國 立 交 通 大 學
電信工程學系
博 士 論 文

以等效電路法設計之縮小化及去耦合化印刷天線

Miniaturization and Decoupling Design of Printed Antennas by the Equivalent Circuit Approach

研 究 生：王侑信
Yu-Hsin Wang

指導教授：鍾世忠　博士
Dr. Shyh-Jong Chung

中　華　民　國　九十七　年　十二　月

以等效電路法設計之縮小化及去耦合化印刷天線

Miniaturization and Decoupling Design of Printed Antennas by the Equivalent Circuit Approach

研究生：王侑信　　Student: Yu-Hsin Wang

指導教授：鍾世忠　博士　　Advisor: Dr. Shyh-Jong Chung

國立交通大學

電信工程學系

博士論文

A Dissertation
Submitted to Department of Communication Engineering
College of Electrical and Computer Engineering
National Chiao Tung University
in Partial Fulfillment of the Requirements
for the Degree of Doctor of Philosophy
in
Communication Engineering
Hsinchu, Taiwan

2008 年 12 月

摘要

本論文旨在研究縮小化天線與多天線去耦合的設計。基於現代無線通訊產品尺寸日益縮小的趨勢，以及經常整合多種無線系統於其中，縮小化天線以及去耦合設計為兩大重要議題。本研究中所有的設計皆使用等效電路模型來解釋天線輸入阻抗的特性。內容主要在於小型天線的設計上提出了新的設計方式，採用電路合成的方式來合成天線，同時可達到共振頻率與阻抗匹配。而去耦合化的設計則提出兩種方式，包含了在電路端提高隔離度的方式，以及使用扼流器阻擋耦合電流的方式，兩者面積皆小於文獻中同類型設計。基於以縮小化為前提，本論文中所提出的架構皆適用於可攜性的無線通訊產品。

本研究將天線分成兩大類，第一類為利用足夠的長度產生波傳導自然共振的設計，例如：縮小化的四分之一波長倒 F 天線。第二類則是使用電路合成產生共振的設計，此為本論文所提出的重點。針對此兩種天線，本論文皆提出縮小化的設計。首先，本論文提出利用螺旋繞線的方式縮小傳統倒 F 天線，同時達到雙頻的效果，以及利用高介電系數的陶瓷材料縮小四股螺旋天線的方式。兩者分別為四分之一波長與一個波長的共振形式，各達到原始面積的 50%及體積的 2.7%的縮小化效果，並且都有等效電路分析其操作模式。另一方面，以電路合成的設計方式，提出了利用串連等長左右手傳輸線的概念來設計開路共振腔，並更進一步的利用短槽孔作為輻射單元，並採用兩顆總集電容，設計出小型天線且實現頻率可調整的功能，僅需要 9 mm x 1.5 mm 的槽孔尺寸即可操作在 1.35 GHz 至 2.45 GHz。此兩種設計都是從等效電路出發，再利用印刷元件來完成佈局實現天線功能，所提出的等效電路可解釋共振頻率以及阻抗匹配的機制。關於去耦合的設計，針對小尺寸的需求開發了縮小化的去耦合架構，使用地緣扼流器。地緣扼流器是使用印刷電路單元實現，其可等效為一個並聯諧振器，能阻擋流經地面邊緣的電流，利用此一特性可以幫助增加兩隻天線的隔離度。此一設計具有小型化以及高適應性的優點，且理論與實作皆已完備並可相互驗證。

Abstract

This dissertation presents the miniaturized antennas and decoupling structures, which are two important issues in mobile wireless applications. All the proposed designs are developed by the equivalent circuit approach in order to understand the impedance features more clearly. The new design concept for antenna has been presented, which is to construct antennas through circuit synthesis. Methods of decoupling are also revealed, including blocking and canceling mechanism. All the proposed structures are compact and low cost that meets the requirement of portable devices nowadays.

The presented miniaturized antennas are divided into two catalogs, the wave resonance type and circuit synthesis type. In natural resonance type, the printed dual-band inverted-F is miniaturized by spiraling the tail of the open-end strip that can simultaneously achieve dual-band operation and size reduction (50%). The dielectric loaded quaduature helix antenna using ceramic rod (relative permittivity = 40) dramatically reduces the volume to be 2.7% of air-loaded one. Both are analyzed by equivalent circuits. The designs of circuit approach utilize the short slot radiator as an inductive element to synthesize the equivalent circuit for antennas. A cascaded right/left-handed transmission line, with opposite phase delay, as a feed is used to create the resonance at operation frequency. An improved design of using two capacitors on a short slot radiator further shrinks the antenna size (9 mm by 1.5 mm for 2.4GHz) and gains more design flexibility. By using varactors it can become a frequency tunable antenna (9 mm by 1.5 mm for 1.35-2.45GHz, measured).

Decoupling technology shows importance in integrated multiple systems and Multiple-Input-Multiple-Output (MIMO) system. For the small device, the decoupling design should also be compact. There is a decoupling method proposed. The current choke composed of printed elements with the function of blocking the induced current on the ground edge. The design is compact and easily integrated in most devices.

誌謝

首先感謝指導教授多年來的栽培提攜和口試委員的建議與評論。還要感謝實驗室眾多的學長姐和學弟妹，因為有你們，論文才能如此順利地完成。

謝謝大家（鞠躬）。

Content

List of Tables

List of Figures

Chapter 1 Introduction

1.1 Background and Motivation

In the past decade, wireless communication has grown rapidly. Many systems have been widely used, e.g. Global Position System (GPS), Wi-Fi for Wireless Local Area Network (WLAN), WiMAX, Bluetooth, and Global System for Mobile Communication (GSM) and Digital Cellular System (DCS). As these systems gain popularity, the demand for wireless products has highly increased, particularly for mobile devices. With the rapid development of the integrated circuit technology, the wireless mobile devices tend to be compact and integrated with multiple systems. For example, a USB WLAN card today is only typically 12 mm × 50 mm that is smaller PCMCIA (50 mm by 100 mm) ($\lambda_0/4$ of 2.4GHz is 32.5 mm). Also, more than one wireless system is evident inside a smart phone today, e.g. GSM, Bluetooth, GPS, WiFi. Moreover, for increasing the data through put, the multiple-input multiple-output (MIMO) antenna system was developed. The system employs multiple antennas which simultaneously transmit and receive within the same system. These examples have to integrate multiple antennas in one device. As a result of the increased demand for miniaturized wireless devices, compact antenna designs with high integrating ability are desired. Since the small devices have limited space reserved for antennas, size reduction becomes the primary concern [1]. Antennas have to be arranged closely giving serious coupling issue in application. However, the coupling will be a serious problem in applications. Therefore, antenna design in modern wireless products has to face important issues on miniaturization and decoupling [2]-[4].

This dissertation focuses on the development of miniaturized antennas and the isolation enhancement between closely-spaced antennas. There are already many design methods for miniaturized antennas – most of which utilize the structure natural resonance of the structure (which corresponds to the length of the antenna). Most miniaturization designs can be simply categorized into three groups – bending the resonant path into a smaller size, using dielectric load, and increasing inductance or

capacitance in single a LC resonator.

Metamaterial have recently bacomes popular in antenna design. There have been many published designs on this subject but the input matching or radiation mechanisms are usually not discussed. A survey of these designs will be discussed in the next section. This dissertation tries to develop a new design method of compact antennas and to provide the equivalent circuit analysis for demonstration. The design methodology stems from equivalent circuit analysis to synthesize the resonance and process input matching. This design concept aims to diminish the consideration of wavelengths. As such, the compact antenna size is possibly smaller if resonance is achieved by discrete reactive elements in stead of the physical length. This dissertation will also study the conventional designs of bending the resonant path and dielectric loading.

The coupling between antennas will degrade the communication system performance, in terms of efficiency due to the cause of power dissipated because of coupling. The solution to this problem is to prevent the other antennas from absorbing the power. In this case, the antenna will be a reactive element with current on it but without power dissipation. This can be achieved by increasing the isolation between antenna terminals, i.e. increasing port isolation. Another solution is to decouple antennas for no current distribution on inactive antennas. Both conditions have already been discussed widely. A survey for above methodology will be presented in the next section. However, many of today's published designs are bulky and most of them are not flexible enough for practical applications.

Today's antennas tend to be compact and so does the decoupling structure for smaller devices. Therefore, this dissertation proposes two compact designs for decoupling and port isolation enhancement. The port isolation enhancement design can process two very closely-spaced antennas. The miniaturization methods of decoupling that respond to the miniaturized antennas also use the circuit approach design for size reduction.

1.2 Literature Survey

In this section, the conventional miniaturization designs and decoupling methods will be presented briefly. The miniaturization methods introduced here are divided into three parts: 1. resonant path alignment, inductive loading or capacitive loading, 2. dielectric loading, and 3. using metamaterial. In the first section, some compact printed dual-band design will also be mentioned due to their popularity.

1.2.1 Miniaturized Antennas

Most compact antennas are resonant antennas. In resonant type wire antennas, length is a main factor in determining the antennas' frequency of operation. For a conventional monopole, it requires a quarter wavelength to resonate and for a loop antenna, it requires one wavelength. To have a compact design, one can simply arrange the resonant path inside a small area or reduce the physical length by inductive or capacitive loading while keeping same electrical length. The conventional design of the resonant path alignment is to bend, fold or turn the path into a smaller size – even a spiral or helical shape is acceptable. Figure 1.1 shows a loop antenna that is folded to be compact for handset application [1].

For mass production, cost is always the first priority. The following examples are given with low cost printed antennas. The printed slot antenna consisting of a slot line, can be miniaturized using similar methods. For example, the most used method is to spiral the slot while keeping its resonant length as shown in Figure 1.2 [5]-[7]. In Figure 1.2(b), a compact open-ended meander slot antenna is shown [8]. In Figure 1.1(c) a slot ring has been miniaturized by fractal geometry [9]. The length of these spiraled or meandered slots have been effectively reduced by increasing antenna width. By bending the slot, the above methods have maintained the total electrical length which determine the resonant frequency.

According to transmission line theory, the inductive loading or capacitive loading can increase the equivalent electrical length which is useful in miniaturizing the antenna. The microstrip-fed slot antenna can be miniaturized by inductive or

capacitive loading, as realized by printed elements, shown in Figure 1.3(a) [10]. Chip capacitors can be loaded at the ends of the coplanar-waveguide-fed slot line for further size reduction, as shown in Figure 1.3(b) [8]. Figure 1.3(c) is the disk-loaded monopole. The antenna is considered as a series LC resonator when the disk acts as a capacitive load [11]. The simple LC model can show resonance characteristics of an antenna but does not include an impedance matching mechanism.

Aside from, a single-band compact antenna, there are many other compact dual-band antenna designs. Since 1999, the WLAN standards including the IEEE 802.11a/b/g systems were established by the IEEE 802.11 Group. In the U.S., the 802.11b/g WLAN standards are used in the frequency range of 2.4 to 2.4835 GHz while the 802.11a standards are used from 5.15 to 5.35 GHz and 5.725 to 5.825 GHz. To enhance the communication capacity of a unit cell, a combo system with 802.11a/g or 802.11a/b/g standards have became popular. In this combo system, the antennas are like transceivers operating in both 2.45 and 5.25 GHz frequency bands; thus, a dual-band antenna with a single input port is needed for size reduction. Many dual-band antennas have been proposed in the literatures. Some of these designs use two similar resonators to achieve dual-band operations, such as a double inverted-F antenna [13] and an F shape monopole (double-L monopole), as shown in Figure 1.4(a) [14]-[17]. These are miniaturized by bending the strips into an L-shape. Also, some of these designs use a single block antenna with multiple resonant modes to achieve dual-band operations, such as a tapered bent folded monopole [18], as shown in Figure 1.4(b), meandered CPW-fed monopole [19], and, an L-shaped monopole [20].

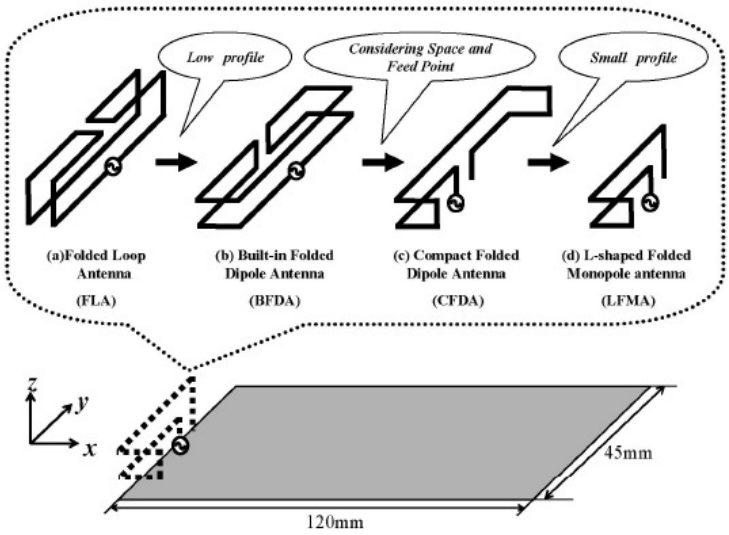

Figure 1.1 Line alignments of a loop antenna for handset use.

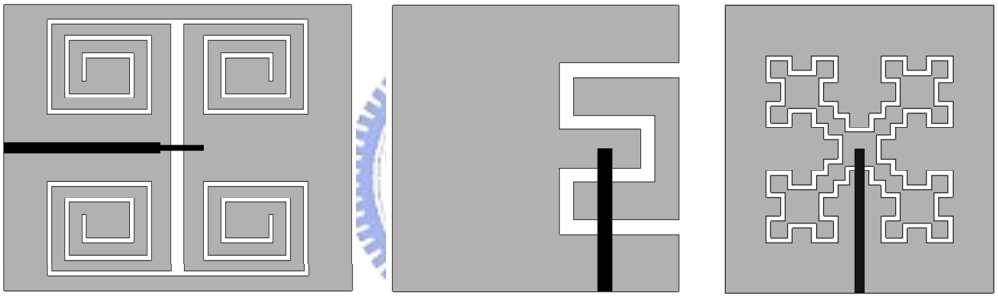

Figure 1.2 (a)The spiraled microstrip-fed slot antenna. (b)The microstrip-fed meandered slot antenna. (c)The fractal microstrip-fed slot ring antenna.

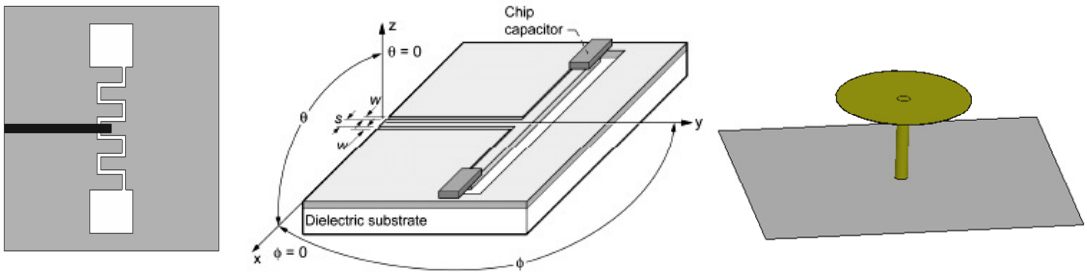

(a) (b) (c)

Figure 1.3 (a)The microstrip-fed slot antenna with inductive load in central portion. (b)The CPW-fed slot antenna with capacitive load at the open end. (c) The disk-load monopole antenna.

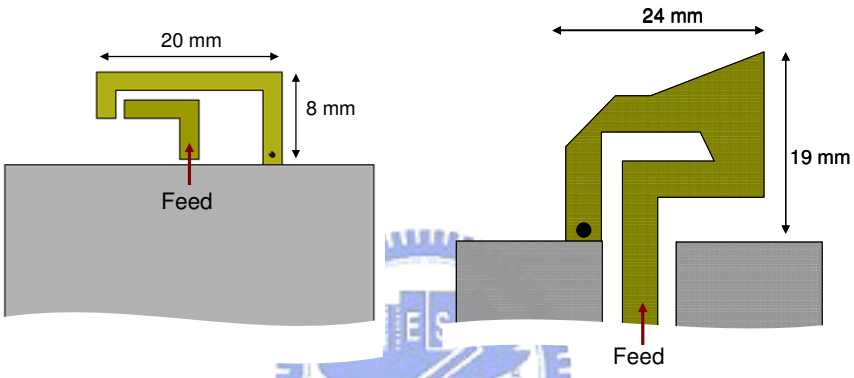

(a) (b)

Figure 1.4 (a)The compact coupled inverted-L dual-band antenna. (b)The compact CPW-fed dual-band antenna.

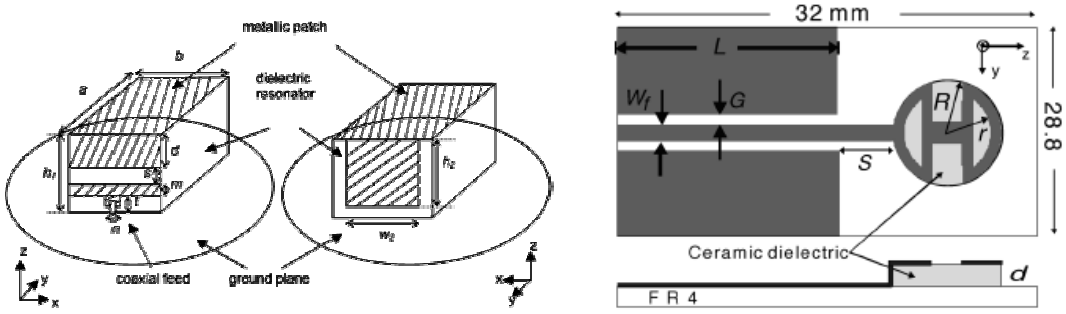

(a) (b)

Figure 1.5 (a)The monopole antenna printed on a dielectric slab. (b)The dielectric loaded monopole antenna.

To have enough electrical length under physical constraints, employing the use of a dielectric is an efficient solution. With a material of higher relative permittivity, one can have a larger phase constant, thereby reducing the physical resonant length [21]. Figure 1.5 shows a monopole printed on a ceramic piece [22]-[23]. In Figure 1.5(b) the antenna length is half than that in air by using the relative permittivity of 22 [23].

Unlike natural transmission line with a positive phase constant, metamaterial based transmission lines have a designable phase constant. This kind of artificial structure has been utilized by numerous guided and unguided wave applications. One notable example is Left-handed materials (LHMs) which possess negative refractive index and have drawn tremendous interests in both scientific and engineering fields. The Left-handed transmission line (LH TL) is characterized by the phase advance whereas the Right-handed transmission line (RH TL) is characterized by phase delay along the power traveling direction. Metamaterial antennas possess different characteristics from conventional antenna designs that are based on the standard transmission line. RH TL and LH TL can be embedded into each other and named as Composite Right/Left- Handed Transmission Line (CRLH TL). [24] provides an practical application inserting LH TL into the host RH TL. Its equivalent circuit and phase constant are shown in Figure 1.6. The Zeroth-order Resonance (ZOR) makes use of the opposite phase properties of RH and LH TL and has been proved experimentally [25]. Small planar antennas utilizing the ZOR structure were published [26-27], as shown in Figure 1.7. Basically, they are just a section of synthesized CRLH TL. The physical size of such antenna can be arbitrary since its size is specified by the value of the capacitances and inductances instead of wavelength. The concept of the infinite wavelength resonant antenna was first demonstrated in [26].

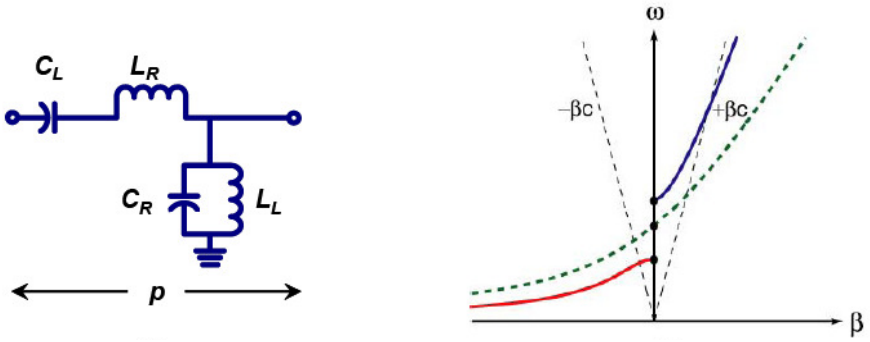

(a) (b)

Figure 1.6 (a)The equivalent lumped circuit of CRLH TL. (b)The phase constant curve of CRLH TL which possesses both positive and negative values.

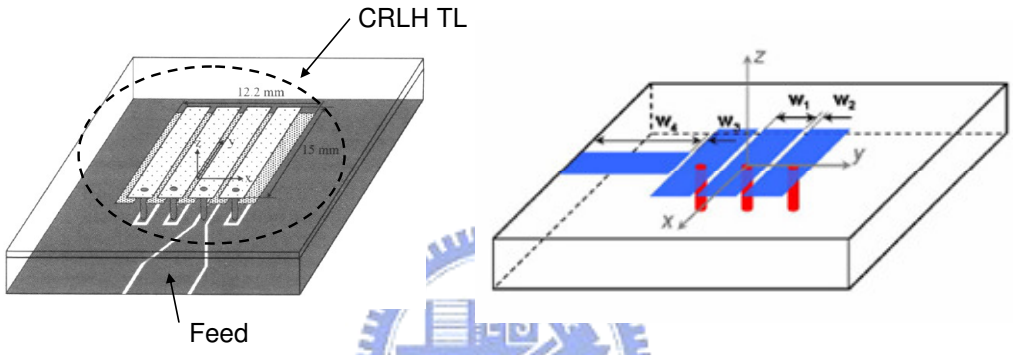

(a) (b)

Figure 1.7 (a)The taped CPW-fed ZOR antenna. (b)The coupled microstrip-fed ZOR antenna.

1.2.2 Decoupling Methods

The use of multi-element antennas, such as MIMO antenna systems, is one of the effective ways to improve reliability and increase channel capacity. Due to the sharing of ground currents between antennas, these antennas couple strongly to each other; thereby, making it difficult to integrate multiple antennas closely in a small and compact mobile handset. For an MxN MIMO communication system, the data throughput can be pushed up to K times (K = min(M, N)), that of a Single-Input Single-Output (SISO) system, as long as the communication channels linked between the transmitter and the receiver are uncorrelated [2][3][29]. The correlation between the channels depends not only on the propagation environment, e.g., multi-path effect due to the reflection and diffraction of outdoor buildings or indoor partitions, but also on the coupling between the M or N antennas. High antenna coupling (or low isolation) would introduce signal leakage from one antenna to another, thus increasing the signal correlation between the channels. It will also decrease the antenna radiation efficiency due power dissipated in the coupled antenna port. The signal correlation between two receiver antennas can be reduced by increasing the antenna spacing. However, spacing is usually limited, especially for a mobile terminal which has very strict volume reserved for antennas. Another way to diminish correlation is by using multiple antennas with different radiation patterns. The patterns have to be complementary to each other in space in order to receive multi-path signals from various directions. However, the complementary patterns may not be the best solution for MIMO system. This is because for a single device, aside from the MIMO system, there are other systems operating simultaneously in the same frequency band, e.g. IEEE 802.11b and Bluetooth – both of which are popular systems that operate in the same 2.45GHz band. In this case, the coupling problem causes the same problem as MIMO system of the radiation efficiency. Thus, it causes inefficiency in the systems due to coupling.

Currently, there are numerous papers published focus on diminishing antenna coupling. Itoh and his co-workers used the defected ground structure (DGS) to increase the port isolation of dual-polarized and dual-frequency patch antennas [30] operating at different frequencies. To decouple two nearby antennas operating at the

same frequency electromagnetic band gap (EBG) structures can be used. Inserting band gap structures between antennas can help block wave coupling. Mushroom-like EBG structures are usually inserted between patch antennas to prevent the propagation of surface waves for higher isolation and better radiation patterns, as shown in Figure 1.8 [31]-[32]. These EBG structures provide conspicuous decoupling effect, but suffer from complicated structures and large structure area. Possible loss may also be induced in the resonant EBG structures. To reduce the coupling between two planar inverted F antennas (PIFAs), Diallo [33]-[36] used a suspended metal strip linking the two antennas to cancel the reactive coupling between antennas, as shown in Figure 1.9. This neutralization technique has been also extended to patch antennas by Ranvier [37]. In [38], a decoupling circuit network was realized for two-element array by using external transmission lines. Although good isolation was achieved, only weak coupled antennas were tackled. The all-transmission-lines configuration also made the circuit bulky. The mutual coupling of two closely-packed antennas was reduced by etching slots on the ground plane [39]. The fish-bone like slots formed equivalent inductors and capacitors on the ground plane, which prevented the flowing of the coupling ground current between the antennas, as shown in Figure 1.10. A large ground plane size, which was close to the antenna size, was needed for sufficient isolation. The above methods can be divided into two cases. The first is to insert band gap structures prevent the direct propagation of electromagnetic wave between two antennas, like EBG and DGS. The driven antenna will not induce current on the other antenna. The second is to cancel the coupling current by using additional reactance network between antenna ports, such as a suspended strip, as a decoupling network. This is similar to the crosstalk elimination circuit used in telephone network. In this case, the driven antenna does induce the current on the other antenna but the decoupling network cancel the current at the antenna terminal.

In conclusion, most of the decoupling technology are bulky, especially EBG structure. The suspended reactive element between antennas is simple but not convenient for the application due to the additional empty space requirement and wire supporting mechanism. These designs are not flexible and compact enough for different PCB configurations. Therefore, this dissertation would like to propose a

more compact and flexible method for decoupling. The primary consideration for their design is to attain a compact size followed by system flexibility.

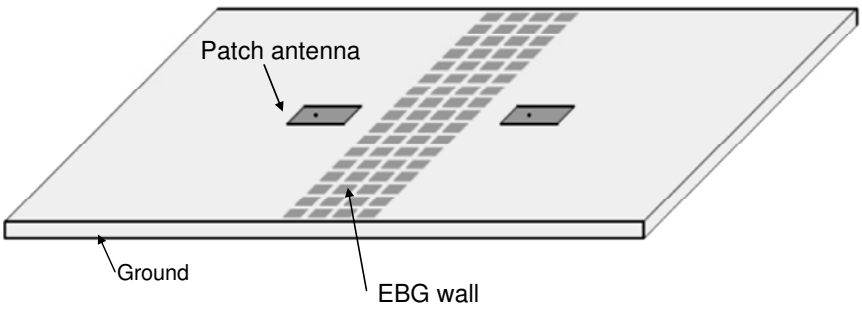

Figure 1.8 The EBG structure used to decouple two patch antennas.

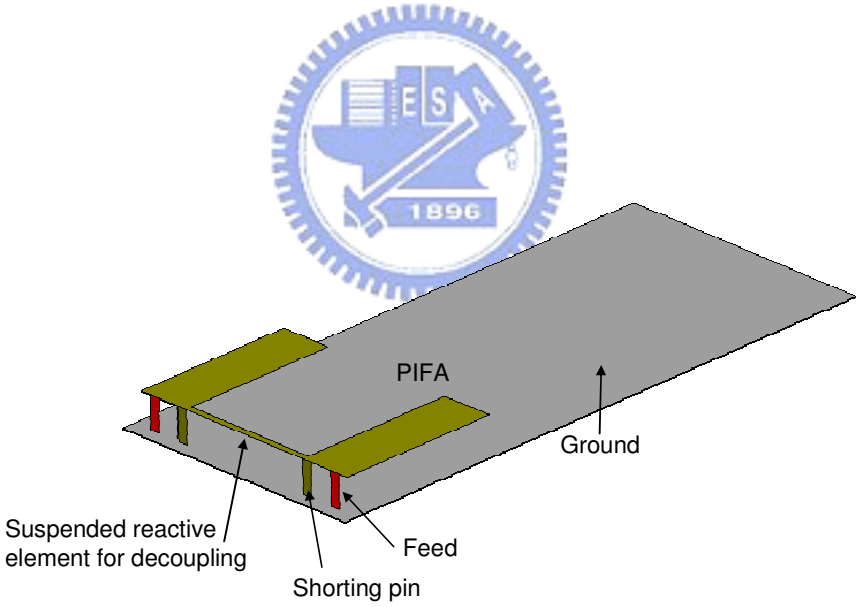

Figure 1.9 The suspended reactive element, a thin line, used to decouple two PIFAs.

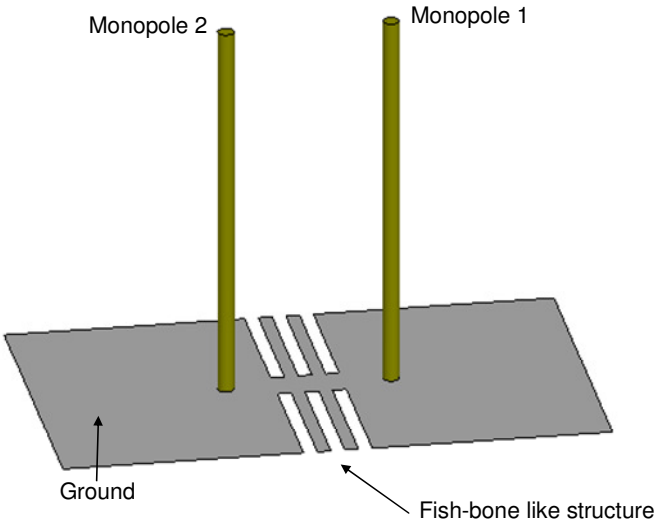

Figure 1.10 A fish-bone-like structure inserter on the ground plane to decouple two monopole antennas.

1.2.3 Antenna Equivalent Circuit Analysis

The equivalent circuit analysis is a kind of antenna modeling, which uses a lumped element circuit to model the input impedance of an antenna. Therefore, the equivalent circuit approach used in this study uses a lumped element circuit for antenna analysis and design.

The equivalent circuit analysis of antennas has already been used for decades. This method is usually used to explain antenna impedance and resonance mechanisms [40]-[43]. Additionally, the equivalent circuits of antennas are used in spice modeling for the analysis of antenna gain bandwidth or time-domain waveforms transmitted from antennas, etc [44]-[45].

Circuit models are used to represent antenna impedance curves. Thus, their creation usually considers antenna physics which mostly relate to resonance mechanisms. For example, a loop antenna with an anti-resonance at the operating frequency will be basically modeled by a parallel LC resonator. A parallel resonator is a basic circuit model of antennas with anti-resonance. However, a purely parallel resonator cannot depict antenna impedance curves precisely. Additional circuit parameters, such as parasitic capacitors, are required for better modeling.

Another topic relevant to equivalent circuit modeling is effective modeling bandwidth. Since lumped elements have bandwidth limitations for modeling distributed elements, the circuit model with lumped elements is also limited; thus, to describe antenna impedance over a wider bandwidth by circuit elements, distributed elements, such as a transmission line will be used.

[40], shows an antenna equivalent circuit of a strip line coupled patch antenna that considers many circuit parameters. Figure 1.11 shows the presented antenna equivalent circuit in [40]. Considering the anti-resonance of the patch antenna, R_A, L_A, and C_p basically form the parallel resonator of a patch. To increase modeling accuracy, L_P and R_P are treated as parasitic elements connected in series with C_p. Coupling through the slot of an open-ended strip line are represented by an impedance transformer – C_t and L_t. The circuit elements mentioned above form a complex antenna equivalent circuit model. The value of each circuit element can be obtained by curve fitting. Therefore, knowing the antenna input impedance is necessary for model extraction regardless of where this value is obtained – whether from measurement or from full-wave simulation. Another example on the operation mechanism of an antenna is that of a ladder CPW-fed slot antenna using multiple resonators. [41] shows a circuit model to explain and describe resonances of such an antenna. This type of circuit modeling does not have a direct relation with antenna physics. In [42], a broadband modeling of a dipole is presented. Two parallel

resonators are used to precisely fit the antenna impedance curve over a wider bandwidth since the two resonators can provide two additional poles, thereby, increasing flexibility in curve fitting.

The equivalent circuit is not only used to explain the operation mechanism and describe the impedance curve but is also for spice simulation in the time domain. In [44], a circuit model of an ultra-wide-band antenna is established and is used to calculate the waveform of receiving signal. Chapter 2 of this dissertation will show the equivalent circuit analysis for the proposed antenna structures.

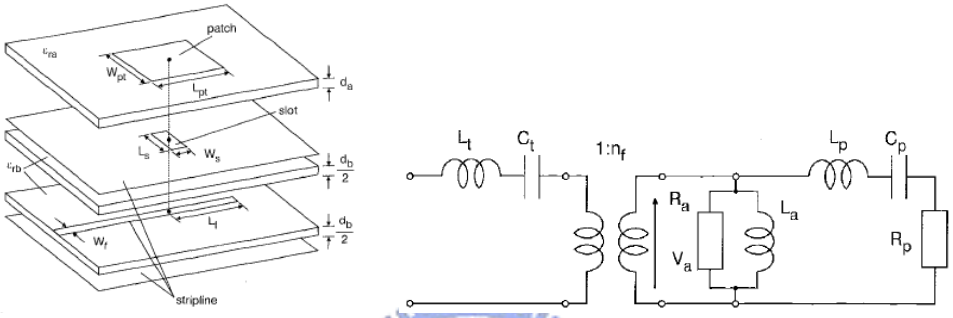

(a) (b)

Figure 1.11 (a)A stripline coupled patch antenna (b)The equivalent circuit model of a stripline coupled patch antenna.

1.3 Antenna synthesis by the Equivalent Circuit Approach

In most publications, the antenna equivalent circuit is used for analysis and explanation. Design of the antenna is usually done first and then the establishment of equivalent circuit. However, the use of the antenna equivalent circuit can be expanded to antenna design. This means that the equivalent circuit must be designed first then synthesized into the antenna design. Chapter 3 will shows the synthesis of an antenna from an equivalent circuit.

This study uses the equivalent circuit approach to achieve miniaturized design. An equivalent circuit established prior to achieve resonance at the antenna's operation frequency. The antenna is directly synthesized from the equivalent circuit instead of the iterative full wave simulation analysis. The equivalent circuit is designed to create resonance at a specified frequency. This is used as a reference in antenna synthesis. Next, the antenna topology is mapped from the equivalent circuit by using printed circuit elements to represent components of the circuit model. In this design procedure, resonant frequency can be easily controlled by an equivalent circuit. However, the radiation effect of antenna is difficult to control in the equivalent circuit model. To solve this problem, there are two possible methods. The first method uses equivalent circuits to control the resonance type and resonant frequencies of antennas. The bandwidth and radiation performance need to be fine tuned when processing the antenna layout. This means the radiation mechanism is considered during layout. This design method will be shown in Chapter 3-1.

The second method establishes circuit model of radiators by considering the radiation mechanism, and radiation resistor, during modeling. This means certain basic radiators, such as slots, should be modeled first. Thus, some preparatory work has to be done before the design of antenna equivalent circuit, such as establishing the radiator model library. The radiator model can be obtained through full-wave simulation or by measurements. However, only simple radiators can be modeled very well. Additionally, interaction between multiple radiators of the same antenna is also very difficult to be modeled. This method will be shown in Chapter 3-2.

The method of antenna synthesis from equivalent circuit model increases the flexibility of antenna design and reduces simulation efforts. Basic antenna design needs several iterations of full-wave simulation in order to obtain the specified resonant frequency followed by antenna layout tuning for input matching and bandwidth. The equivalent circuit approach helps obtain the correct resonant frequency quickly. For radiator models, although it takes time for modeling, the obtained radiator model can be reused in many future antenna designs.

1.4 Contributions

A series of miniaturized antenna design is presented with the equivalent circuit analysis. Also, the decoupling methods for two closely-space miniaturized antennas are developed. Both of miniaturized antenna design and decoupling method are important in modern wireless applications because modern devices tend to be smaller with less reserved antenna space. Antenna designs or decoupling structures should therefore be more compact as compared to whole device.

The research of miniaturized antennas is divided into two categorizes. One category is to use natural resonance in design – resonant antenna by using wavelengths. The other is design by circuit approach – creating resonance irrespective of wavelength. In the first category, a printed spiraled inverted-F antenna operating in 2.4/5.2GHz is very compact (9.5 mm by 6.5 mm). This can easily fit in most compact devices today. The dual-band mechanism of the spiraled inverted-F antenna is also explained by the equivalent circuit model. The dielectric-loaded quadrature helix antenna (QHA) with relative permittivity of 40 is another compact antenna design which is only 2.7% of air-loaded antenna. The challenge and solution of using dielectric to miniaturize QHA is studied and demonstrated in this dissertation. Two designs using circuit approach are proposed. The first design uses a short slot radiator with cascaded left/right-handed transmission line feed. The use of two cascaded sections of transmission line with identical electrical length and opposite phase constant to create anti-resonance is new concept. The second design uses a short slot radiator as an inductive element and two capacitors for tuning resonant frequency and matching. Both designs are with equivalent circuit demonstrations to help understand the antenna impedance and operating principle of the antenna. The advantages of circuit approach design are the flexibility and compactness of the resulting design which can be merged to the design of the wireless communication system. The radiation mechanism and input impedance are also discussed in the above design. The miniaturization methods mentioned provide new design concepts, several techniques and complete impedance analysis for compact antenna design.

The decoupling design reveals two compact structures. One is the circuit approach design which can reduce coupling by the circuit and can handle any two

closely-spaced antennas. The complete analysis of the circuit structure is demonstrated in Appendix A. Additionally, the same structure can be extended to dual-band application under limited conditions. The other is the miniaturized current choke that can block ground edge current. The ground edge current effect is common in monopole antenna design. The proposed choke was developed against edge current. Two useful applications are presented – decoupling and pattern regulation. The current distribution analysis is also illustrated to help understand the behavior of the edge current and the current choke. Both miniaturized decoupling structure are compact and flexible for application. This dissertation focuses on the miniaturization design of antenna and decoupling structures.

Chapter 2 Miniaturized Antennas with Wave Resonances

2.1 Spiraled Printed Inverted-F Antenna

The conventional printed inverted-F antenna is widely used because of several advantages such as making up with ease, matching the input impedance with no outer circuit, having omni-directional pattern, etc. However, its length is limited to be a quarter wavelength of the operating frequency, which usually occupies quite a few amounts of space in PCB [46]-[49]. Besides, the single inverted-F antenna can only be operated at the certain resonant frequency, which is unable to supply the market need of dual-band or triple-band applications. To solve these problems, in this section, PIFA related structures by means of spiraling an inverted-F antenna which achieves dual-band operation by one resonator. The antenna is designed on the FR4 substrate with 0.8mm thickness for commercial usage.

2.1.1 Antenna Configuration

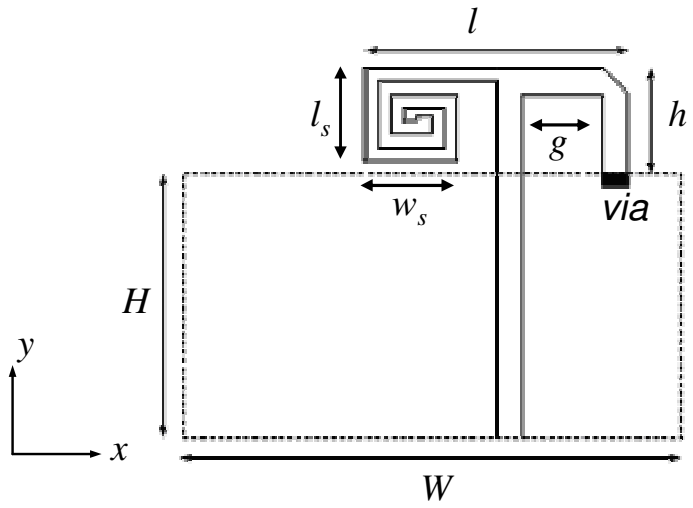

Figure 2.1 The configuration of dual-band spiraled printed inverted-F antenna.

The first PIFA-related miniaturized dual-band antenna is the spiraled PIFA (Figure 2.1). The spiral inductor loaded on the antenna can both realize dual-band

operation and miniaturizes the size of the conventional inverted-F antenna. The chosen ground width is 46 mm compatible for PCMCIA interface. The antenna placed near the edge of ground plane is possible for antenna diversity.

2.1.2 Equivalent Circuit Analysis

In this section, the effect of the spiral is discussed and the circuit model is also developed for analyzing. And in Figure 2.2(a), there is a typical inverted-F antenna implemented on a printed circuit board. For this inverted-F antenna, the microstrip feed line is connected to a horizontal metal line with one end short-circuited to the ground and the other end open-circuited. The metal line and the ground plane form a quasi transmission line. It is easy to derive that as the total length of this quasi transmission line equals a quarter of wavelength, the input reactance vanishes due to the resonance of the inductor-like short-circuited line and the capacitor-like open-circuited line. The corresponding return loss simulated by the commercial EM simulator IE3D [50] is presented as the curve *a* in Figure 2.3(a). Here, the length of the horizontal metal line is designed as a quarter wavelength of the fundamental frequency 2.45 GHz, so that a deep resonance occurs at that frequency with return loss larger than 20 dB. It is noticed that another resonance presents at the frequency around 7.35 GHz, which is the triple of the fundamental frequency.

In order to demonstrate how the spiral works, a number of spiraled inverted-F antennas were also simulated. A set of spiraled inverted-F antennas (as Figure 2.2(a)-(d).) with the total length of the metal line kept similar and spiraled gradually were designed. The total length of the strip from short point to open end in Figure 2.2(a) is 25.5 mm. The fundamental resonant frequency of these antennas should remain about the same, which can be verified from the simulated return losses shown in the curves *a-d* of Figure 2.3(a). As a matter of fact, the return losses of the four antennas are all better than 15 dB, except for the variation of the bandwidth. However, it is also found that the frequency of the second resonance becomes lower as the antenna tail is spiraled more. The second resonant frequency shrinks to about 71% (from 7.35 to 5.25 GHz) when the antenna structure is changed from the conventional PIFA of Figure 2.2(a) to the spiraled one of Figure 2.2(d).

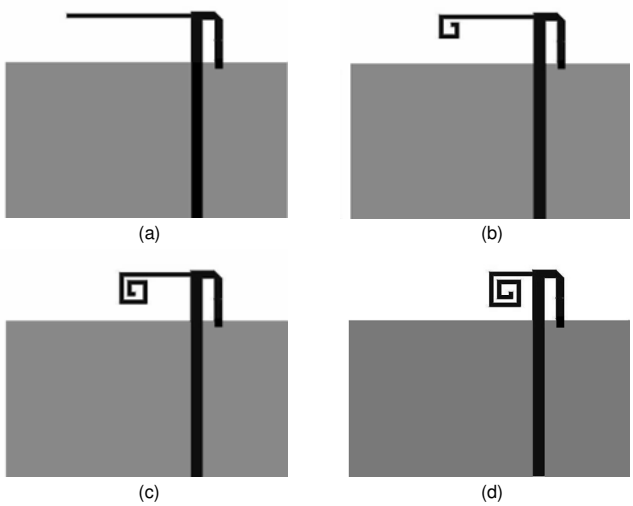

Figure 2.2 Four printed inverted-F antennas with different spiraled tails. The tail lengths are kept the same for the four antennas.

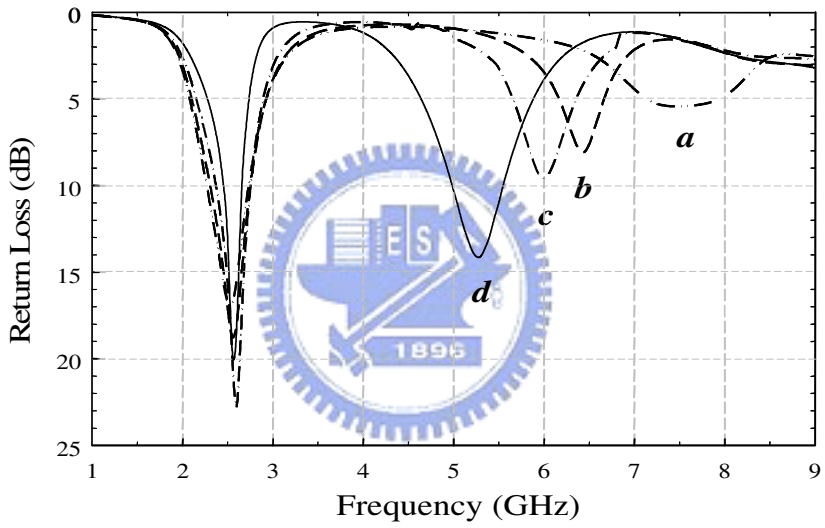

(a)

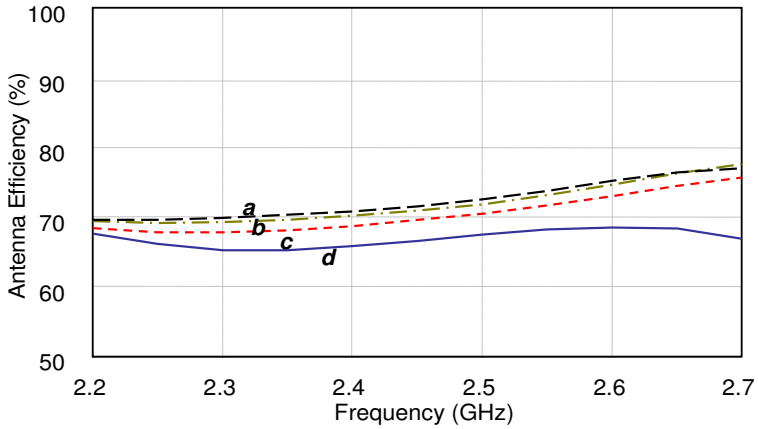

(b)

Figure 2.3 (a)Simulated return losses, as functions of frequency, for the antennas shown in Figure 2.2. (b)Simulated radiation efficiency, as functions of frequency, for the antennas shown in Figure 2.2.

The miniature antenna always encounters the problem of the efficiency, especially for the lower operation band. The simulation of antenna efficiency around 2.45GHz is shown in Figure 2.3(b). It can be found that the efficiency is almost the same (about 70%) for the four antennas shown in Figure 2.2. The degradation of efficiency is under 5% in the required bandwidth. It means that the additional loss induced in this miniaturized antenna design is negligible. The invariance of the efficiency may be due to that a large ground plane with length larger than a quarter wavelength is used. (Note that the ground plane is a part of the antenna, on which the induced current contributes to the radiation performance of the antenna.) However, the bandwidth of the 2.45GHz band shown in Figure 2.3(a) becomes narrower with the smaller antenna size. This can be attributed to the increasing of antenna quality factor due to the antenna size. The efficiency of the well matched spiraled inverted-F antenna around 5.2GHz is about 50%, which is lower than that (70%) of a typical PIFA designed at the same frequency. In the 5GHz band, the proposed antenna operates at the high order mode with three quarter wavelength resonance. The current flows in the spiral with different directions, thus reducing the radiation efficiency of the antenna.

For conceptually understanding the frequency reduction effect of the second resonance, a brief equivalent circuit model for the spiraled PIFA is proposed as shown in Figure 2.4(a), where the PIFA is modeled as a short-circuited transmission line of length θ_2 in shunt with a transmission line of length θ_1 loaded by an effective radiation resistance R_a. An inductor L is inserted in the end of the open-circuited transmission line in order to take account of the spiraling effect of the antenna tail and the parasitic inductance of the transmission line. In addition, a parasitic capacitor C_s shunt to ground for fringe field is considered in the open-end transmission line. The input admittance

$$Y_{in} = Y_1 + Y_2 = Y_0 \frac{Y_L + jY_0 \tan\theta_1}{Y_0 + jY_L \tan\theta_1} - jY_0 \cot\theta_2 \qquad (2\text{-}1)$$

where Y_0 (= Z_0^{-1}) and β denote the characteristic admittance and phase constant, respectively, of the transmission line. The admittance Y_L can be written as:

$$Y_L = Z_L^{-1} = \left[jwL + R_a + \frac{1}{jwC_s} \right] \qquad (2\text{-}2)$$

The input reflection coefficient Γ, or the return loss, can thus be calculated from

$$\Gamma = \frac{Y_0 - Y_{in}}{Y_0 + Y_{in}}. \tag{2-3}$$

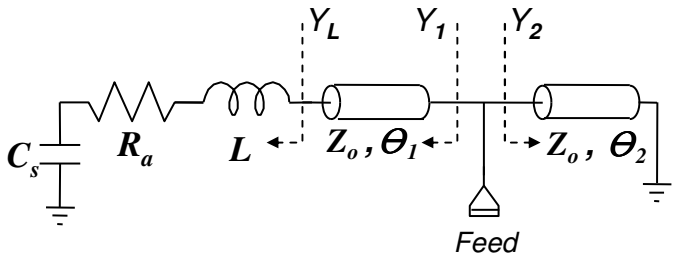

(a)

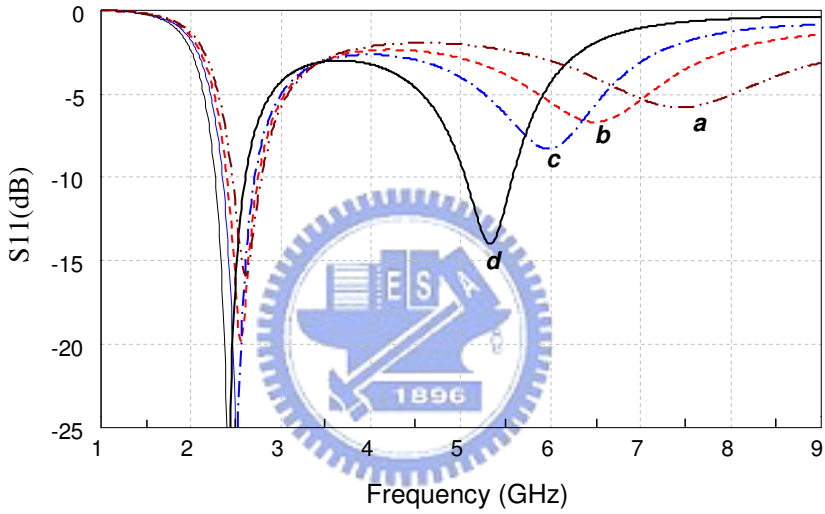

(b)

Figure 2.4 (a)Equivalent transmission line model for the spiraled printed inverted-F antenna. (b)Simulated return losses of the equivalent model with Z_o = 180 Ω, θ_1 = 57.4°, θ_2 = 18.3°, C_s = 0.13 pF, R_a = 150 Ω and L = 3.7, 6, 8, 12nH.

Figure 2.4(b) illustrates the calculated return losses, functions of frequency, for the equivalent circuit model of the spiraled antenna. The characteristic impedance Z_o is 180 Ω, which is about the EM-simulation value of the characteristic impedance for the antenna's quasi transmission line portion. The electrical length is set as $\theta_1 = 57.4^\circ$ and $\theta_2 = 19^\circ$ at 2.45GHz. The total electrical length is around quarter wavelength at 2.45GHz. Consider the small parasitic capacitor C_s to be 0.19pF as fringe field. The effective radiation resistance R_a is around 150 Ω. The inductor L is related to the spiraled strip, which is the dominant factor of the model. From the intuition, its value should increase as the strip is spiraled more. However, since the inductance

caused from the spiraling is distributed in the structure, it is hard to extract from the EM simulation. In this study, this inductor was chosen as 3.7, 6, 8, and 12 nH for the antennas (a) to (d) in Figure 2.2, respectively, so as to fit the EM-simulation results (Figure 2.3 (a)) of the antennas.

One can observe from Figure 2.4(b) that in the frequency span, two resonances are generated by each circuit. The higher resonant frequency at 7.35 GHz moves towards the lower frequencies of 6.5, 6, and 5.25 GHz, although, at the same time, the lower resonant frequency is remained around 2.45 GHz. Finally the specified dual-band operation is achieved by only one resonator. The results resemble those of the spiral antennas quite well, meaning that the equivalent circuit model including the value-changing inductor does explain the frequency characteristics of the proposed dual-band antennas.

2.1.3 Experimental Results

The spiraled PIFA of Figure 2.2(d) (or Figure 2.1) was fabricated on an FR4 (ε_r = 4.4) substrate with thickness 0.8 mm. The ground size of the substrate is set as $W \times H$ = 46 mm × 55 mm. The antenna occupies an area of $l \times h$ = 9.5 mm × 6.5 mm, which is only 50% of that of the PIFA without spiraling. The others parameters are l_s=4.5 mm, w_s=4 mm, g=1.54 mm and both the width and gap of spiral=0.5 mm. Figure 2.5 shows the measured return loss corresponding to the EM simulated one. Both results agree each other quite well. The measured 10-dB bandwidth is 140 MHz centered at 2.45 GHz and 756 MHz at 5.25 GHz.

The measurement radiation patterns of the antenna are presented in Figure 2.6(a) for 2.45 GHz and Figure 2.6(b) for 5.25 GHz. Comparing with the conventional antenna (not shown here), the radiation patterns at the lower frequency of the proposed spiraled antenna are not varied much. The radiation pattern in the y-z plane is omni-directional with a peak gain of 1.59 dBi and average gain about -3 dBi. The radiation patterns at 5.25 GHz are also omni-directional in the y-z and x-z planes. The peak gain and average gain are respectively near 3 and -1.5 dBi in the y-z plane, and are about 0 and -5 dBi in the x-z plane.

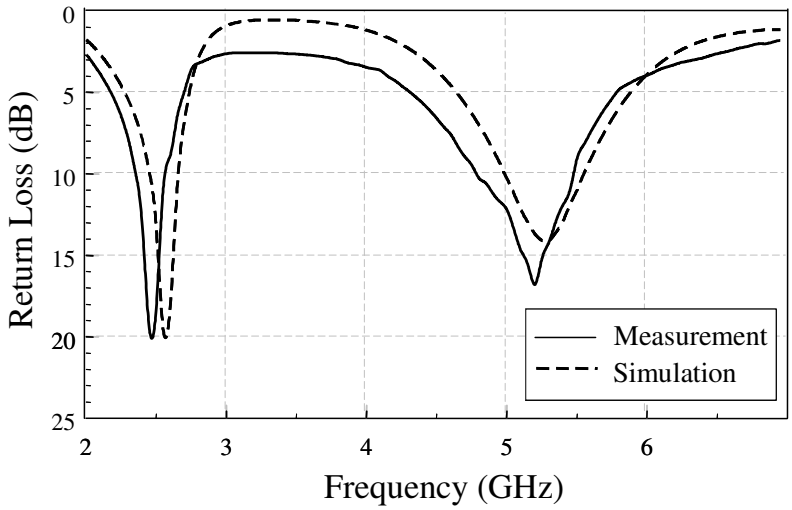

Figure 2.5 Simulated and measured return losses to frequency of the dual-band spiraled printed inverted-F antenna.

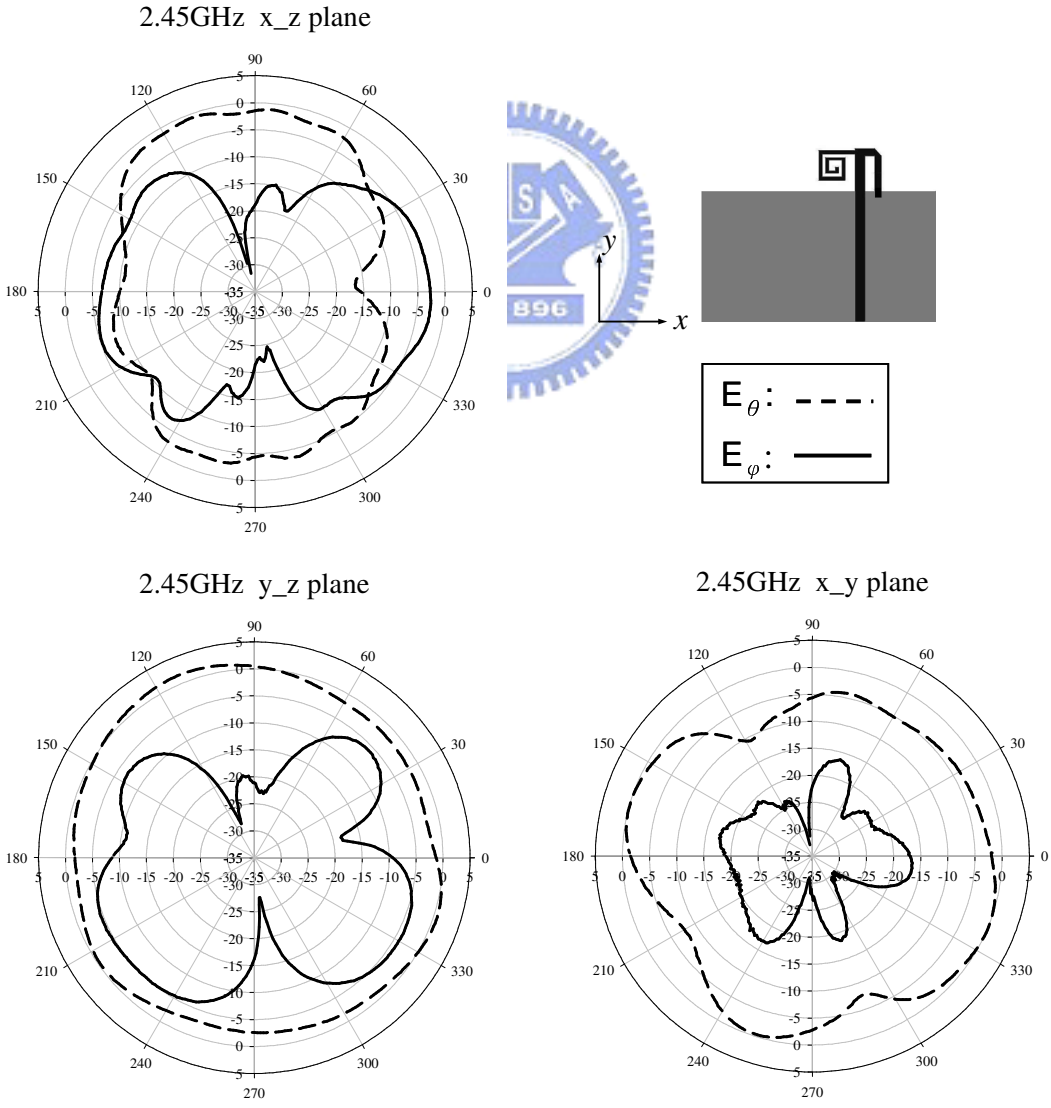

(a)

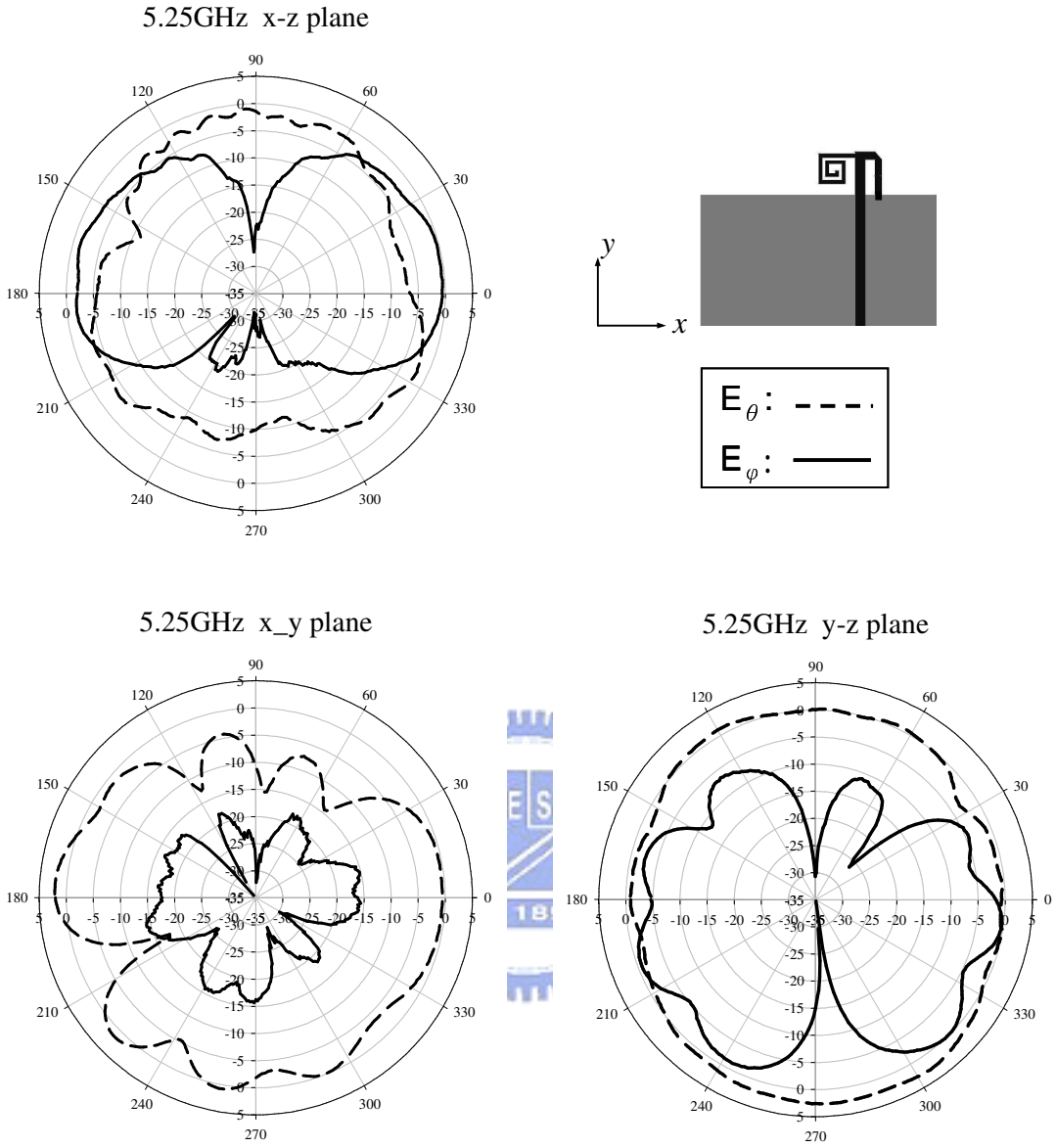

(b)

Figure 2.6 Measured radiation patterns at the principal planes for the dual-band spiraled PIFA at (a)2.45GHz and (b)5.25GHz. (solid line denotes E-theta; dashed line denotes E-phi)

2.1.4 Summary

Through the features of the conventional PIFA, the original antenna is re-shaped to a spiral structure for the purpose of miniaturization and dual-band operation. A dual- band equivalent circuit model for spiraled antenna has been developed as well in order to examine the effects with the tail of the antenna spiraled little by little. The size of the proposed spiraled antenna is about 50% of a conventional one. The proposed type not only holds most of the properties of the conventional antenna but also provide more options for dual-band antenna designs. Finally, since the bandwidths of the higher band is about 700 MHz, it is easy, after upwards shifting the center frequency, to cover all signal frequencies (from 5.15 GHz to 5.825 GHz) of the IEEE 802.11a WLAN application.

2.2 Dielectric-loaded Quaduature Helix Antenna

The resonant quadrifilar helix antenna (QHA) can generate a semi-spherical radiation pattern for circular polarization. This radiation pattern with a wide beamwidth can facilitate low-elevation reception or a wide angular receiving range. This antenna is already applied in many spacecraft systems [51]. The advantages of the semi-spherical radiation pattern of the QHA are also attractive for mobile satellite communication and position-location systems, which typically require circular polarization and a wide beamwidth. The conventional resonant QHA has two resonant bifilar helix antennas (BHAs) oriented in a mutually orthogonal relationship on a common axis. The resonant BHA can be treated as a twisted one-wave-length loop antenna. To achieve circular polarization, these two BHAs are fed in quadrature phase. The radiation pattern shape of the resonant QHA depends on helix dimensions, number of turns and pitch angle. When four arms are roughly half wavelength with half turn with axial length equal to a quarter wavelength, the radiation pattern approaches a semi-sphere like a cardioidal shape [52]. The demand for global positioning systems (GPSs) has recently grown dramatically for portable tracking devices or mobile phones with GPS functions. This need has led to the increased requirement for circular-polarized antennas. The good radiation property of resonant QHAs has drawn considerable attention. However, the half wavelength of 1.575GHz (GPS L_1 frequency) for a resonant QHA is too long to be integrated into handsets without minimizing the QHA.

2.2.1 Antenna Configuration

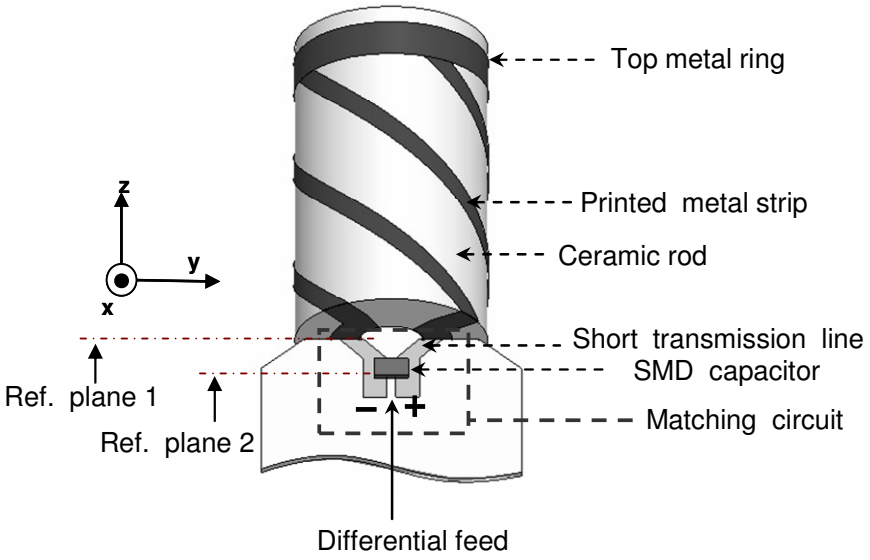

Figure 2.7 Antenna structure including the adapted PCB with a SMD capacitor.

Figure 2.7 presents the geometry of the proposed antenna. The overall structure contains a hollow ceramic rod with printed metal strips on the surface and a planar circuit substrate with a matching structure and feeding lines. The ceramic rod with a relative permittivity of 40 helps reduce antenna size [53]-[54]. Its low material loss with loss tangent lower than 0.0001 at the frequency under 5GHz also helps maintain the antenna efficiency. The hollow structure of the rod is designed for fabrication convenience and to retain structure strength. The circuit substrate, which has a protrusion, can be inserted into the ceramic rod during assembly. The metal strips on the ceramic rod surface are silver ensuring good conduction, and are printed by using the low-cost screen-printing technique. To reduce the procedure of manufacture, only the rod sidewall and bottom are printed. A metal ring on the top of the sidewall is used to connect the four helical arms of the resonant QHA. The feeding lines are a differential line that directly contacts antenna feed points on the ceramic rod bottom. Feeding lines are printed on the circuit substrate. The proposed antenna is designed to operate at 1.575 GHz for GPS applications. The structure is simulated using the full-wave simulation tool, Ansoft HFSS. Due to the high permittivity of the ceramic rod, the antenna is very small, only 4.5 mm in radius and 14.8 mm in height ($<0.08\lambda_0$). The hollow-hole diameter in the ceramic rod is 3 mm. The metal strip width is 1 mm.

The helical arms are roughly half turns with a pitch length of 22 mm. The helical orientation of the antenna affects radiation performance. The helical arms of the antenna are designed in a left-hand orientation to optimize the right-hand circular polarization (RHCP) gain in the upper half space. This helix orientation generates better RHCP gain in the upper space than a left-hand circular polarization (LHCP) gain in the lower space [52]. The antenna is matched to 100 Ω by the matching structure. The 100-Ω differential line is then used to feed the antenna. Both the feeding line and matching structure are printed on an 0.8-mm-thick FR4 substrate.

2.2.2 Equivalent Circuit Analysis and Matching Network

The impedance characteristics of the dielectric-loaded QHA can be observed from simple equivalent circuits. Because the configuration of BHA is constructed as a twisted pair line, the BHA model consists of a differential transmission line and resistor (Figure 2.8(a)). The characteristic impedance of the transmission line in the model is approximately 65 Ω. This value is similar to the simulated characteristic impedance of the twisted line in a BHA. The resistor includes the effects of radiation resistance and ohm resistance, whose value equals 1.3 Ω (obtained by curve fitting compared with full- wave simulation.) The high permittivity of the ceramic rod makes the antenna very small as compared with the wavelength in free space, and decreases radiation resistance dramatically. The small radiation resistance means that the loss tangent of the ceramic rod becomes very critical to antenna efficiency.

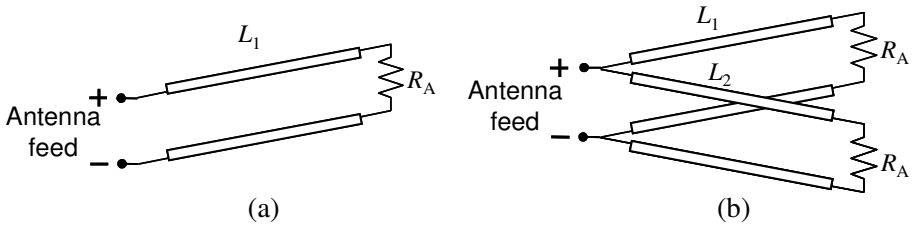

Figure 2.8 (a)The equivalent circuit of the proposed BHA. (b)The equivalent circuit of the proposed QHA.

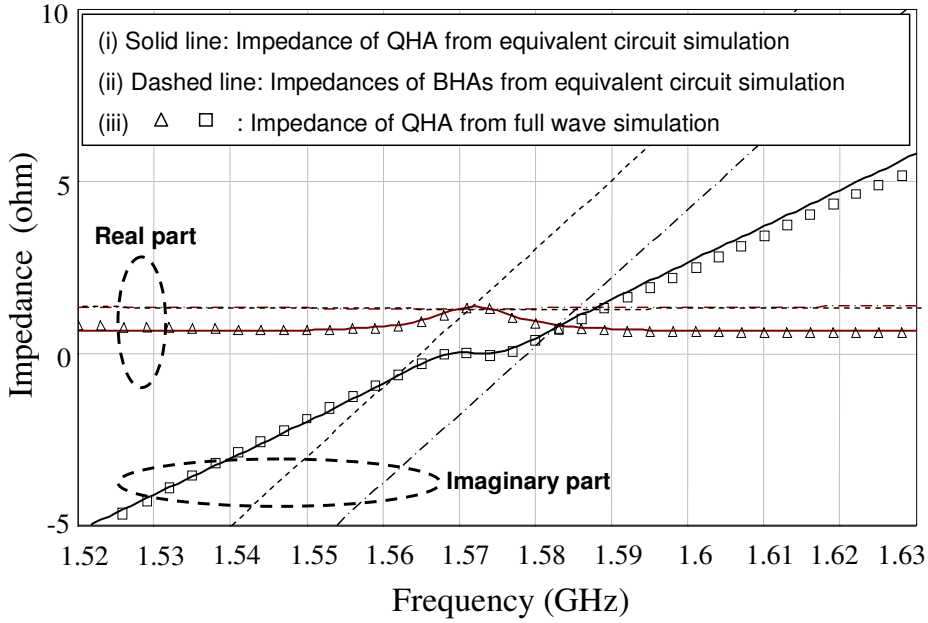

Figure 2.9 Impedances from full-wave simulation and equivalent circuit simulation.

A resonant QHA can be considered as two resonant BHAs arranged orthogonally with quadrature-phase excitation. To simplify the feeding network, the phase quadrature is obtained using the self-phasing method such that only one set of feeding lines is required. By this method, two BHAs are fed in parallel (Figure 2.8 (b)), with one BHA slightly larger than the other. In the proposed design, the electrical lengths L_1 and L_2 of the equivalent transmission line of the two BHAs are 180.8° and 179.2° at the QHA resonant frequency, what are inductive and capacitive, respectively, and cancel each other at the center frequency. The very small difference in length required to achieve circular polarization is based on the small input resistance of the antenna. To compare full-wave simulation result with the equivalent circuit, the input impedance of the un-matched antenna was de-embedded to eliminate parasitic inductance from feeding lines. Figure 2.9 plots the calculated input impedances of the BHA and QHA from equivalent circuits, and the input impedance of QHA from full-wave simulation, where the reference plane is set as reference plane 1 (Figure 2.7). The calculated result for the circuit model agrees with the full-wave simulation, and the impedance of the QHA is the impedance of two BHAs connected in parallel. Near the center frequency of the QHA, the impedance curve of an imaginary part becomes flat and the curve of the real part reaches a maximum. The corresponding Smith chart has a tip on the impedance curve around center frequency (Figure 2.10).

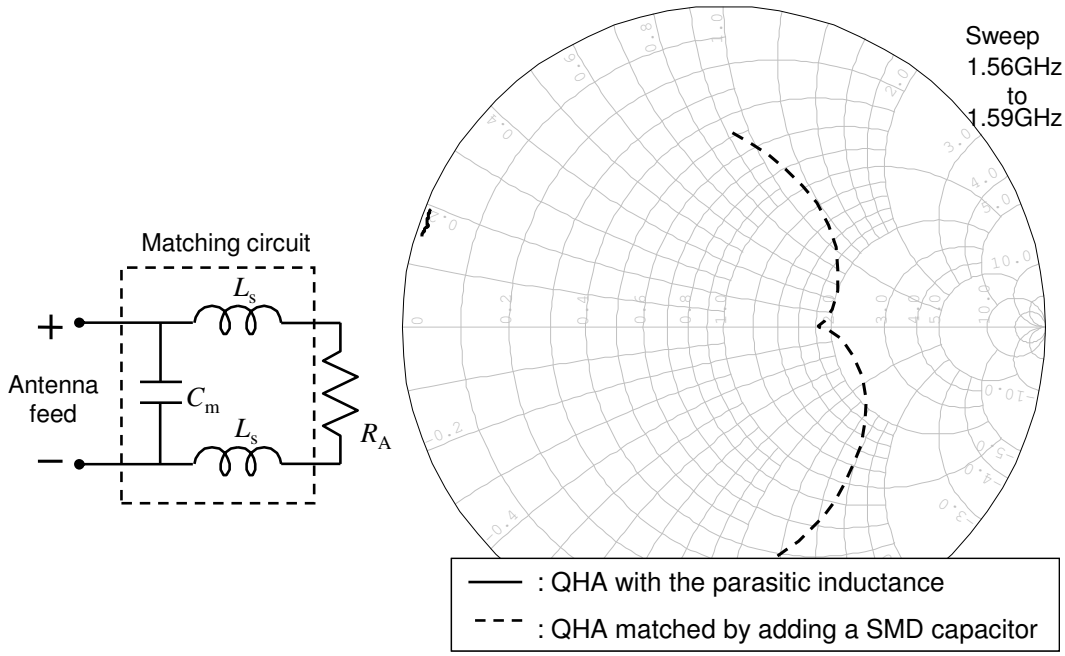

Figure 2.10 (a) Schematic diagram of the matching circuit. (b)The simulated input impedance of the antenna at reference plane 2. The solid line represents the antenna without the capacitor. The dashed line represents the antenna matched by adding the capacitor.

The small input resistance is a critical problem when feeding the proposed antenna. To transform a very small resistance to 100Ω, the efficiency of the matching circuit should be considered. Furthermore, the matching circuit should also be small such that the entire antenna is compact. Figure 2.10(a) shows the proposed matching circuit, in which two inductors and a capacitor are used to match antenna resistance RA of 1.3 Ω at the center frequency. To transform the small resistance to 100 Ω, the required value of the inductors and capacitor are 0.6 nH and 8.5 pF, respectively. Notably, a small inductor is utilized, which helps reduce loss and thereby increase the efficiency of the matching network. In practice, the two small inductors are implemented using two parasitic short sections of transmission lines. The large capacitor used is a surface mount device (SMD) component. The capacitor is shunted with feeding lines. Figure 2.7 presents the layout of the proposed matching configuration. The circuit size is very small and only one SMD component is used. By appropriately positioning the capacitor, the required length of the short matching transmission-line sections and, thus, the matching inductance can be obtained.

Figure 2.10(b) shows the simulated input impedances of the antenna, with and without the matching capacitor, at reference plane 2 (Figure 2.7). Without the

matching capacitor, the input impedance is near 1.3 Ω with a small inductive reactance provided by the short transmission line sections from reference plan 1 to 2 (Figure 2.7). After adding the capacitor, the impedance can be matched to 100 Ω at the center frequency. Matching circuit efficiency depends on the loss of components. Since the loss of a short transmission line section is quite low, it can be ignored. The parasitic resistor of the SMD capacitor is of greatest concern. According to the capacitor model from the Murata library [55], the parasitic resistance associated with an 8.5 pF capacitor is 0.33 Ω. The matching efficiency is at least 80%. To increase efficiency further, the single 8.5 pF capacitor can be replaced by two shunt 4.25 pF capacitors.

2.2.3 Experimental Results

In this work, a good RHCP pattern in the upper half space is designed. Figure 2.11 presents the method used to attain self-phased quadrature excitation for RHCP. Two feed points are connected to the feeding lines on a circuit substrate for a differential input signal. The circuit substrate is rotated by a small degree, θ, relative to the symmetric plane. After rotation, the lengths of two BHAs become different; this difference proportional to the rotational angle (Figure 2.11). However, average length of two BHAs remains the same, implying that resonant frequency will not change because the resonant frequency of a QHA depends on average length of the two BHAs. Rotation makes the length of one BHA longer than the average length and the other shorter. The longer BHA exhibits an inductive impedance at the center frequency and the shorter BHA shows capacitive impedance, which provides the required quadrature-phase excitation for circular polarization. To obtain the RHCP in the upper half space, θ should be positive; otherwise, a negative θ causes LHCP in the upper half space and RHCP in the lower half space.

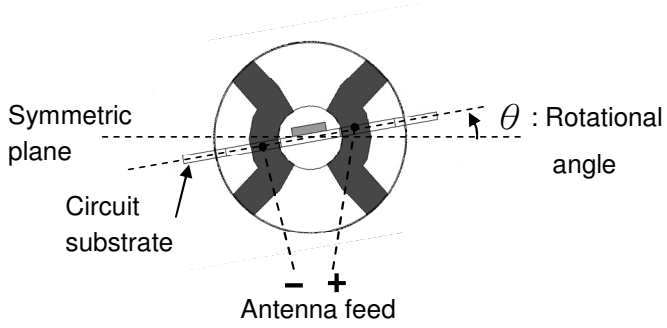

Figure 2.11 Rotation method rotates the circuit substrate for achieving circular polarization.

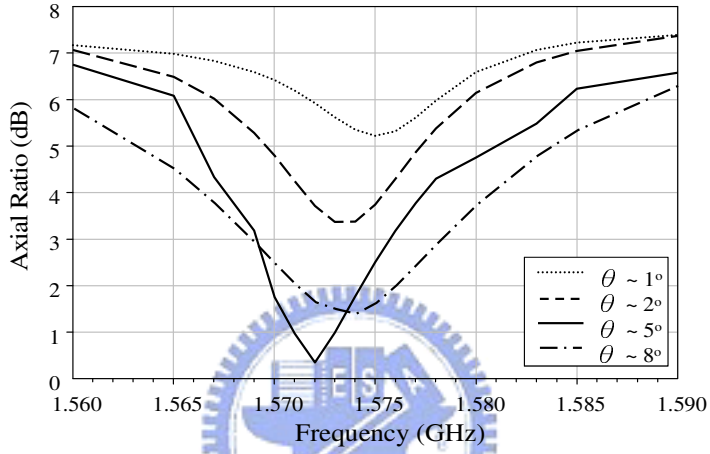

Figure 2.12 The simulated axial ratio compared with different rotational angles.

A set of simulations for different rotational angles was conducted to identify a suitable θ for good circular polarization. Figure 2.12 presents simulation results; the frequency responses of the axis ratio for θ from 1–8° are shown. The circular polarization improves when the rotational angle approaches 5°, and then worsens as the angle is increased further. Although not shown, the simulated axial ratios for θ = 0° are large (30–40dB), meaning that the radiation field is primarily linearly polarized. Notably, the 3-dB axial ratio bandwidth when θ = 8° is wider than that when θ = 5°; however, θ = 5° has the best axial ratio at the center frequency. Figure 2.13 shows the variation of impedance for different rotational angles. Since the impedance before matching is quite small, the simulations include the matching circuit for enhanced observation. When θ is around 5°, the minimum axial ratio is achieved, and the circular polarization occurs at the tip (1.572 GHz) of the Smith chart. When exceeds 5 °, a circle instead of a tip occurs on the impedance curve. The formation of the tip is observed when checking the self-phasing state.

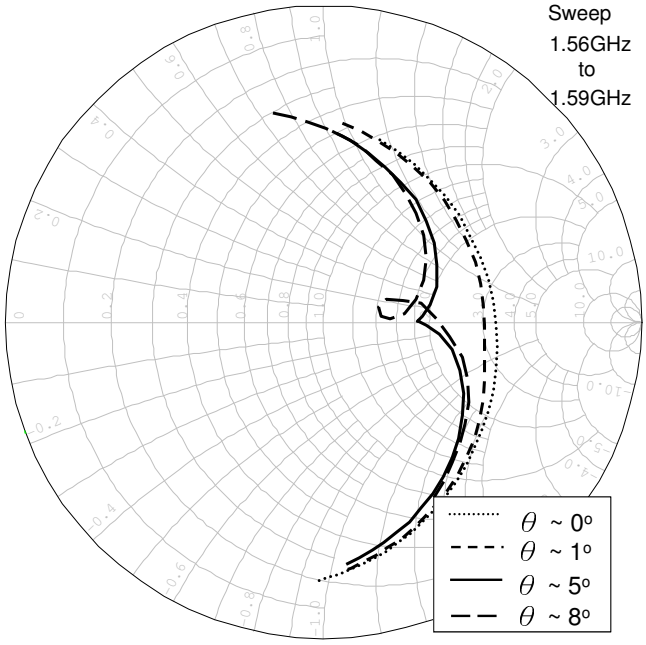

Figure 2.13 The simulated impedances with different rotational angles.

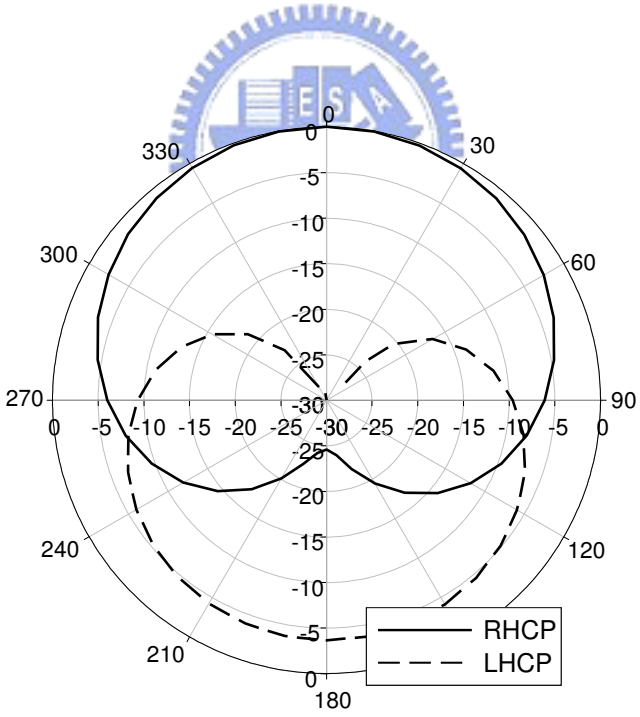

Figure 2.14 The simulated radiation pattern when rotational angle is 5°.

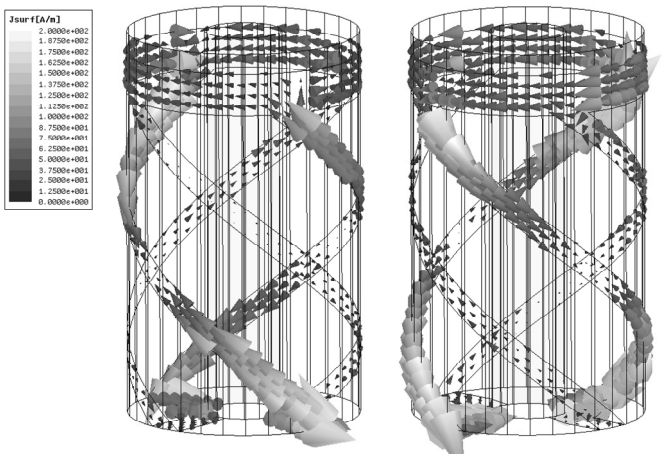

Figure 2.15 The current distribution of the proposed antenna with input phases of (a)0° and (b)90°.

The input impedance bandwidth of the proposed antenna is determined by the matching structure. By using the matching circuit, the simulated 10-dB return-loss bandwidth for θ = 5° is 12 MHz, which is wider than the corresponding 3-dB axial-ratio bandwidth (7 MHz). Both the small impedance and axial-ratio bandwidths result from the small radiation resistance. Nevertheless, both the bandwidths are sufficient for application on the GPS L1 band. Figure 2.14 shows the normalized simulation radiation pattern at the center frequency. A good semi-spherical circular polarized pattern is obtained, which has a 3-dB beamwidth as wide as 130°. The good cardioid-shaped radiation pattern demonstrates that the overlapping region of two BHAs with a top metal ring does not influence radiation performance that is similar to that of the conventional resonant QHA. It also shows that the RHCP gain is 4 dB higher than the LHCP gain. This result agrees with the helix design of left-handed orientation. Figure 2.15 plots the simulated current distribution of the QHA at 1.572 GHz. The current distribution of each BHA is one-wavelength resonance, just like a loop antenna. At the center frequency, where circular polarization occurs, the two BHAs resonate in phase quadrature as predicted. The closed loop resonance for each BHA is accomplished using the top metal ring.

The proposed antenna was fabricated for experiments. The antenna is fixed to the circuit board via the protrusion. A microstrip Balun with 2:1 impedance transformation provides the differential signal. The SMD capacitor used for impedance matching is a Murata GRM1885C1H6R8DZ01¬. As mentioned, the impedance-matching inductors are realized by two short microstrip-line sections,

whose lengths are determined by the shunt capacitor location. By properly tuning the capacitor position, the return loss of the antenna matched better than 10 dB at the center frequency. Figure 2.16 presents the measured input impedances with rotational angles of 0°, 4°, and 8°. The condition of $\theta = 0°$ indicates that the two BHAs are the same length and the corresponding impedance curve changes monotonously, as predicted in the simulation. The antenna with the best circular polarization, where the axial ratio is 0.8 dB, is measured when the rotational angle is 4°, where a tip at the center frequency of 1.592 GHz forms in the impedance curve. The shift of resonant frequency and the required rotational angle is mainly due to manufacturing tolerance of ceramic permittivity and metal printing. When the rotational angle is increased to 8°, a circle rather than a tip occurs in the curve near the center frequency. Under this condition, the impedance bandwidth widens at the expense of degraded circular polarization; this is tradeoff between circular polarization quality and impedance bandwidth. Additionally, the center frequency remains the same with different rotating angles (Figure 2.16). The self-phasing method used is convenient for tuning circular polarization without changing the center frequency.

Figure 2.17(a) presents a photograph of the finished antenna, and Figure 2.17(b) depicts the measured radiation pattern at 1.592GHz with a 4° rotational angle. The radiation pattern is measured using an RHCP standard antenna. The semi-spherical pattern is omni-directional in the horizontal plane and agrees with that simulated. The corresponding 3-dB beamwidth is 150°, which is sufficiently wide for practical applications. The measured peak gain is −4.3 dBic and the 3-dB axial ratio bandwidth is 8 MHz.

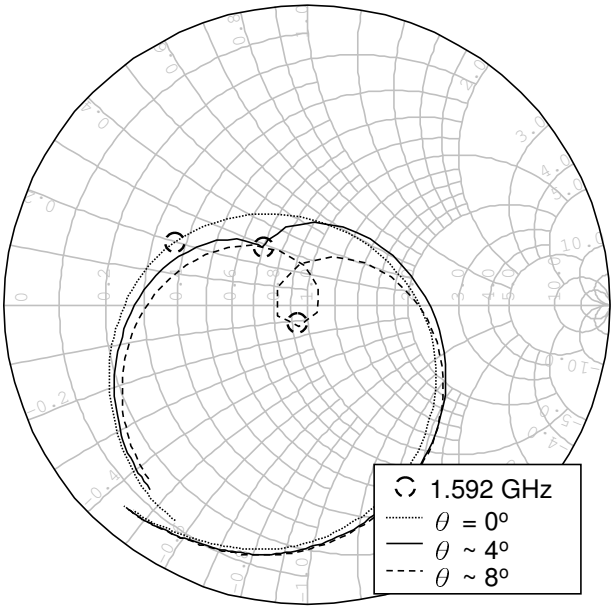

Figure 2.16 The measured impedances with different rotational angles.

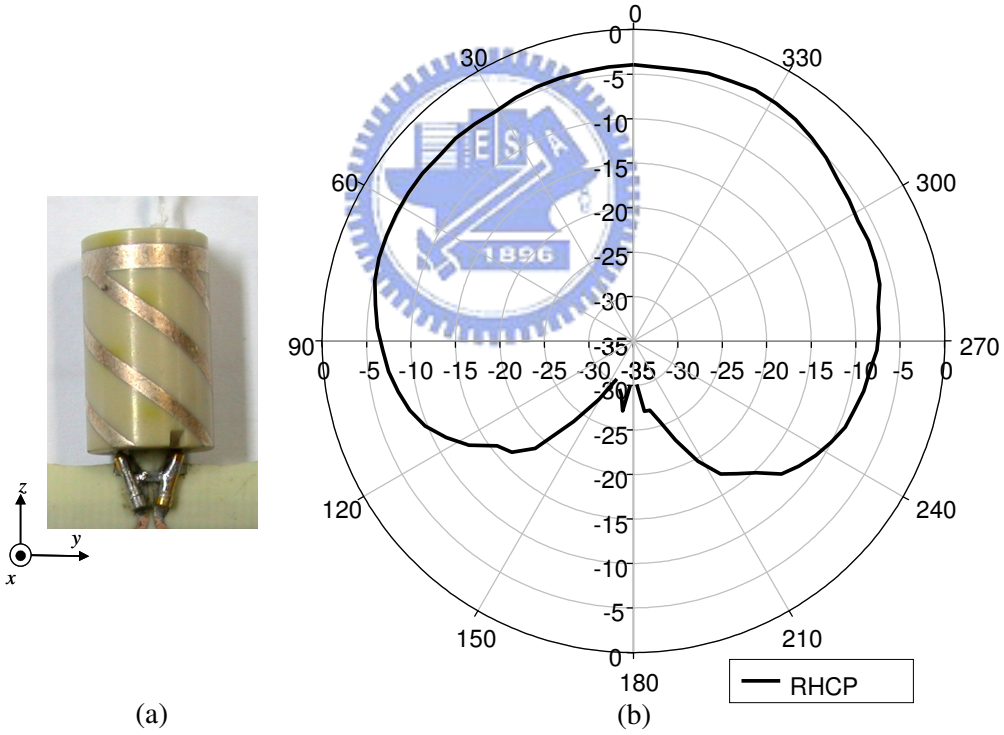

(a) (b)

Figure 2.17 (a)Photograph of the realized antenna. (b)Measured radiation pattern of the proposed antenna at 1.592 GHz.

2.2.4 Summary

A semi-spherical circular-polarized radiation pattern and reasonable gain for proposed QHA were achieved. The proposed self-phasing method for achieving circular polarization was flexible when tuning the axial ratio while retaining the same resonant frequency. Experimental results agree well with simulation results. The differential signal for antenna feeding can be provided by a LC Balun or a differential amplifier. The small input resistance of the miniaturized QHA has been matched successfully via a simple structure without occupying additional area. Both the feeding and matching structures are quite small, low cost and simple to manufacture, and easily integrated into circuit boards.

Chapter 3 Miniaturized Antennas with Circuit Resonances

3.1 Short Slot Radiator Utilizing a Right/Left-Handed Transmission Line Feed

Rather than employing CRLH or simply LH TL as mentioned in Chapter 1, a novel planar antenna utilizing cascaded right/left-handed transmission lines is proposed as sketched in Figure 3.1. The design concept is inspired from metamaterial antennas. Two cascaded transmission lines of equal amount of electrical length with opposite polarities, i.e. a section of RH TL and a section of LH TL, can also result in phase of zero degree as shown in Figure 3.2. With using the equivalent transmission line circuits, one can realize compact antennas consisting of printed inductors (L) and capacitors (C) on a printed circuit board without via. The physical dimensions of the antenna are decided by the values of the inductances and capacitances. The layout planning has significant influences on the implementation of such radiating structures.

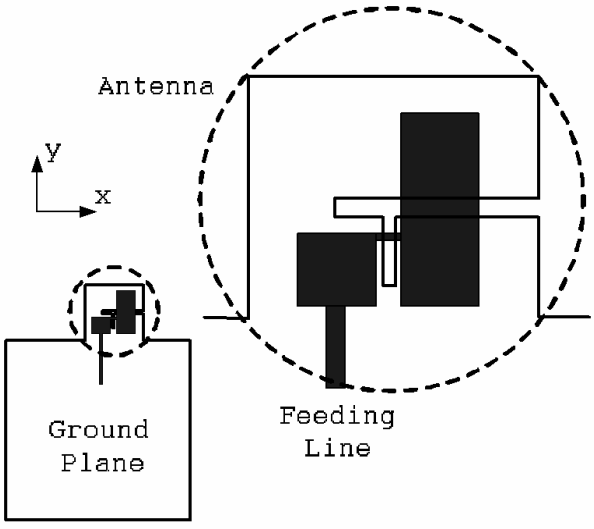

Figure 3.1 Geometry of the proposed planar antenna.

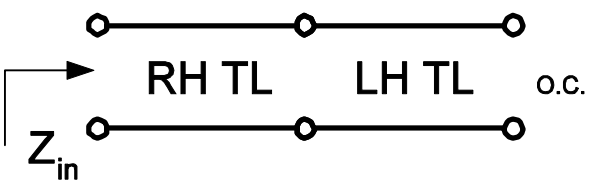

Figure 3.2 Cascaded right/left-handed transmission lines.

3.1.1 Equivalent Transmission Line Model

The design starts with cascading a section of RH TL and a section of LH TL. The former one has a positive electrical length indicating phase delay whereas the latter one has a negative electrical length indicating phase advance. One port is pen-circuited as illustrated in Figure 3.2. The input impedance (Z_{in}) possesses zero imaginary part, which is one of basic requirements for a resonant antenna. By employing the equivalent circuit model for a TL section, one can realize it with lumped circuits. With the specified characteristic impedance Z_0, the operation frequency f_0, and the electrical length θ, it is well-known that a certain length of transmission line can be modeled by either π or T equivalent circuit. Figure 3.3 shows the circuit models with

$$\begin{aligned} Y_{\pi 1} &= jY_0(\csc\theta - \cot\theta) \\ Y_{\pi 2} &= -jY_0 \csc\theta \\ Z_{T1} &= jZ_0(\csc\theta - \cot\theta) \\ Z_{T2} &= -jZ_0 \csc\theta \end{aligned} \tag{3-1}$$

where $Y_0=1/Z_0$. These formulas can be easily derived by comparing the ABCD matrix for TL section with the ABCD matrix for π and T circuits at the design frequency. The susceptances of $Y_{\pi 1}$, $Y_{\pi 2}$ and the reactances of Z_{T1}, Z_{T2}, as functions of the electrical length θ, for the normalized component values with $Y_0=1$ and $Z_0=1$ are sketched in Figure 3.4. The upper half plane in Figure 3.4(a) and the lower plane in Figure 3.4(b) indicate capacitive elements whereas the lower half plane in Figure 3.4(a) and the upper plane in Figure 3.4(b) indicate inductive elements.

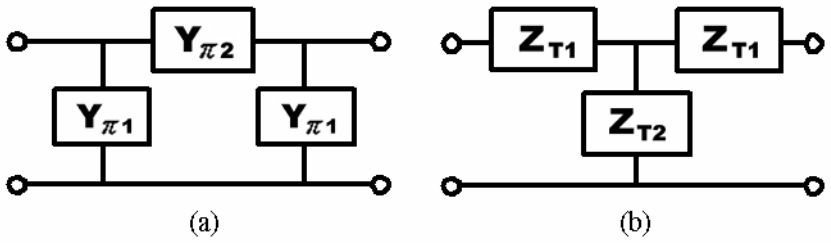

Figure 3.3 (a) π and (b)T equivalent circuit for a reciprocal two-port network.

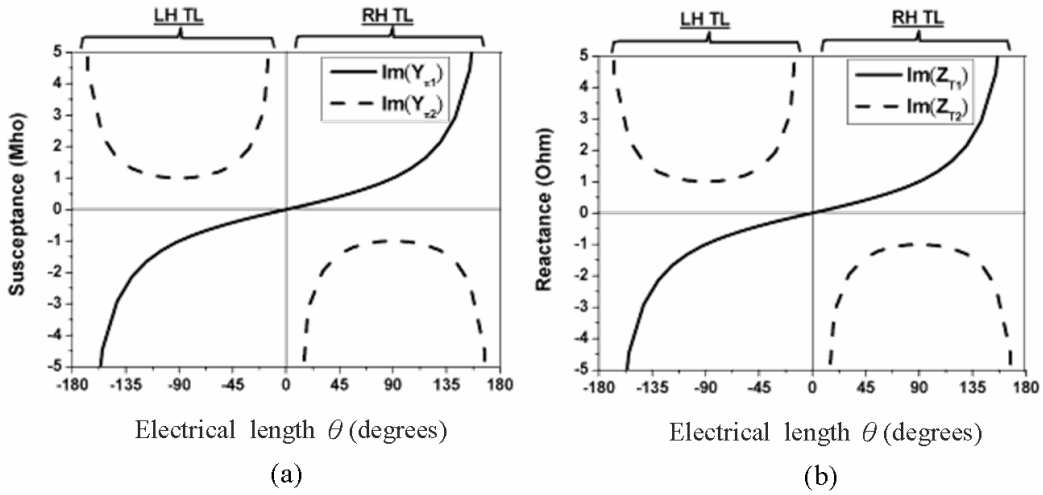

Figure 3.4 (a)Susceptances of $Y_{\pi 1}$, $Y_{\pi 2}$ and (b)reactances of Z_{T1}, Z_{T2}, as functions of the electrical length θ, for the equivalent circuits of Figure 3.3 $Y_0 = 1$ and $Z_0 = 1$.

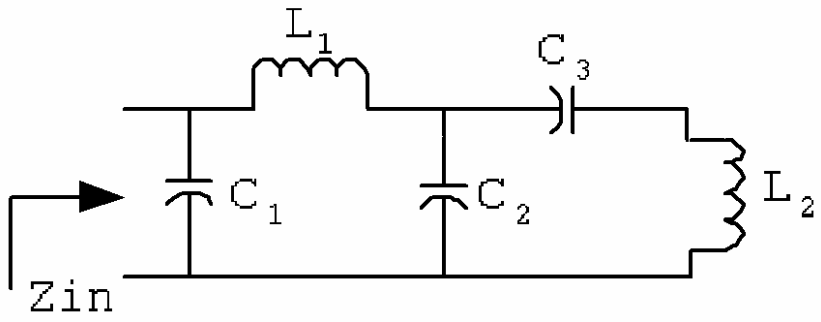

Figure 3.5 Cascaded circuit structure consisting of a π model for RH TL and a T model for LH TL. The last series capacitor of the T circuit has been removed since it is connected to the open-circuit end.

3.1.2 Antenna Synthesis and Radiation Mechanism

Following the previous section, formulas for the inductors (L) and capacitors (C) of the equivalent transmission line model are listed in Table 3-1, where $\omega_0 = 2\pi f_0$. The notation $L_{L\pi}$, for example, represents the value of the inductor of the π model for LH TL. Since each TL segment in Figure 3.2 can employ either π or T circuit, there are four combinations in total. A π circuit for RH TL and a T circuit for LH TL are chosen and connected with an open-circuit at the unconnected port of the LH TL. This can results in a via-free layout which does not require an extra fabrication process. The last series capacitor of the T circuit can be removed since it is connected to the open-circuit end. As shown in Figure 3.5, it turns out the circuit for designing the proposed antenna with $C_1 = C_2 = C_{R\pi}$, $L_1 = L_{R\pi}$, $C_3 = C_{LT}$, and $L_2 = L_{LT}$.

In order to have a compact structure, the design of the circuit parameters was considered. Referring to Figure 3.4, choosing θ close to either 0 or 180 degrees leads to very large L or C value. Therefore, θ is chosen to be 90 degrees so as to keep a small circuit area. In addition, since many published antennas using metamaterial concepts, mentioned in Chapter 3.1.1, possess patch or patch-like radiation patterns, this study goes with introducing relatively larger capacitors rather than larger inductors. In case of avoiding large inductors and mainly having patches in the physical structure, a relatively small Z_0 is preferred. Based on these conditions, several layout types were developed and compared to find the optimal topology.

EQC	Formulas for L	Formulas for C
π LH	$L_{L\pi} = \frac{Z_0}{(\csc\theta - \cot\theta)\omega_0}$	$C_{L\pi} = \frac{1}{Z_0\omega_0 \sin\theta}$
π RH	$L_{R\pi} = \frac{Z_0 \sin\theta}{\omega_0}$	$C_{R\pi} = \frac{(\csc\theta - \cot\theta)}{Z_0\omega_0}$
T LH	$L_{LT} = \frac{Z_0}{\omega_0 \sin\theta}$	$C_{LT} = \frac{1}{Z_0\omega_0(\csc\theta - \cot\theta)}$
T RH	$L_{RT} = \frac{Z_0(\csc\theta - \cot\theta)}{\omega_0}$	$C_{RT} = \frac{\sin\theta}{Z_0\omega_0}$

Table 3-1 The formulas of L and C for a TL section.

To perform the antenna layout, the following design procedure is adopted. The first is to determine the operation frequency, the electrical length, and characteristic impedance of the RH and LH transmission lines. Here, the operation frequency is 2.45 GHz and the characteristic impedance (Z_0) of the LH and RH TLs is set to be 25 Ohm. The second is using the circuit model to determine the values of required inductors and capacitors. This can be done by applying Table I. It turns out that all the three capacitors have the same value of 2.6 pF and both of the inductors have the same value of 1.62 nH at 2.45GHz. The third, the most important step, is to realize these capacitors and inductors by using printed elements. The capacitors are patches against the ground with proper size to fit the value of capacitance. The equation of the parallel plate capacitor can be used to get the initial sizes of the patches. The inductors are implemented by metal traces or metal traces with slotted ground. The lengths of metal traces and the sizes of the slots are designed by EM simulator to fit the value of inductance. Finally, the obtained printed capacitors and inductors are connected properly according to the circuit model. The arrangement of these elements is important for antenna performance. The layout consideration becomes the point of this antenna design. For planning the layouts, full wave EM simulation is done by utilizing the commercial software, Ansoft HFSS. Three possible layouts are considered for comparison as follows. The layout is made on a two sided FR4 substrate with relative dielectric constant of 4.4 and thickness of 0.4 mm.

A compact antenna structure based on the circuit in Figure 3.5 is proposed as illustrated in Figure 3.6 with the corresponding elements marked. The solid lines are for the top metal layout and the dashed lines are for the bottom layout. The rectangular patches are obviously planned to realize the capacitors. The narrow short metal traces dominantly contribute as inductors. This layout arranges the C_1, L_1, C_2, C_3, and L_2 in turn forms a closed loop and intend to create the longer slot on the ground plane. The geometry parameters are $L = W = 11.5$ mm, $w_C = 4$ mm, $l_{23} = 9.5$ mm, $g = 1.3$ mm, $l_{S1} = 7.2$ mm, $l_{S2} = 3.2$ mm. Instead of a narrow short trace, the small inductor L_2 is realized by a wide and longer metal trace. Besides, a slot of width of 0.5 mm under L_1 is introduced and observed to provide a wide tuning range for the input resistance by changing the slot length l_{S2}.

Two other possible layouts, named the type A and B, are shown in Figure 3.7(a)

and Figure 3.7(b), which are made also on the same FR4 substrate. For the type A layout, the bottom pattern is a wide trace of 5.5 mm in width with, of course, a narrow trace for L_2. The top pattern is a less wide trace of 3.5 mm in width also with a narrow trace of 2.5 mm in length for L_1. The type B layout has quite similar dimension with the type A layout but its wide traces go along an edge of the ground plane. The trace for L_2 is directly connected to the ground plane. The dimension along the *y* axis of the straight type A antenna is 18.5 mm and the dimension along the *x* axis of the straight type B antenna is 18 mm. It can be roughly interpreted that the proposed layout is obtained by bending the straighter layout as the type A or B. It should be mentioned that all the three layouts have finite ground planes of 40 mm (*y*-direction) by 30 mm (*x*-direction) in size, extended in the negative *y* direction and partly ignored in the figures for simplicity of illustration.

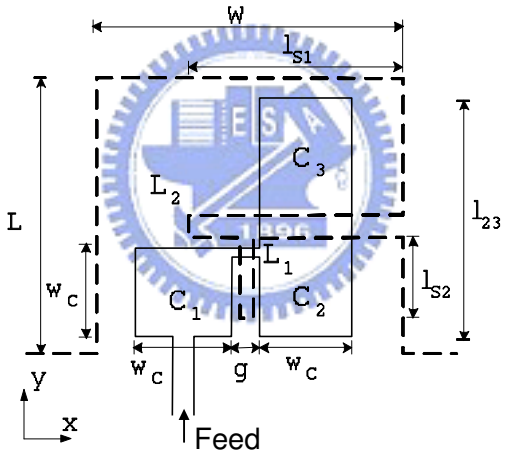

Figure 3.6 Layout of the proposed antenna. The dashed lines are for the bottom metal layout and the solid lines are for the top metal layout.

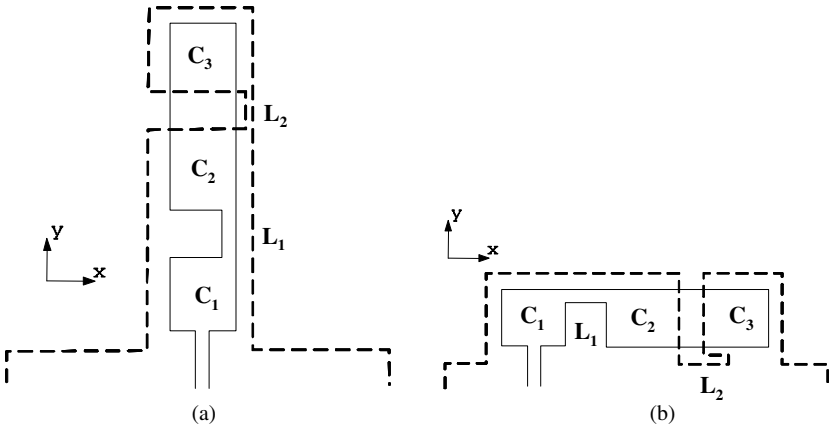

Figure 3.7 Layouts of (a) straight type A antenna and (b) straight type B antenna. The dashed lines are for the bottom metal layout and the solid lines are for the top metal layout.

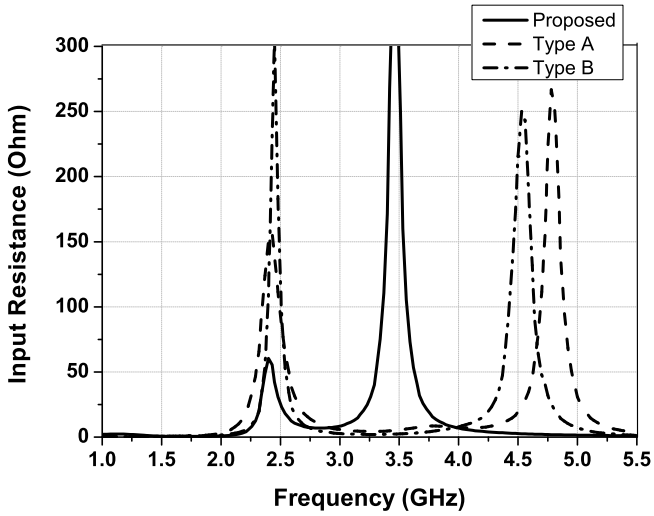

(a)

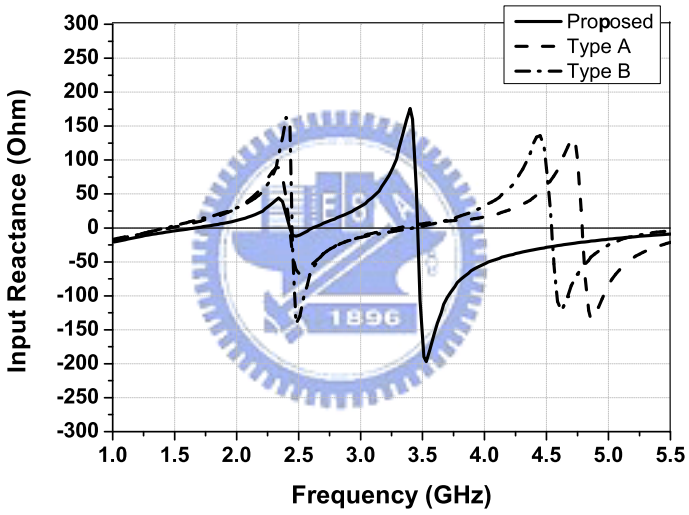

(b)

Figure 3.8 Simulated (a)input resistance and (b)reactance for the proposed, type A, and type B antennas.

Different layouts may cause different electric field and current distributions, thus affecting the radiation performance. Figure 3.8 shows the simulated input impedances of all the three antenna layouts. At the design frequency of 2.45 GHz, all of them possess an anti-resonance, (or a parallel resonance) as can be observed from Figure 3.8(b) where the curve for the input reactance have a zero crossing with a negative slope at that frequency. However, apparent differences of the real parts are observed. The real part of antenna input impedance usually reflects the radiation performance for easy matching with good radiation efficiency. Thus the layout planning has

significant influences on providing efficient radiating structures while employing the cascaded right/left-handed transmission lines. It is observed that a second anti-resonance occurs around the harmonic frequency (4.5 GHz) for both the type A and B antennas with straight layout. This second anti-resonance also happens in the proposed antenna, however, at a lower frequency of 3.5 GHz. Since the design and analysis focus on the performance at the desired fundamental frequency, other resonances are not taken into account in this paper.

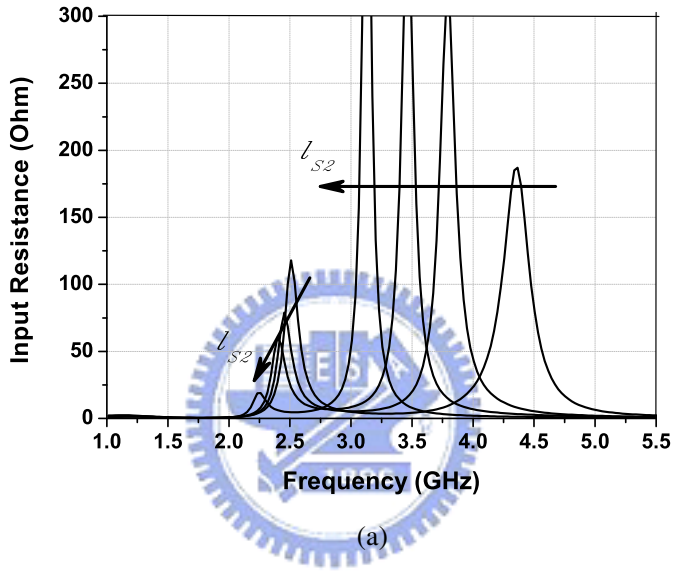

(a)

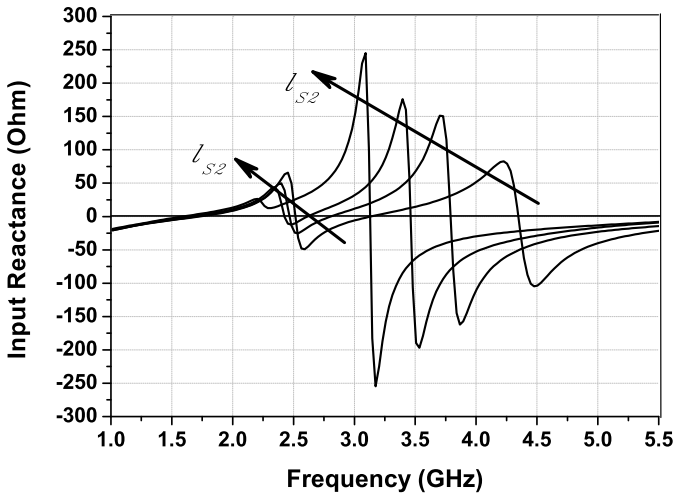

(b)

Figure 3.9 Simulated (a) real part and (b)imaginary part of the input impedance, with changing the slot length l_{S2} under L_1, for the proposed antenna. l_{S2} = 1.5, 3.0, 3.5, 4.5 mm.

The most difference between these three layouts is considered as the topology of the ground. The proposed antenna structure can be interpreted as closing the layout for L_2 to the bottom side of C_1. The surface electric current flow is guided roughly in a loop in the order of C_1, L_1, C_2, C_3, L_2 and then back to C_1. In contrast, the type A and B is extended straightly without closing the ground plane to the bottom side of C_1. This difference causes the proposed layout introduces longer slot on the ground plane which may have significant influences on inducing radiating current on the ground efficiently. It is found that the slot length, l_{S2} of the proposed layout, can be used to reduce the input resistance of the antenna from hundreds of ohms to a few ohms with unapparent changing of resonant frequency shown in Figure 3.9. It proves the influence of the radiation from the proper slot on the ground plane. In addition, the proposed antenna can be easily matched.

Besides the consideration of the slot, the patches as capacitors which occupy the main area of the antenna are also studied. An individual patch of small size with respect to the wavelength can only generate negligible far field radiation since the equivalent surface magnetic current ($\mathbf{M_S}$) at the edges results in canceling each other at bore sight direction. A surface magnetic current $\mathbf{M_S}$ is defined by

$$Ms = E \times \hat{n} \tag{3-2}$$

where $\mathbf{E}$ is the electric field, and $\hat{n}$ is the outward normal of the side walls for capacitor patches or the normal vector to the surface of the slots. The proposed layout (Figure 3.6) has a topology of patches at the top and slots at the bottom. The bottom pattern could be considered as the extended ground with two connected orthogonal slots. The capacitors confine electric energy and provide fringing fields at their edges. As seen in Figure 3.10(a), the simulated electric fields for C_2 and C_3 possess opposite polarities, i.e. the electric field vectors for C_2 points upward if those for C_3 points downward. The opposite polarities make the equivalent magnetic current flow from C_2 goes counterclockwise while that from C_3 goes clockwise, as indicated by the double-headed arrows of Figure 3.10(b). The radiation fields from the close and opposite directed pairs of the magnetic currents cancel with each other. Therefore, as a result, here are two edges at the top constructively contributing to radiation. These two edges provided by C_2 and C_3 at the top side operate as the radiating edges of a conventional half-wavelength patch antenna. In other word, this design shrinks

the dimension from half wavelength to one-eleven wavelength. Moreover, there are two connected slots at the bottom side offering aperture electric field for constructing radiation. The contribution provided by C_1 is not taken into account since its field strength is very weak. Regarding the type A, it plans three patches in a row with two short traces. The corresponding simulated electric fields and equivalent magnetic currents are shown in Figure 3.10(c) and (d), respectively. The magnetic currents provided by C_1 cancel each other in the far field since they are close and opposite directed in pairs. The fringing field from C_2 is too weak to contribute. Two remaining edges provide equivalent magnetic currents in the same direction. One is from the slot at the bottom side between C_2 and C_3. The other one is the upper edge of C_3, which is close and parallel to the slot one. The type B has very similar field distribution with the type A.

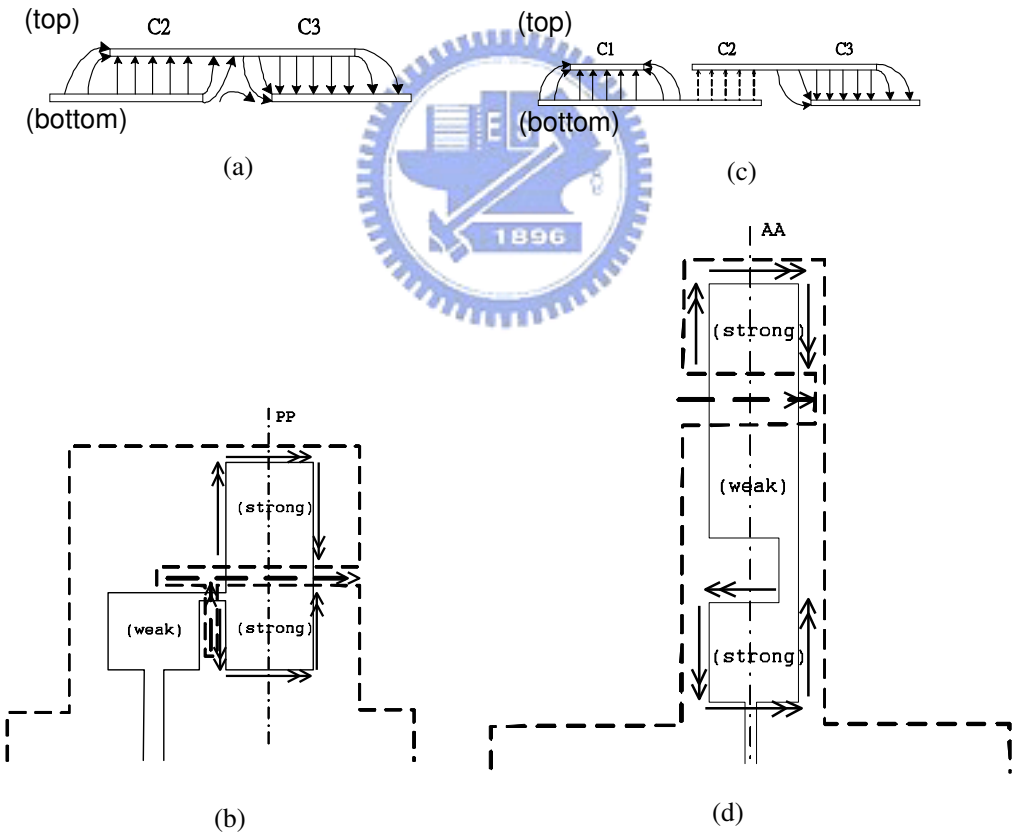

Figure 3.10 (a)Schematic for the electric field distribution at the PP cut for the proposed antenna. (b) Schematic of the equivalent magnetic current distribution for the proposed antenna. (c)Schematic of the electric field distribution at the AA cut for the type A antenna. (d)Schematic of the equivalent magnetic current distribution for the type A antenna.

3.1.3 Experimental Results

For experimental verification, both the type A and the proposed structure are fabricated and measured. These two printed antennas were implemented on an FR4 substrate with relative dielectric constant of 4.4 and thickness of 0.4 mm. The proposed antenna results in occupying an area of 11.5 mm by 11.5 mm with a connected ground size of 40 mm by 30 mm. The type A has the size of 5.5 mm by 18.5 mm with the same ground size as the proposed one. As the simulation result predicted, the input resistance of the type A antenna is about 150 Ω, which is relatively large for the 50-Ω system. Thus, an extra quarter-wavelength high impedance line is added between C1 and the 50-Ω microstrip feeding line for impedance transformation. Figure 3.11 shows the measured and simulated return losses, as functions of frequency, for the proposed antenna and the type A antenna. Both of the measurement results shift a little in frequency from the desired 2.45 GHz. The proposed antenna exhibits a resonant frequency at 2.23 GHz with the measured return loss of 23 dB, whereas the type A antenna is at 2.35 GHz with a return loss of 16 dB. The corresponding 10-dB return loss bandwidths are 4.5% and 5.3%, respectively. Figure 3.12 and Figure 3.13 show the measured radiation patterns for the proposed antenna and the type A antenna, respectively, in the three principal planes. The peak gain is +0.16 dBi for the proposed antenna and is -0.54 dBi for the type A antenna.

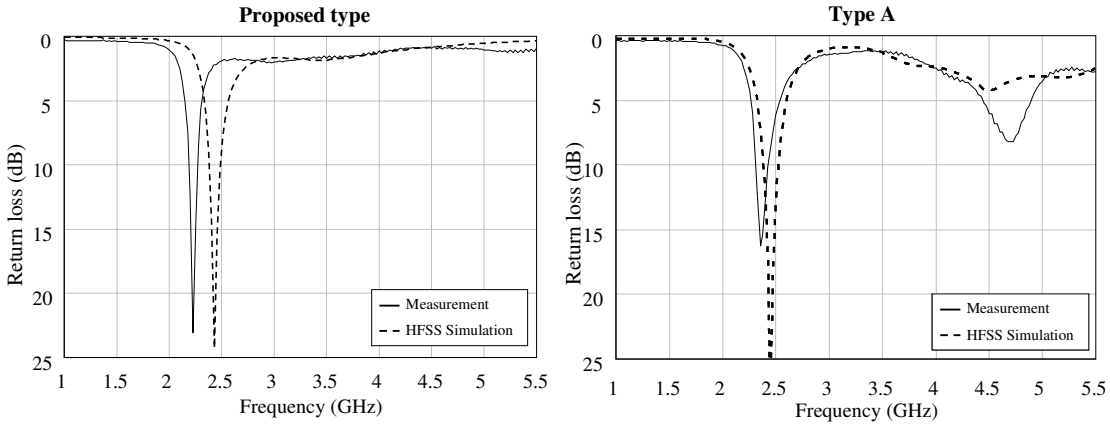

(a) (b)

Figure 3.11 Simulated and measured return loss for (a)the proposed antenna and (b)the type A antenna.

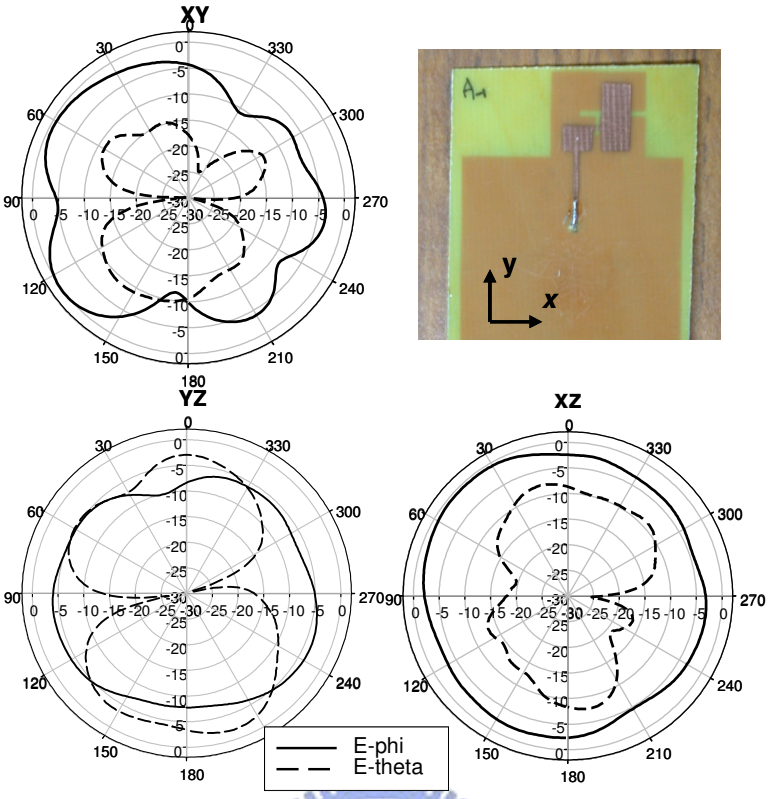

Figure 3.12 Simulated and measured radiation patterns for the proposed antenna.

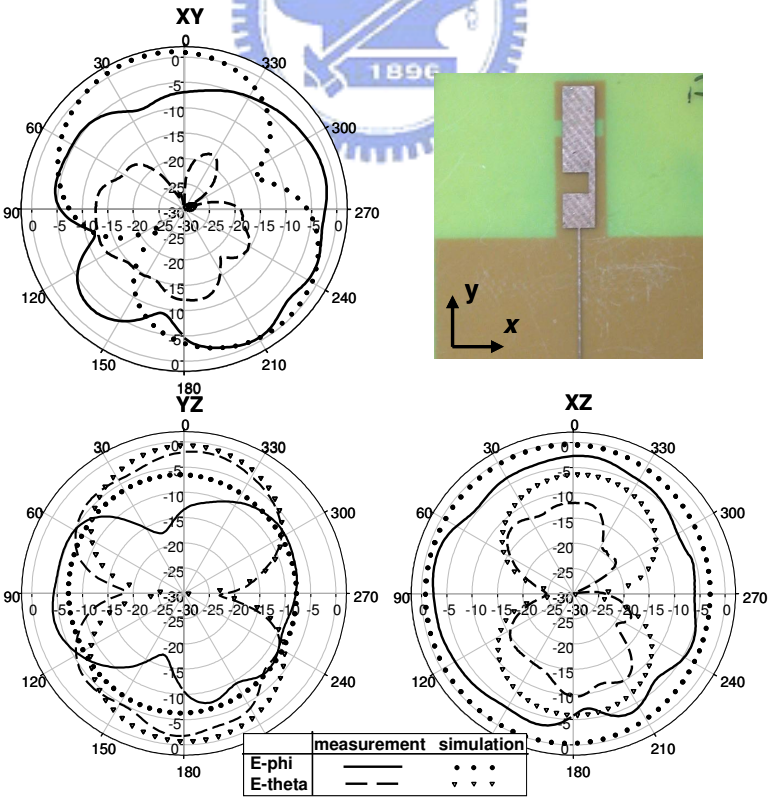

Figure 3.13 Simulated and measured radiation patterns for the type-A antenna.

To further understand the influence of the small patches on the radiation performance, two antennas, which have the same layout as the proposed antenna but with the printed capacitors in one antenna replaced by lumped capacitors (Figure 3.14 (a) and (b)), were designed and measured for comparison. Both antennas use same ground plane design with the same slots and equivalent capacitors and inductors. The measurement results and the photos of the antennas are shown in Figure 3.14. The input resistance of the antenna with lumped capacitor is a little less than the other at the center frequency, as can be observed from Figure 3.14(c) and (d). Also from Figure 3.14(e) and (f), it is seen that, the radiation patterns of the two antennas are quite similar, which means that the capacitor patches do not contribute significant radiation. Most of the radiation comes from the ground slots and the induced currents along the ground edges. Nevertheless, it is still noticeable that the theta component of the electrical field of the antenna with patch capacitors is about 2 dB larger than that of the antenna with lumped capacitors.

Through careful design and layout planning, the proposed antenna physically formed by small patches and slots can offer fairly good performance with a compact dimension of $\lambda_0/11$ square, where λ_0 is the free space wavelength. Finally, due to the self-resonance of the antenna configuration, the resonant frequency of the proposed antenna is insensitive to the ground size, as can be observed from the measurement results shown in Figure 3.15. Here, three antennas with the ground sizes of 70 mm by 45 mm, 40 mm by 20 mm, and 27 mm by 25 mm using same antenna layout are measured and compared. It is seen that the resonant frequencies of the three antennas are almost the same. It proves that the ground size has negligible effect on the resonance of the proposed antenna structure. As a reference, three typical printed quarter-wavelength monopole antenna with different ground sizes have also been developed for comparison. The antennas have the same monopole strip size of 27 mm by 1.6 mm and with ground sizes of 70 mm by 45 mm, 40 mm by 20 mm, and 27 mm by 25 mm, respectively. Although not shown here, the center frequency of the monopole antenna varies with the change of the ground size from 2.35GHz to 1.99GHz. A 16.5% frequency offset is observed.

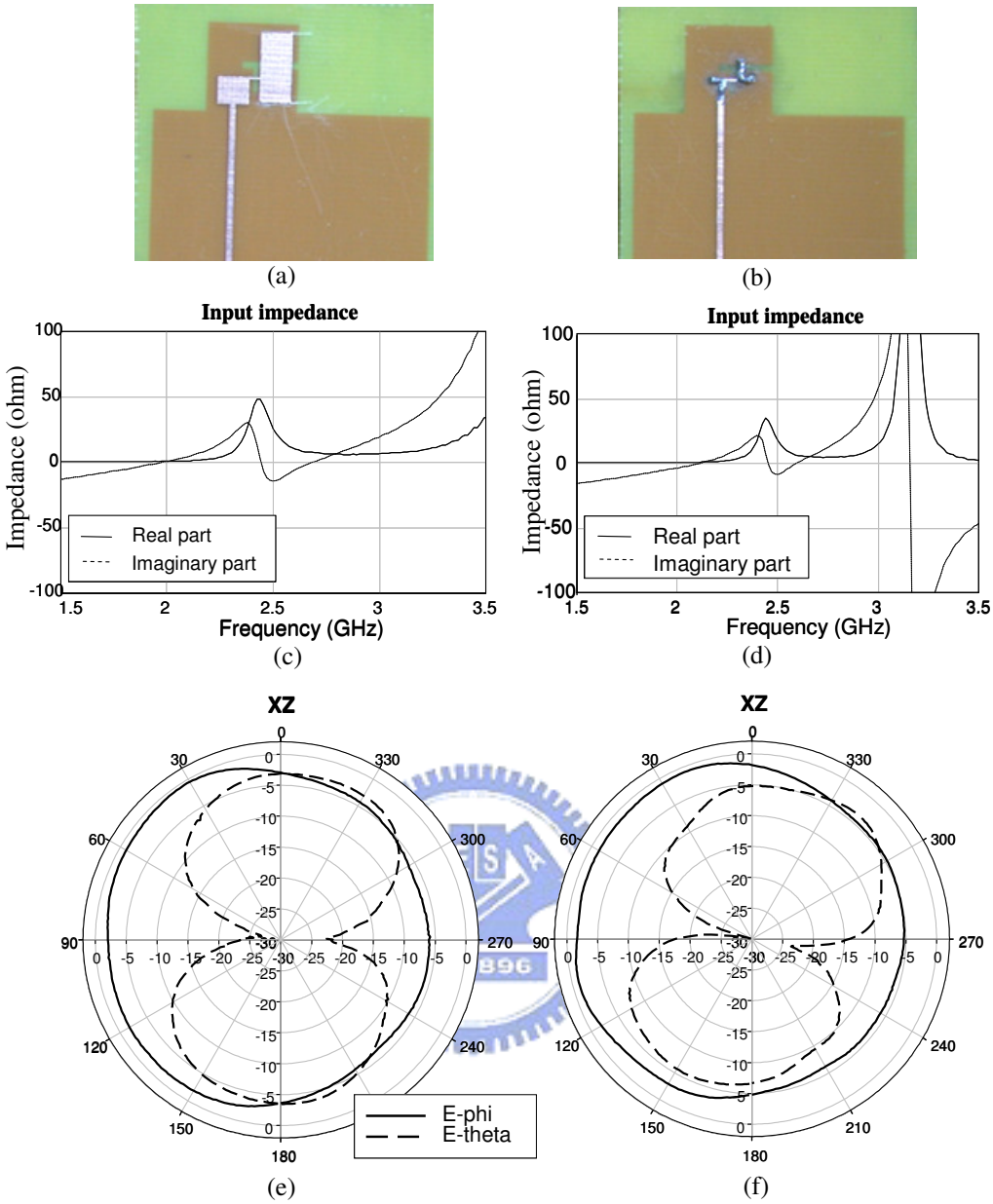

Figure 3.14 (a)The realized proposed antenna layout with printed elements. (b)The realized proposed antenna layout with lumped capacitors. (c)The measured input impedance of the antenna with printed element. (d)The measured input impedance of the antenna with lumped capacitors. (e)The measured radiation pattern of the antenna with printed element in x-z plane. (f)The measured radiation pattern of the antenna with lumped capacitors in x-z plane.

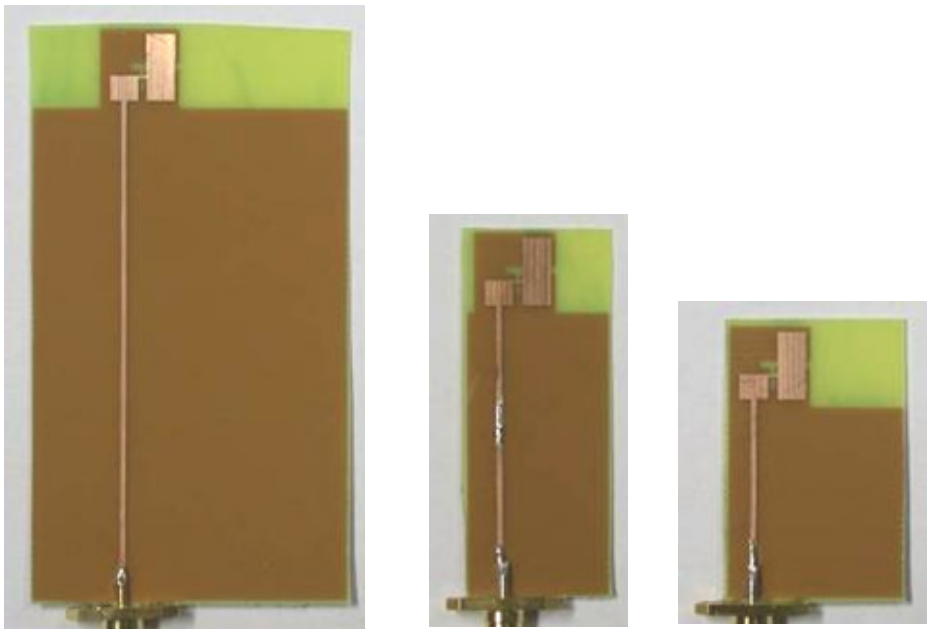

(a)

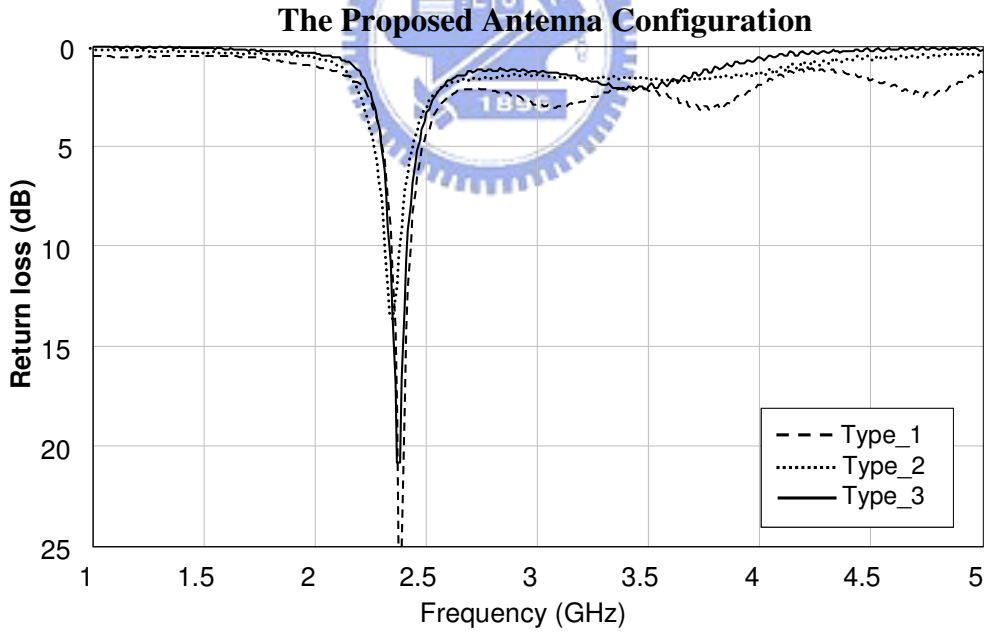

(b)

Figure 3.15 (a)The proposed antenna configuration with different ground sizes. (b)The return loss of the proposed antenna configuration with different ground sizes.

3.1.4 Summary

A novel compact planar antenna is designed and verified experimentally. Fairly good measurement results are obtained. Layout planning plays a crucial role for radiating as discussed. Different layouts for the same circuit model can cause different performances. This paper shows the possibility to design compact antennas based on cascaded right/left-handed transmission lines. Through applying the equivalent transmission line model, the physical dimension can be compact with a size are small as $\lambda_0/11$ square. In this paper, the proposed antenna avoids via and consists of only five lumped elements by the selection of the EQC model combination. The π and T models can offer exact formulas for L and C for almost all-range electrical length, θ, rather than CRLH TL of which formulas for the circuit elements are valid for very small θ with the same accuracy as $\sin\theta$ approaches unity. (In fact, the CRLH TL method can be considered as a sub-category of the general π and T models.) Possible radiation mechanism, including the radiation from the capacitor patches and the slots, of the proposed antenna has also been proposed. After the experimental comparison as shown in Figure 3.14, it is found that the antenna is more like a slot radiator. Instead of only half-space patch-like radiation, the proposed antenna structure with more than two radiating edges gives a fairly omni-directional radiation pattern. The proposed design has several advantages, such as easily achieving resonance, simple structure, compact size without performance degradation, and stable frequency against different ground size. Additionally, although the equivalent circuit parameters in this paper are chosen for certain considerations, different electrical length, different characteristic impedance, or different equivalent models are still possible to be applied.

3.2 One-Eighth Effective Wavelength Slot Antenna

Microstrip-fed slot antennas have been researched for long tomes therefore many circuit models have been revealed to explain the response of input impedance. The circuit models can be helpful in miniaturized slot antenna design. The circuit model extraction has also been discussed in [5]-[7], which using two-port network. In this study, the equivalent circuit model is also established. Based on the circuit analysis, the author proposes the method of using chip capacitors not only for size reduction but also the synthesizing resonance and impedance matching. The same circuit model is used to describe a conventional slot antenna with open end and miniaturized one for further understanding. As the example, first, a 1/8 effective wavelength slot antenna is developed for single band operation. Then, an extended design of frequency tunable type is presented.

The most commonly used approach to miniaturize a slot antenna is to route a dense path for keeping the required resonant length, that is, half wavelength for a short-to short slot or quarter wavelength for a short-to-open slot. As mentioned in Chapter 1, spiraled slots, a meandered slot or a slot ring with fractal geometry are in the same approaches that although the antenna area was shrunk, the required total electrical length along the slot was unchanged. All of these examples try to keep their half or quarter wavelength resonant mode in the operational frequency for the reduced antenna path. Unlike a conventional open-end slot antenna which requires quarter wavelength from open to short, the proposed capacitor-loaded slot antenna uses only one-eighth effective wavelength. Under operation frequency, the slot is inductive in stead of as a resonator, which is different from many miniaturized resonant antennas

3.2.1 Equivalent Circuit Analysis of Directly-Fed Open-End Slot

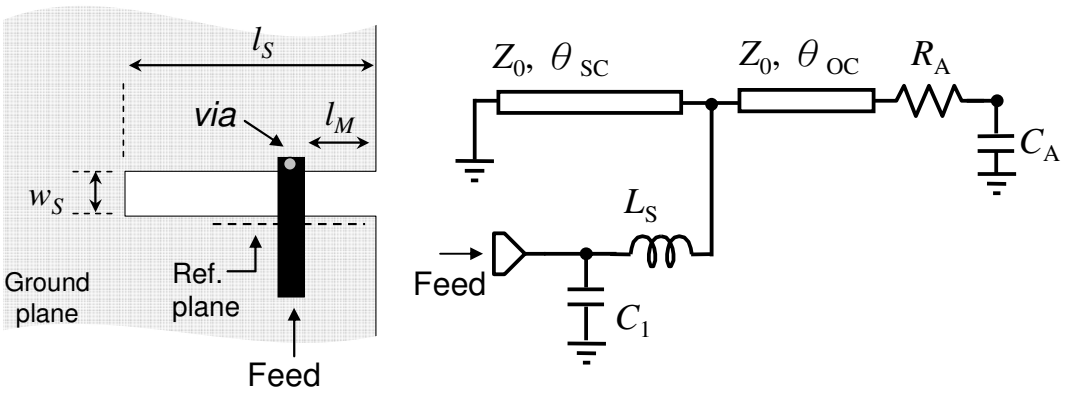

(a) (b)

Figure 3.16 (a)The configuration of an open-end slot antenna fed by a short-circuited microstrip line. (b)The corresponding equivalent circuit model.

Figure 3.16(a) depicts the geometry of an open-end slot antenna. In order to obtain the equivalent circuit model of the open-end slot, the structure of being fed by a short-circuited microstrip line is considered. A via is used for the microstrip to directly conduct the slot line on the ground plane. The slot line is with the length l_s = 9 mm and width w_s = 1.5 mm. The distance between the microstrip and ground edge is l_M which is the feeding position of the slot. The substrate is 0.4 mm FR4 and the width of the microstrip is 0.76 mm for 50 Ω. Figure 3.16(b) shows the equivalent circuit model corresponding to the configuration in Figure 3.16(a). Transmission line sections are used to model the slot line, of which θ_{OC} is related to l_M and θ_{SC} is the distance from the short end to the feeding position. R_A with C_A is for modeling the radiation resistor over the wide bandwidth. l_S and C_1 are the parasitic inductor and capacitor in the presence of the microstrip line crossing the slot. All the simulations are performed by the commercial EM tool, Ansoft HFSS. According to full wave simulation, the parameters can be extracted, characteristic impedance Z_0 = 140Ω, θ_{OC} +θ_{SC} = 39° as referred to 2.45GHz, R_A = 650 Ω, C_A = 0.12 pF, l_S = 0.5 nH, and C_1 = 0.04 pF. Figure 3.17(a) and (b) show the input impedances of the antenna, through reference plane, in Figure 3.16 from the full wave simulation and circuit model calculation respectively, with different feeding positions, l_M from 0 to 6 mm. The corresponding θ_{OC} in circuit calculation are 0°, 8.7°, 17°, 26° for l_m of 0, 2, 4, 6 mm.

Apparently, the results of circuit model calculation agree the results of full wave simulation through different feeding positions. Additionally, it can be seen that the slot resonates around 4.8GHz when l_M is small and possess inductance below 4.8GHz.

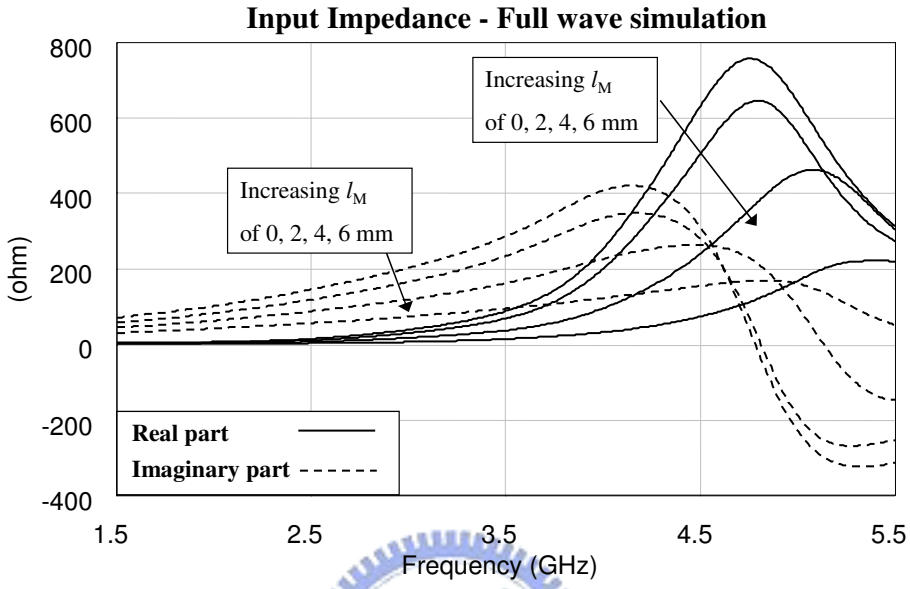

(a)

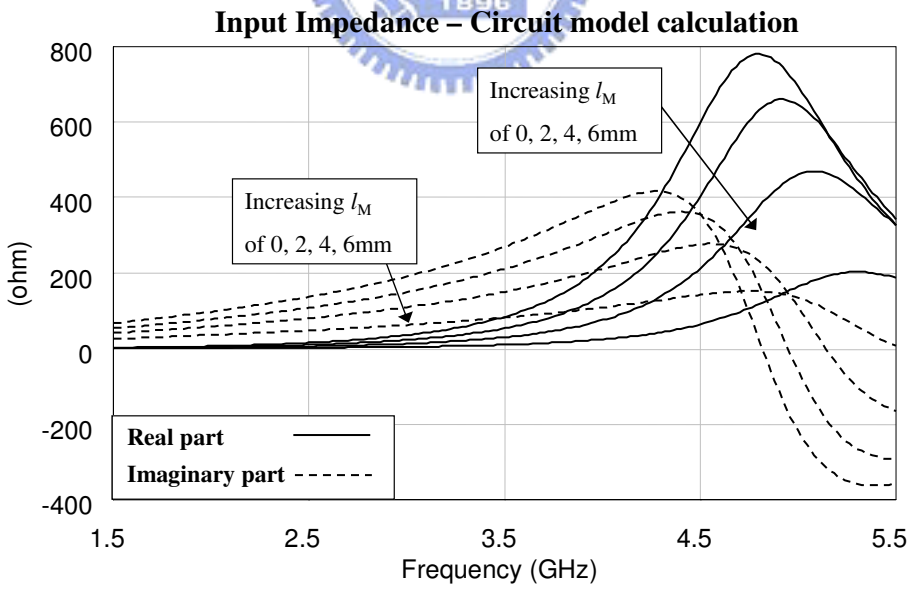

(b)

Figure 3.17 (a)The input impedance from full wave simulation with different l_M. (b)The input impedance from model calculation with different l_M.

3.2.2 One-Eighth Effective Wavelength Slot Antenna Design

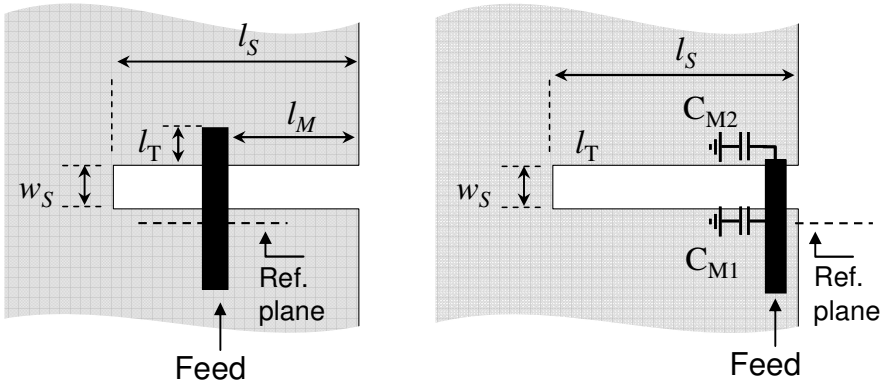

(a) (b)

Figure 3.18 (a)The configuration of a conventional microstrip-fed slot antenna with open end. (b)The configuration of the proposed slot antenna. Both the configurations have the identical slot size.

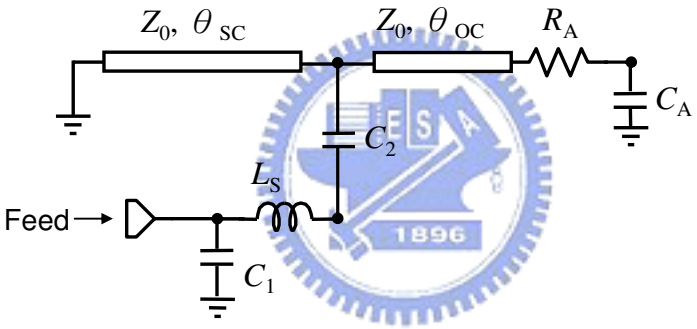

Figure 3.19 The corresponding equivalent circuit model of the antenna configuration in Figure 3.18.

Based on the equivalent circuit of the directly-fed open-end slot antenna, the conventional slot antenna with microstrip coupled structure was then studied. Figure 3.18(a) shows the conventional microstrip-fed slot antenna, where a 50Ω microstrip line is used to couple the input power to the open-end slot radiator. As well known, its operation frequency is mainly determined by the slot length l_S, which is quarter wavelength at the resonant frequency. The feeding position l_M and open stub length l_T can be designed to achieve critical coupling for input impedance matching. Also, Figure 3.18(b) shows the configuration of the proposed antenna, where two capacitors, C_{M1} and C_{M2}, are loaded to the 50Ω microstrip feeding line. With choosing the proper values, the antenna can operate below the resonant frequency of the slot. Both types utilize capacitive coupling for feeding the slot. Therefore, there will be a series capacitor between the feeding port and the slot for equivalent circuit. Considering

the shunt capacitor C_{M1} takes the same place of C_1 in equivalent circuit. C_{M2} and the open stub are same for the capacitive coupling, which is a series capacitor in equivalent. The conventional type and proposed type share the same equivalent circuit model, as shown in Figure 3.19.

In this study, the identical slot, l_s = 9 mm and w_s = 1.5 mm, for the conventional and proposed design were designed and fabricated on 0.4 mm FR4 substrate for comparison. The same ground plane size of 65 mm by 42 mm and 50 Ω microstrip line are used for both antennas with the slot radiator located in the middle of the long edge of the ground plane. The conventional type utilizes the natural resonance of the slot that possesses the resonant frequency determined by the slot length. l_M = 3.2 mm and l_T= 1.1 mm are designed for impedance matching. The proposed type is designed to operate in 2.45GHz, in purpose, by using two SMD capacitors loading on the feeding line. The capacitors C_{M1} and C_{M2} are properly designed as 2.4 pF and 0.6 pF by using HFSS simulation.

Figure 3.20 is the comparisons of the results of circuit model calculation and full-wave simulation for both conventional type and proposed antenna. Since the identical slot is used, the circuit model parameters of the slot are the same as that of the directly-fed slot, Z_0 = 140 Ω, R_A = 650 Ω, C_F = 0.12 pF, and $\theta_{SC} + \theta_{OC} = 39^o$. For the conventional type, equivalent θ_{OC} is 26^o for l_M = 5 mm, θ_{SC} is 13^o, and C_2 = 0.26 pF. For the proposed type, equivalent θ_{OC} is 3^o for l_M = 0.5mm, θ_{SC} is 39^o, C_2 = 0.63 pF, and C_1 = 2.35pF. The results of full wave simulation and equivalent circuit calculation match each other very well. This approves the accuracy the circuit model. It can be found that the conventional type possesses an anti resonance around 5GHz, which is the natural resonant frequency of the slot length. In the other hand, the purposed type has a resonance at 2.45GHz for the operational frequency, i.e. the slot antenna is miniaturized. The operation frequency is at 2.45GHz that is half of the conventional although identical slot size is used, as shown in Figure 3.21.

The conception of using the loading capacitors for impedance matching is quite intuitive. Since the open-end slot antenna is short as compared to the wavelength at 2.45 GHz, it behaves as an inductive component as seen from the feeding microstrip line. Therefore, by the proper design of C_1 and C_2, it is possible to match the short slot to 50 Ω. Once the circuit parameters related to the microstrip-fed slot are obtained,

C_1 and C_2 can be easily found.

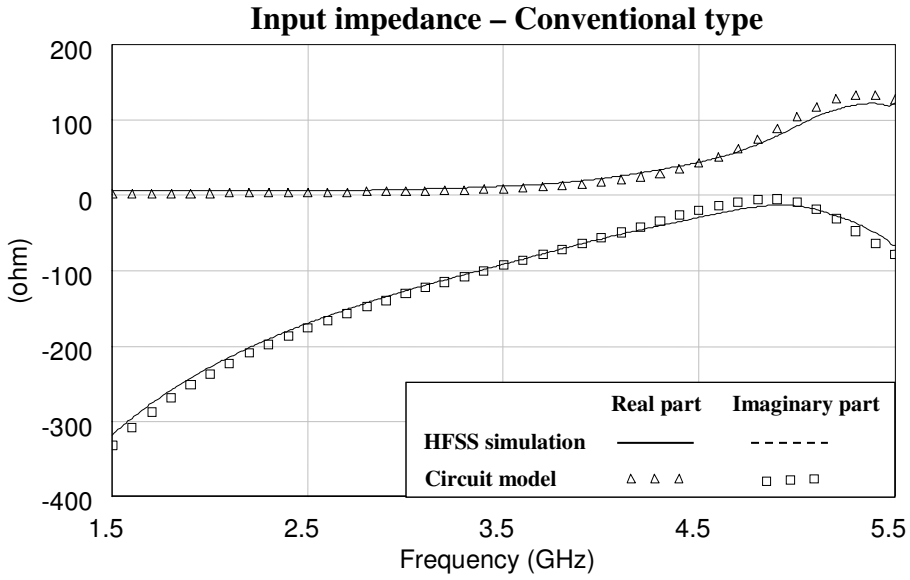

(a)

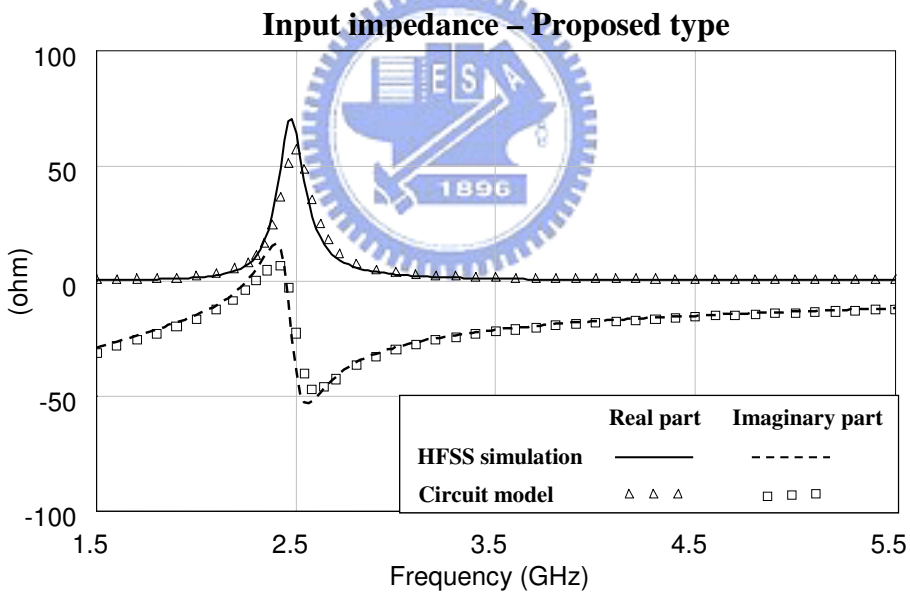

(b)

Figure 3.20 The comparison of input impedance between circuit model calculation and full-wave simulation. (a)The conventional open-end slot antenna. (b)The proposed open-end slot antenna.

3.2.3 Experimental Results of One-Eighth Effective Wavelength Slot Antenna

For experiment, the antennas were fabricated and measured. The Murata SMD capacitors of 0.6 pF and 2.2 pF with part number GRM1555C1HR60CZ01 and GRM1555C1H2R2CZ01 are used in the proposed antenna for C_{M2} and C_{M1}. A 50Ω cable is connected to the microstrip line for measurement. Figure 3.21 shows the simulated and measured return losses of the conventional and proposed open-end slot antennas. The measured 10-dB bandwidth of the proposed type is from 2.4 to 2.509 GHz that is sufficient for 802.11b/g application. The conventional type possesses quarter wavelength resonance operates around 4.8GHz twice than the proposed type. Therefore, the proposed type can be treated as roughly one-eighth effective wavelength open-end slot antenna. Figure 3.22 shows the radiation patterns of the proposed one-eighth effective wavelength slot antenna at 2.45GHz. The measured peak gain is 1.89dBi on *yz*-plane. The averaged gains are -3.8dBi, -1.1dBi and -1.2dBi on *xy*-, *xz*-, *yz*-plane respectively. It means the radiation efficiency is fairly good although the slot does not resonate at the operation frequency. In addition, since the resonance of the antenna is determined by the circuit synthesis, which is an inductive slot and two capacitors, the resonant frequency should be stable against ground size, as mentioned in Chapter 3.1.3. Figure 3.23 shows the measured return losses a set of antennas with the identical slot and capacitors but with different ground sizes was fabricated and measured. The resonant frequencies are the same against different ground sizes, as prediction.

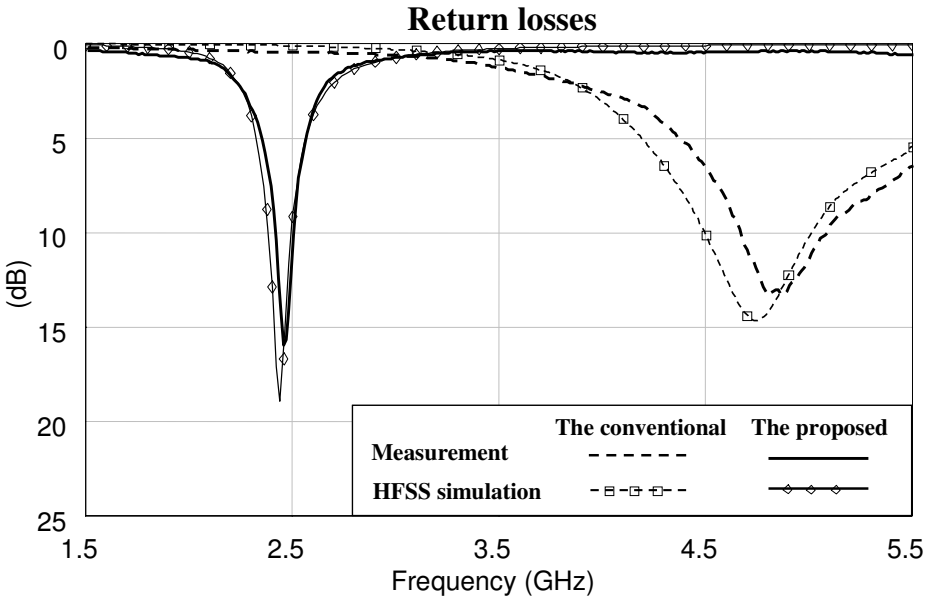

Figure 3.21 The simulated and measured return losses of the proposed antenna.

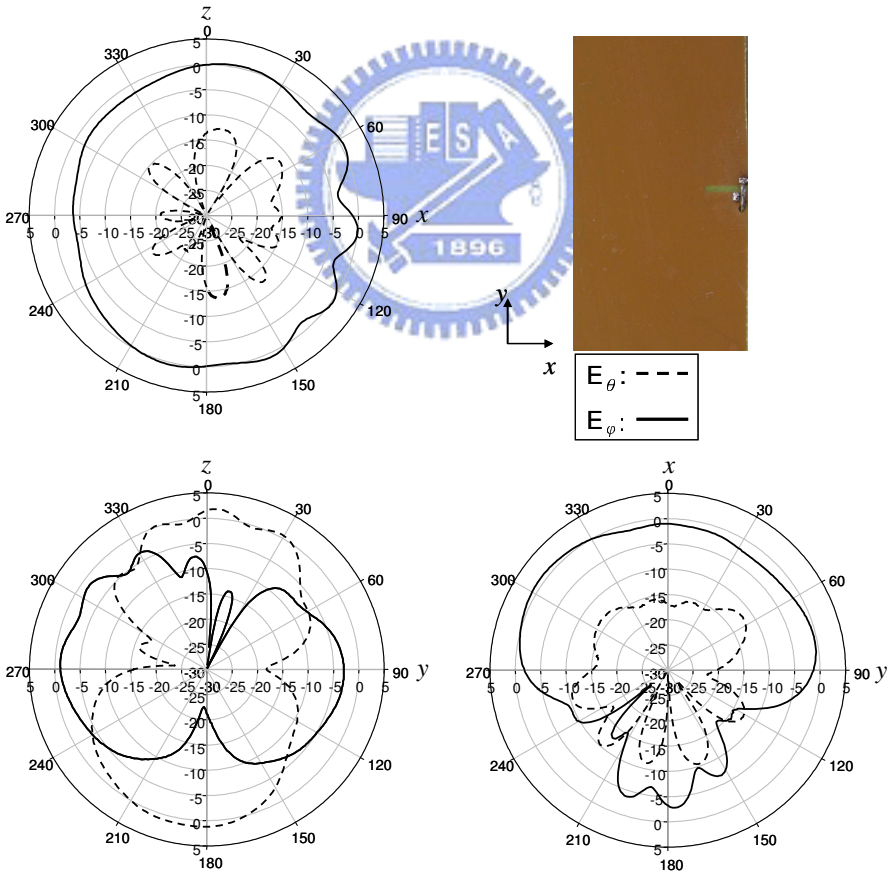

Figure 3.22 The measured radiation patterns of the proposed antenna.

Type A
(20 mm X 50 cm)
USB dongle size

Type B
(40 mm X 70 cm)

Type C
(170 mm X 250 mm)
Laptop panel size

(a)

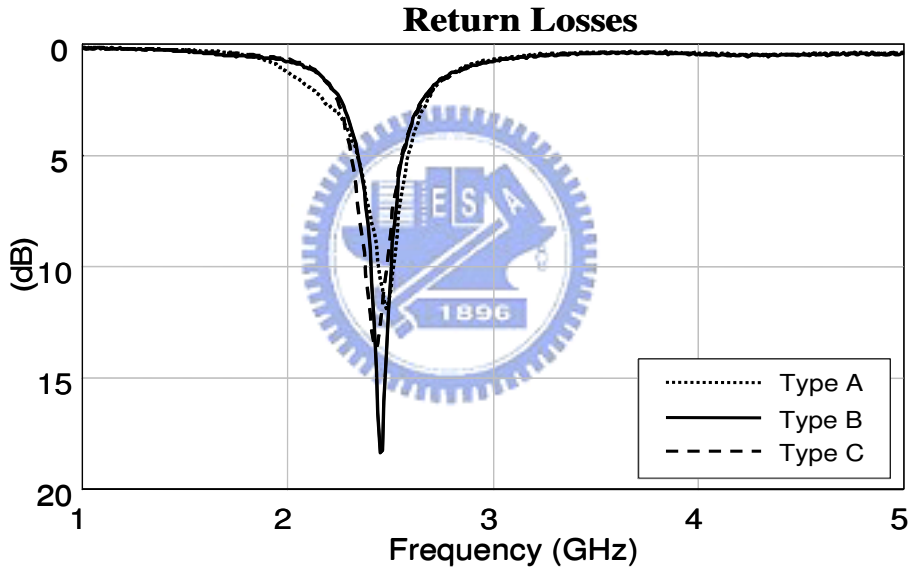

(b)

Figure 3.23 (a)One-eighth wavelength antennas with identical slot and capacitors with different ground sizes. (b)The return losses of one-eighth wavelength antennas with identical slot and capacitors with different ground sizes.

3.2.4 Summary

The input impedance of directly-fed open-end slot antennas has been explained by a equivalent circuit model. The results of circuit model calculation quite agree the result of full wave simulation over a wide bandwidth. Based on the slot model, the circuit model of conventional quarter wavelength open-end slot antenna was also developed. Also, using the same circuit model, we proposed a one-eighth wavelength slot antenna. The proposed antenna utilizes a short open-end slot, roughly one-eighth effective wavelength in 2.45GHz, with two chip capacitors. The values of chip capacitors can be designed through the circuit model. In operational frequency where the antenna is matched, the slot possesses inductive impedance that does not resonate.

The comparison between the conventional and the proposed slot antennas using identical slot size was given. The results of the circuit model calculation, full-wave simulation and measurement show agreements. In this study, the proposed antenna designed to operate at 2.45GHz has measured 10dB return loss of 109MHz. The antenna size is only 9 mm by 1.5 mm. Measured radiation pattern is omni-directional with peak gain of 1.89 dBi that means the efficiency is still fairly good even the slot line does not resonate.

3.3 Frequency Tunable Slot Antenna

The need of wideband broadcast reception or multiple communication systems integrated in the same device requires the antenna that can cover all the operation bandwidth. The design of an efficient compact antenna covering wide bandwidth is major challenge. The concept of frequency tunable antenna is proposed as one of the solutions. The frequency tunable antenna is tuned to provide narrower required bandwidth instantaneously over all the bandwidth instead of covering all the bandwidth simultaneously. The advantage is to gain the increased bandwidth without increasing size but requires additional active elements for tuning.

3.3.1 Frequency Tuning Mechanism

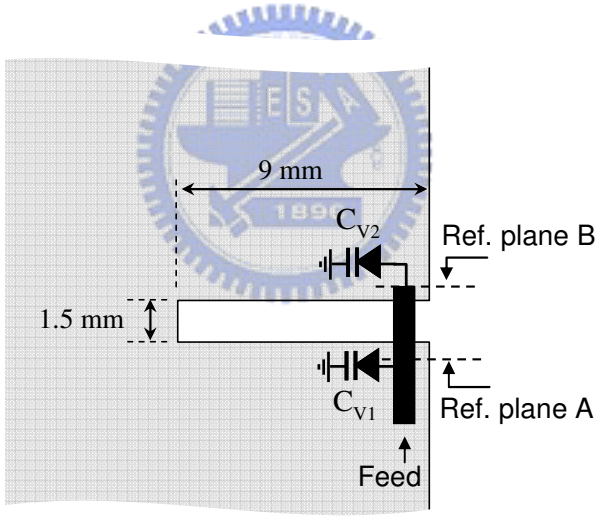

Figure 3.24 The geometry of the proposed frequency tunable antenna

The configuration of the tunable type is shown in Figure 3.24. There are two varactors loaded at the open-end of the microstrip line, C_{M2}, and shunt with the feed point, C_{M1}, respectively. In this study, the size of the slot keeps l = 9 mm and w = 1.5 mm. By tuning the varactors, the antenna can operate over wide bandwidth. To demonstrate the tuning mechanism, the first is to consider the equivalent circuit as shown in Figure 3.25(a) which is arranged from the circuit model of the identical slot ,as shown in Figure 3.19 with varactors instead of capacitors. Since the

arrangement is only changing the sequence of series elements the impedance feature will not be affected. The normalized equivalent impedance *r(f) + jx(f)* is from the slot radiator treated as a two-port network with reference plane at A and B in Figure 3.24. In this study, the 2-port network of the slot radiator is obtained from HFSS simulation. The ports are located at the reference plane A and B in Figure 3.24. To tuning the antenna a simplified model, as shown in Figure 3.25(b), can be considered. C_{V1} and C_{V2} dominate the value of C_1 and C_2 in the circuit model for the reason of loading C_{V1} and C_{V2} with larger value than parasitic of the microstrip. It is noticed that the model turns into the circuit with matching network of series capacitor and shunt capacitor. Antenna can be matched as long as *r(f) + jx(f)* located outside the forbidden area, as shown in Figure 3.26. The forbidden area is based on 10dB return loss matching. The required value of C_{V1} and C_{V2} can also be estimated easily. It can be found that the slot radiator can be matched over most frequency range when it possesses inductive impedance.

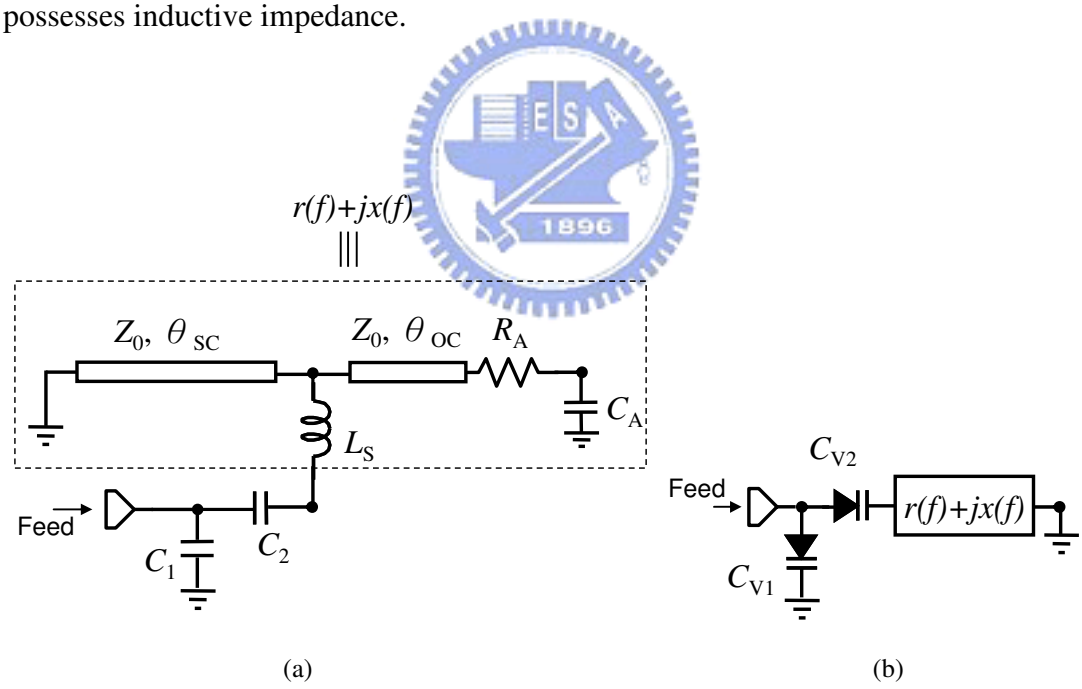

Figure 3.25 (a)The equivalent circuit model of the proposed antenna. (b)The simplified model after the arrangement from Fig. 2(a).

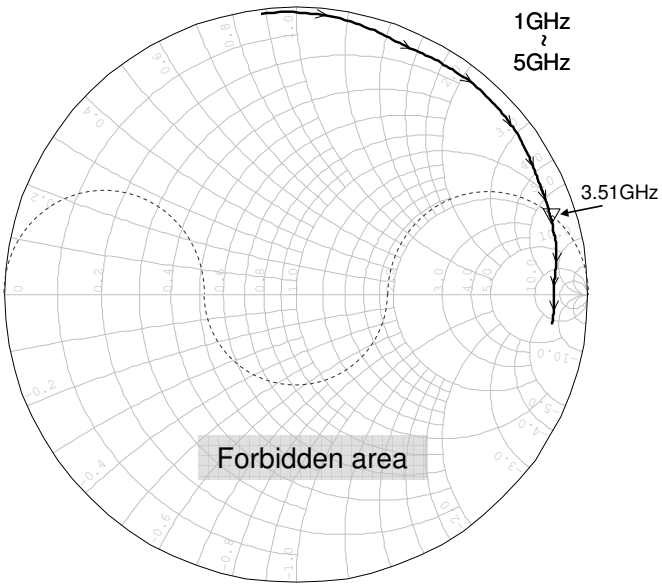

Figure 3.26 The impedance curve, *r(f)+jx(f)*, of the slot line on smith chart from the full-wave simulation. The denoted region is the forbidden area for the proposed matching scheme.

3.3.2 Experimental Results of Frequency Tunable Slot Antenna

For experiment, the antennas were fabricated on the FR4 substrate with thickness of 0.4 mm. The ground plane is 70 mm by 40 mm and slot is 9 mm by 1.5 mm. The open-end slot located 30 mm away from the upper edge. Because the tuning limited tuning range and parasitic resistor of varactors, the antenna using SMD capacitors without the bias circuit is measured first to verify the proposed tuning mechanism. Figure 3.27 shows the return losses of the antenna with different SMD capacitors. The results indicate that with the different values of C_{V1} and C_{V2}, the antenna can operate at least from 1.57GHz to 3.7GHz with good input matching. The wide tuning range of the proposed configuration was performed that proves the proposed tuning mechanism. However, it requires a large varying range of capacitance. It is difficult to find the varactor that can cover all of these values. The tuning range of the varactors would be the limitation of the tunable antenna. The return losses of antennas using SMD capacitor also show that the antenna can be easily matched to the operational frequency as long as the slot possesses inductive impedance.

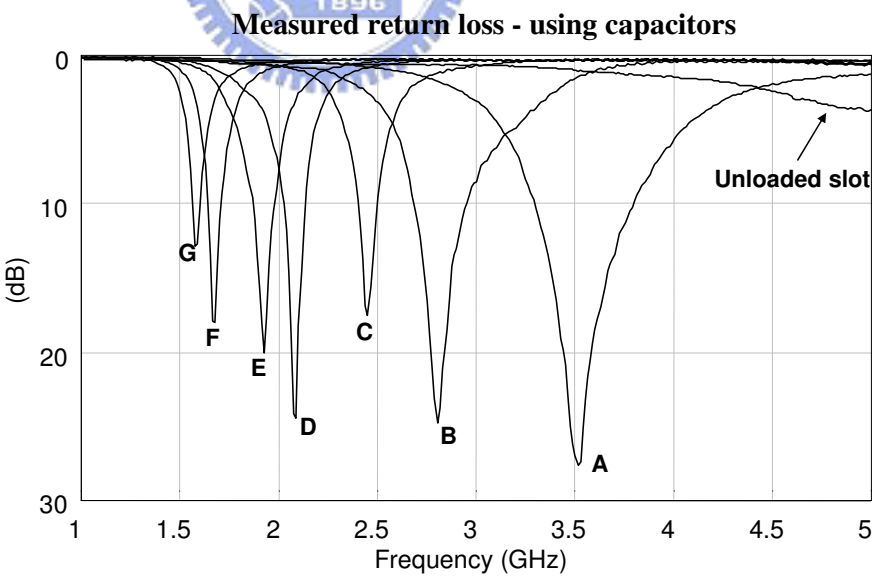

	A	B	C	D	E	F	G
C_{V2} (pF)	0.2	0.4	0.6	1.0	1.2	1.5	1.8
C_{V1} (pF)	0.4	1.0	2.2	2.5	2.7	3.9	4.7

Figure 3.27 The measured return losses of the antenna with SMD capacitors.

3.5GHz

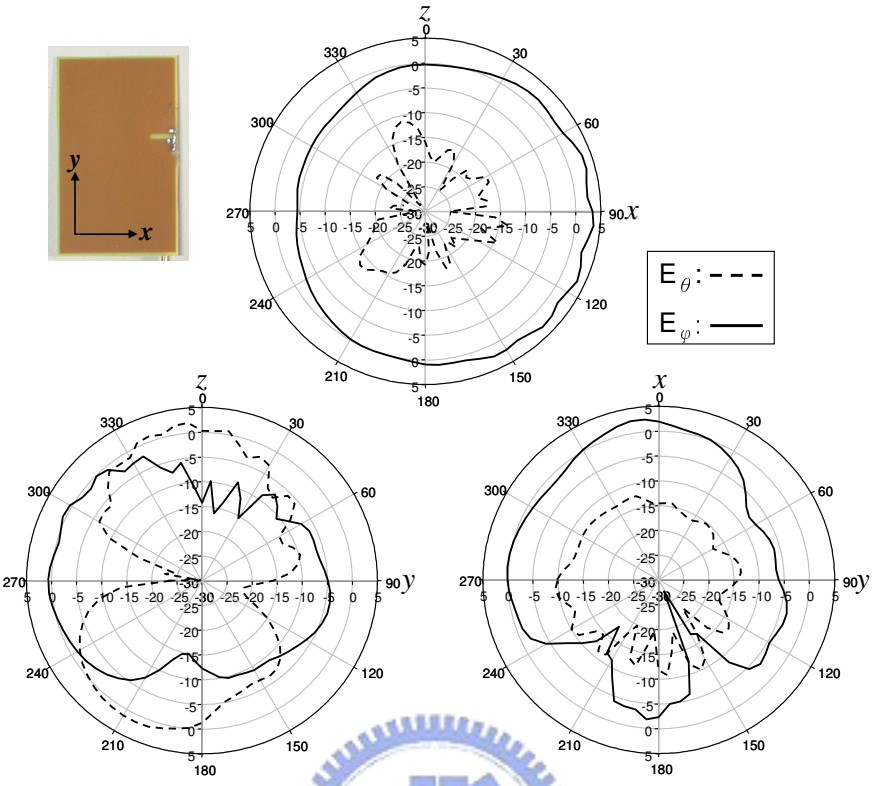

(a)

2.45GHz

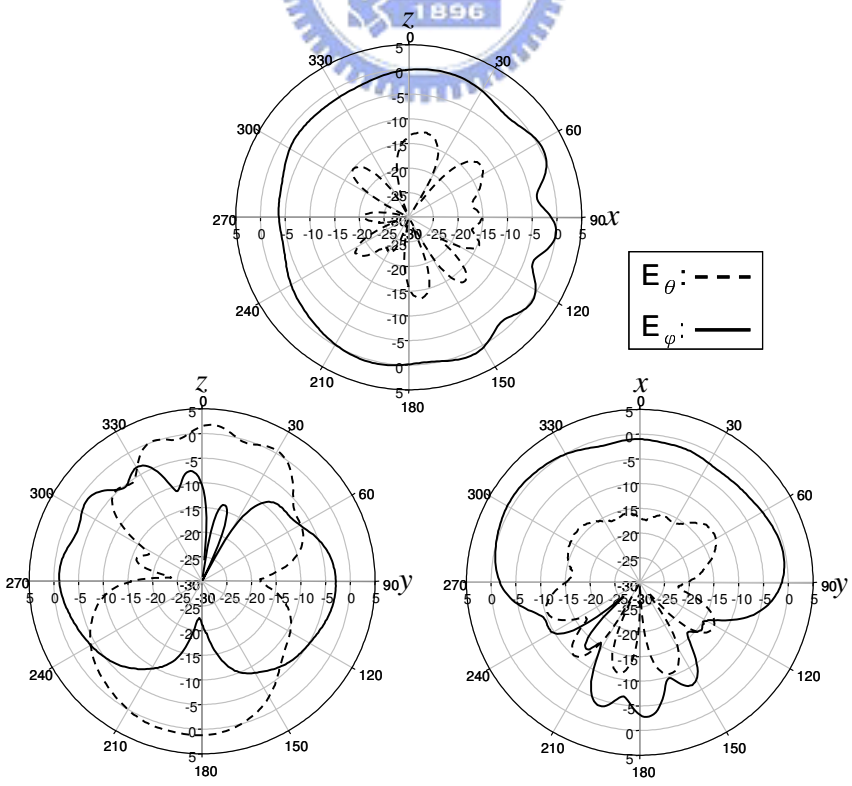

(b)

1.9GHz

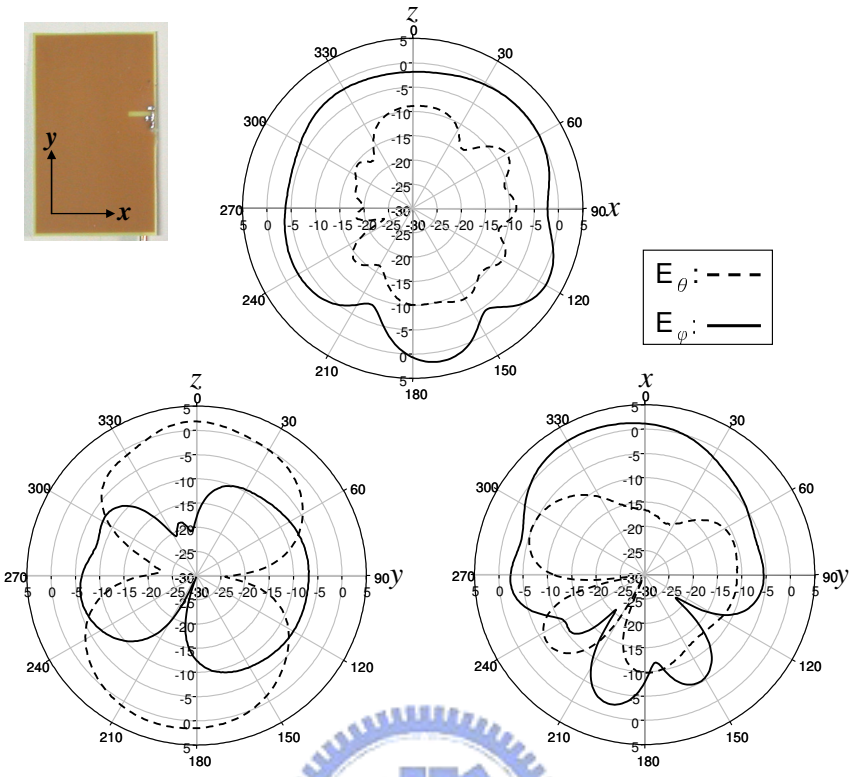

(c)

1.64GHz

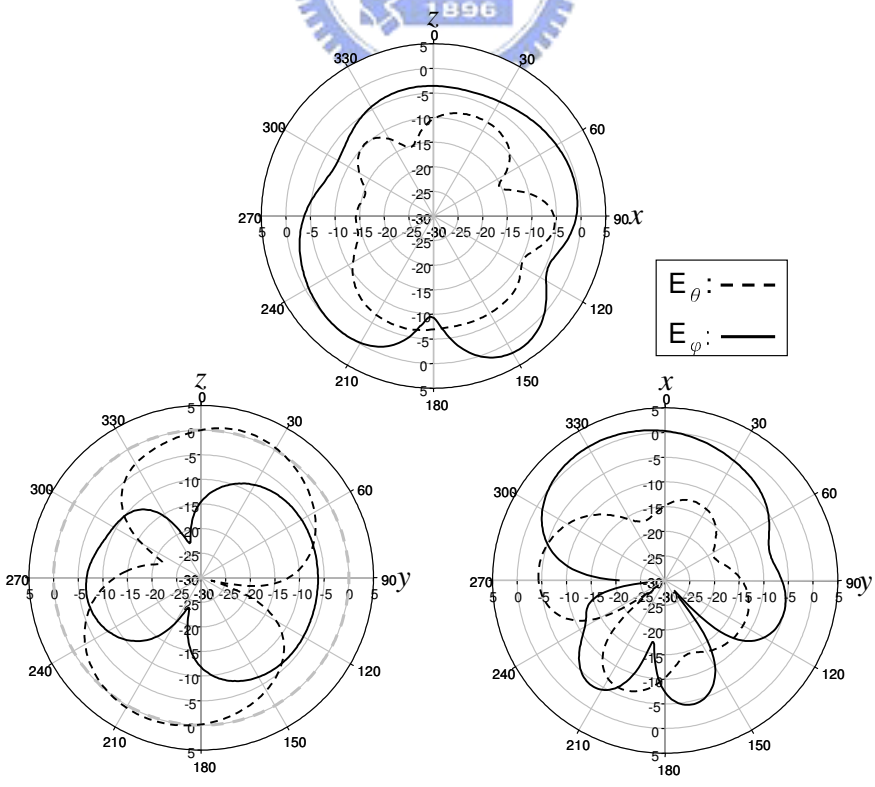

(d)

Figure 3.28 Measured patterns The measured radiation patterns of different operational frequencies (a)The antenna with C_1 = 0.2 pF and C_2 = 0.4 pF for 3.5GHz.. (b)The antenna with C_1 = 0.6 pF and C_2 = 2.2 pF for 2.45GHz. (c)The antenna with C_1 = 1.2 pF and C_2 = 2.7 pF for 1.9GHz. (d)The antenna with C_1 = 1.5 pF and C_2 = 3.9 pF for 1.64GHz

Frequency	Peak gain	Radiation efficiency
3.5GHz	3.7 dBi	78%
2.45GHz	1.89 dBi	69%
1.9GHz	2.69 dBi	50%
1.64GHz	1.68 dBi	45%

Table 3-2 The gain and efficiency of antennas using SMD capacitors

The efficiency of small antennas is always the concern. A set of antennas using SMD capacitors was measured for the radiation patterns and radiation efficiency. Figure 3.28 plots the measured radiation patterns of four antennas with different capacitors for different operational frequency. The chosen frequencies are 1.64GHz, 1.9GHz, 2.45GHz, and 3.65GHz. Over these frequencies, the measured patterns are quite similar and are like omni-directional. The measured peak gains and radiation efficiencies are listed in Table 3-2. Fairly good gains and efficiency were measured. Peak gains are all more than 0dBi in each frequency and the efficiency is still acceptable at 1.64GHz of which the slot length is less than 1/10 effective wavelength.

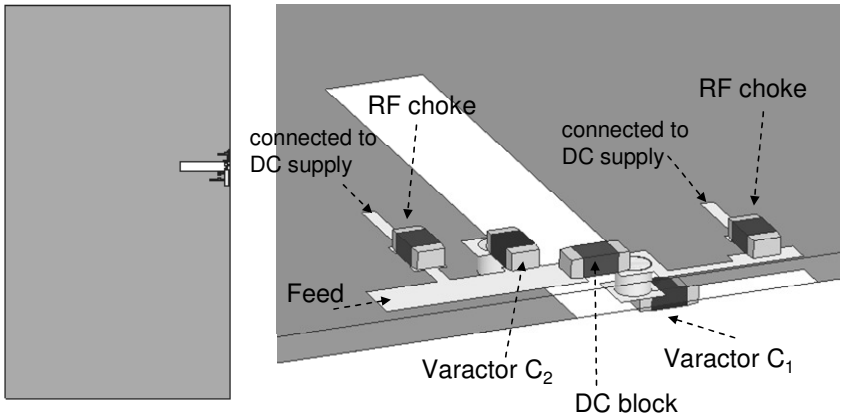

(a) (b)

Figure 3.29 The illustration of the frequency tunable antenna layout (a)Whole view (b)Circuit arrangement.

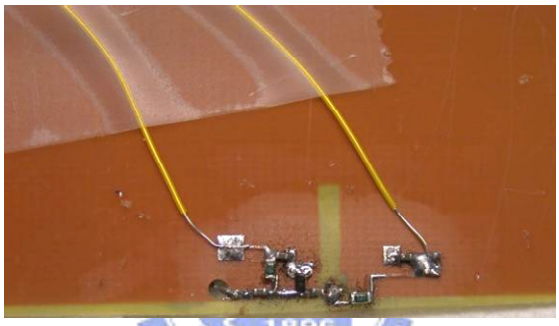

Figure 3.30 The photograph of the realized frequency tunable antenna.

After the tuning mechanism was verified, the antenna using varactors was designed and fabricated for experiment. The identical slot, 9 mm by 1.5 mm, located on same ground size is used, as illustrated in Figure 3.29(a). The layout with bias circuits of the realized antenna is shown in Figure 3.29(b). Considering wide tuning frequency range, the RF chokes employ resistors of 7K ohm. The varactor C_1 and C_2 are both implemented by using Alpha SMV1232 varactor with tuning range from 0.72 pF to 4.15 pF. The photograph of realized antenna is shown in Figure 3.30. Since the tuning range of the varactor is limited the predicted tunable frequency range would be less than 2.5GHz according to the results of using capacitors. Figure 3.31 shows the measured return losses of the antenna with SMV1232 varactors. The capacitance response against applied voltage is listed in Figure 3.32. The measured results agree the prediction that the proposed antenna is limited with tuning range from 1.36 to 2.45 GHz for varactor SMV1232. The radiation patterns for three operational frequencies

of 2.45GHz, 1.95GHz, and 1.65GHz, are measured, as shown in Figure 3.33. The applied voltages for these frequencies are list in Figure 3.31. Only gains on *yz*-plane are plotted. Over these three frequency bands, the patterns are similar but the gains tend smaller in lower frequency. The low gains are caused by the parasitic resistor of the varactors and the smaller radiation resistor in low frequency that makes matching circuit inefficient. The comparison of radiation efficiency for antennas using capacitors and varactors is shown in Figure 3.34. The efficiency is measured by using SATIMO 3D near-field antenna measurement system. The measured frequency ranges are different but overlapped. It can be seen that the efficiency of both types decreases when frequency decreases. However, the efficiency of antennas using capacitors is much better than those using varactor. For 2.45GHz, the efficiency of using capacitors is 69% that is 17% higher that using varactors. This is because the parasitic resistor of varactor is much larger than that of capacitor. To have better efficiency for frequency tunable design, varactors with lower resistance should be used.

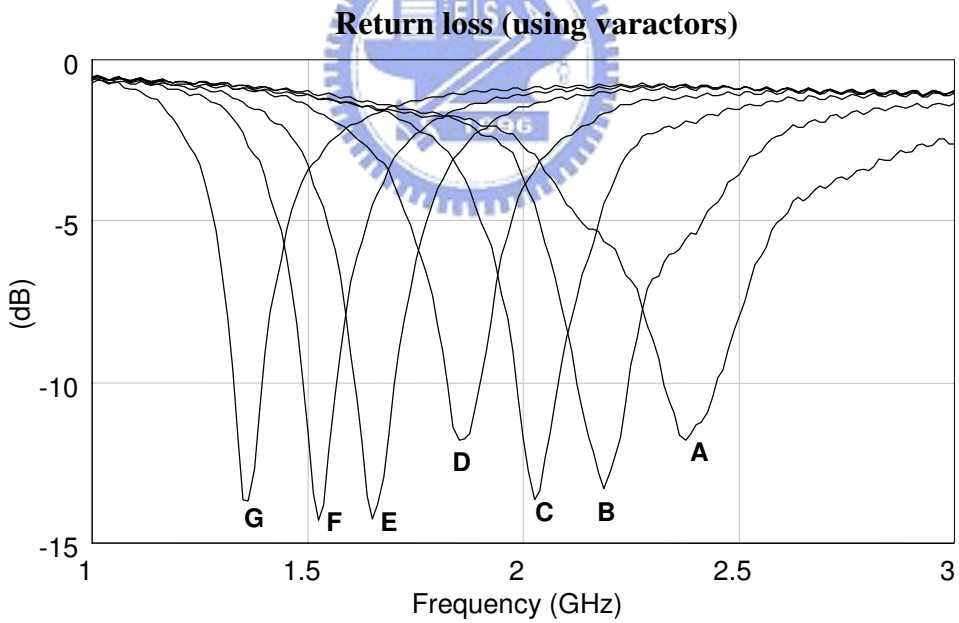

	A	B	C	D	E	F	G
V_1 (V)	10	7.5	5.5	4.0	2.8	2.0	1.1
V_2 (V)	8.4	3.6	2.4	1.7	0.9	0.4	0.0

Figure 3.31 The measured return losses of frequency tunable antennas using varactors with different applied voltages for different operational frequency.

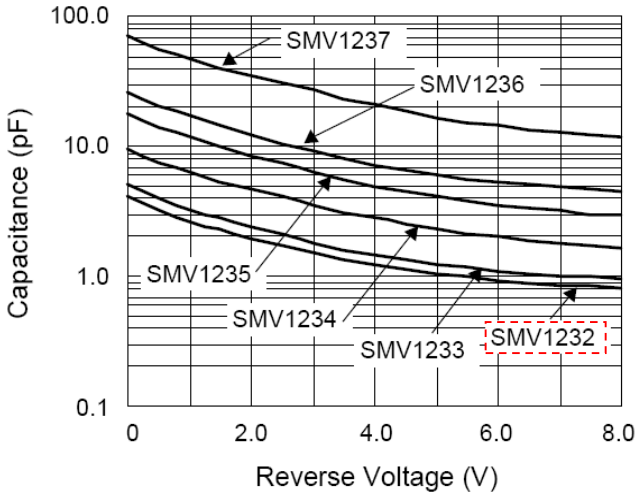

Figure 3.32 The capacitance tuning range of ALPHA SMV1232 varactor.

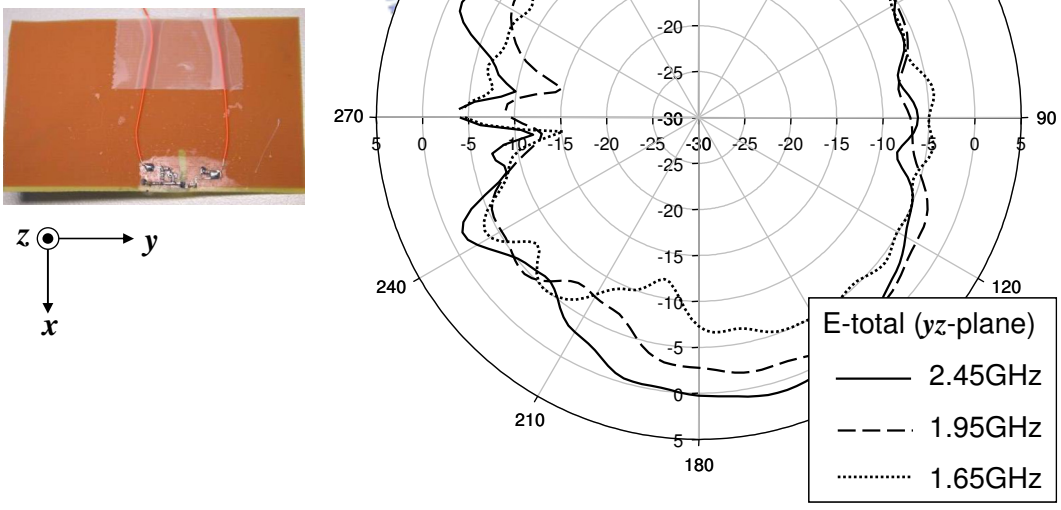

Figure 3.33 Measured radiation pattern of frequency tunable antenna on *yz*-plane in 1.65GHz, 1.95GHz, and 2.45Ghz (E-total).

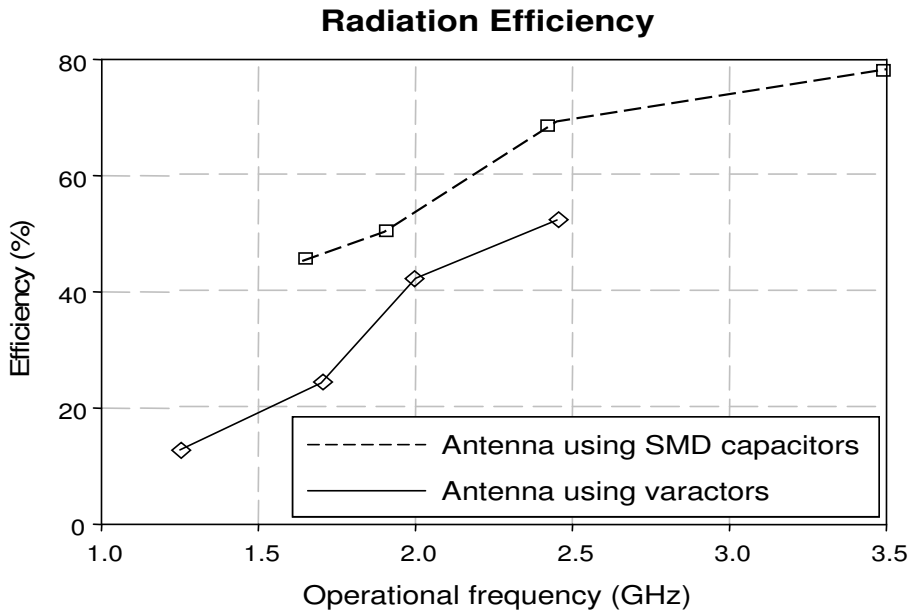

Figure 3.34 The comparison of radiation efficiency for using capacitors and varactors.

3.3.3 Summary

A compact frequency tunable antenna has been presented. The proposed antenna is the extended design of one-eighth wavelength slot antenna. It consists of an open-end slot radiator and two varactors for tuning. The tuning mechanism is based on the equivalent two-port network of the slot radiator. The frequency range able to be tuned can be determined from the full-wave simulation of the slot radiator only. The tunable mechanism is equivalent to a series-C and shunt-C matching scheme. When the antenna is matched, the slot radiator possesses inductive impedance. Therefore, the slot length will be short as compared with the wavelength of the operation frequency. The tuning range is dominant by the tuning range of the varactors. The proposed structure is simple and compact with wide tuning range which has high potential for mobile application.

Chapter 4 Isolation Enhancement Methods of Ground Edge Current Choke

4.1 GECC Configuration

The radio frequency (RF) choke is one of the important components in microwave circuits. Its function is usually known as to block the RF signal, and the general application is for supplying DC bias and preventing RF signal from leaking to the bias circuit [56]. The RF choke is usually implemented by distributed elements, such as a quarter-wavelength transmission line with short-circuited terminal, which possesses very high input impedance as an open circuit so as to stop the RF current. The function of blocking the RF signal can also be achieved by other structures, such as the defected ground (DGS) structures [57]-[58] and electromagnetic band gap (EBG) structures [59]. A DGS structure performs like a low pass filter that can stop the high frequency signal and an EBG structure is like a notch filter that stops the specified frequency band.

The RF choke structures are also used in the antenna design for improving the antenna performance, such as bandwidth enhancement, multiple band operation, gain enhancement, and the radiation pattern shaping. There are already many publications discussing the use of RF chokes, DGS and EBG structures for improving antenna performance. The sleeve Balun for dipole antenna feed is a best example of using the short-circuited quarter-wavelength coaxial cable as an RF choke [60]. Similar designs were also performed in horn antennas, where the coaxial cable choke was used to prevent the current from distributing over the outer conductor of the horn [61]-[63]. These chokes mounted on the horns can improve the radiation patterns [61]-[62] or enhance the antenna gain [63]. Besides, to reduce the surface wave for a good radiation pattern, the uses of ring chokes and EBG structures have been presented in [64]-[65]. The concept of RF choke was also adopted to achieve multiband or wideband operation. In [66], a choke, formed by a short-circuited quarter-wavelength microstrip stub, was introduced to divide a monopole antenna into

two sections so as to create two resonant paths and thus achieve dual band operation. In [67], a bandwidth enhancement technique for mobile phone antennas was developed by introducing a quarter-wavelength choke to the chassis edge. By properly designing the position of the choke, the bandwidth can be obviously improved.

A new miniaturized RF current choke is proposed and demonstrated. Unlike utilizing a short-circuited quarter-wavelength transmission line, the proposed choke is implemented using a printed inductor and a capacitor, which is easy to be fabricated on the circuit board. And the size is as small as only 6% of the free space wavelength. As one knows, the induced ground plane current of a printed antenna (especially a small antenna) contributes to a large part of the antenna's radiation field. Also, most of the current concentrates along the edges of the ground plane. Therefore, the distribution of the ground edge current may affect the antenna's performance much. The proposed RF choke is to be located on the peripheral of the ground plane for blocking and thus shaping the ground edge current.

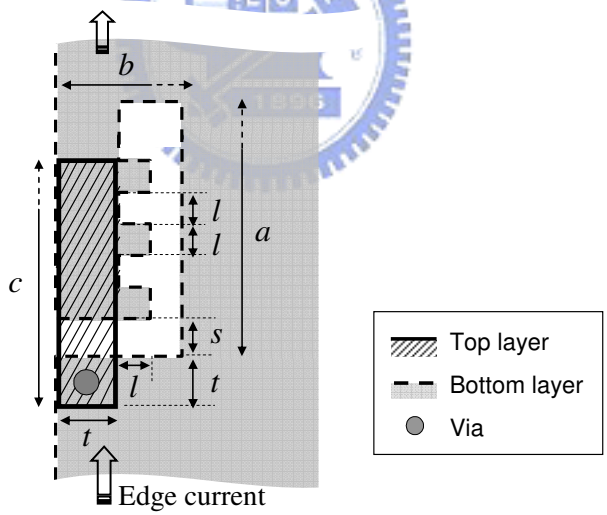

Figure 4.1 Configuration of the proposed ground edge current choke.

4.2 GECC Design and Measurement

In order to block the current traveling along ground edge, the RF choke is designed to perform an effective electrical open circuit on ground edge. Figure 4.1 illustrates the geometry of the proposed ground edge current choke (GECC), which is

implemented using a printed inductor and a capacitor. The inductor is realized by a corrugated L-shape slit at the ground plane edge on the bottom layer of the substrate, and the capacitor is by a metal strip on the top layer and the ground plane underneath. As shown, a via is used to connect the strip and the ground plane. When a current flows upwards along the ground edge toward the structure, part of it goes along the meandered edge of the corrugated slit, thus experiencing an effective inductance; the rest climbs up to the metal strip through the via and is then capacitively coupled to the underneath ground plane. After that, both current streams merge and flow upwards together. Therefore, the proposed configuration forms an equivalent parallel LC resonator and thus exhibits an open circuit at the resonant frequency. The value of the capacitor depends on the overlapping area of the metal strip and the ground plane. And the length of the current path along the slit edge determines the value of inductance.

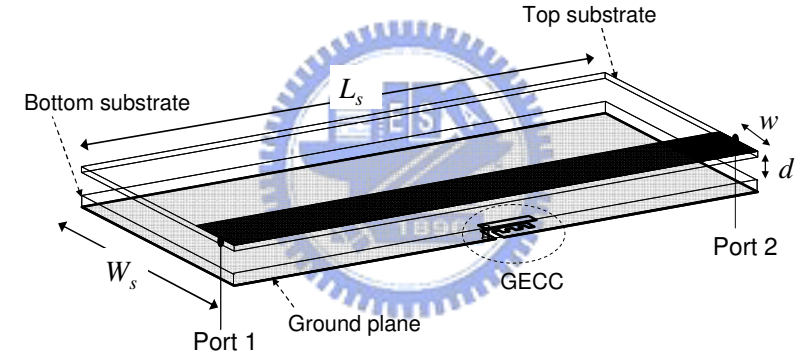

(a)

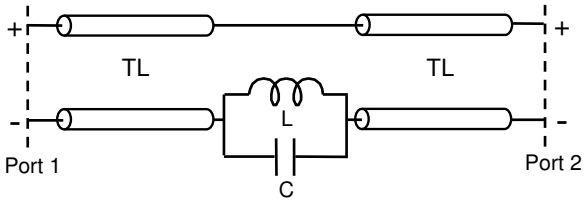

(b)

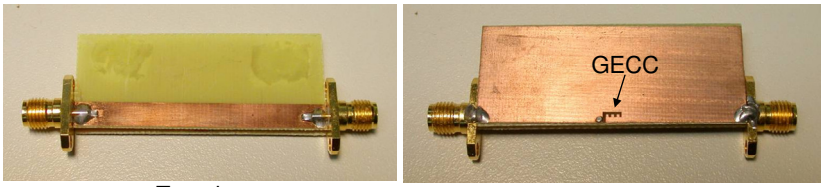

(c)

Figure 4.2 (a)The transmission line structure for measuring the proposed RF choke. L_s = 50 mm, W_s = 20 mm, w = 5 mm, and d = 1.6 mm. (b)Equivalent circuit of measurement structure. (c)The photograph of measurement transmission line structure.

To evaluate the proposed GECC and to study the design parameters, various sets of simulations and measurements were performed. To this end, a microstrip line structure containing the proposed GECC as shown in Figure 4.2(a) is proposed for test. There are two FR4 substrates used for the signal line and ground plane, respectively, to form the transmission line. The signal line is printed along the edge on the upper layer of the top substrate (with thickness of 0.4 mm). And the ground plane of the microstrip line is printed on the bottom layer of the bottom substrate (0.8 mm thickness). The GECC for testing is fabricated on the ground plane and is inserted in the middle of the ground edge just under the signal line. The equivalent circuit for this test setup is illustrated in Figure 4.2(b). The current will be blocked and not go through the transmission line at the resonant frequency of the choke. By measuring the transmission coefficient (S_{21}) of the transmission line, the property of the GECC can be observed. In order to keep impedance matching, the characteristic impedance of the choke-embedded transmission line is designed as 50 Ω. From simulation, the required width of the signal line is 5 mm and the gap between two substrates is 1.6 mm. Figure 4.2(c) shows the photograph of the proposed structure for measurement. Two SMA connectors are used to connect the transmission line.

The operating frequency of the GECC is designed around 5 GHz. Figure 4.3 shows the frequency responses of the simulated and measured transmission coefficients (S_{21}), for various values of the GECC dimensions a, b, c. Other structure parameters are fixed as t = 1 mm, l = 0.5 mm, and s = 0.6 mm. Three corrugation teeth as shown in Figure 4.1 are used in the L-shape slit of the GECC to provide sufficient inductance. The simulations were performed by commercial tool, Ansoft HFSS. Figure 4.3(a) shows the effect of the choke length a (= 3.5, 4.0, 4.5 mm), with choke width b and strip length c fixed at 2 mm and 3.9 mm, respectively. The measurement results agree well with the simulation. It is observed that for each length a, the frequency response exhibits a notch, with a minimum transmission coefficient of about -14 dB. The fractional 10-dB insertion-loss ($1/S_{21}$) bandwidth is about 6%. It demonstrates that the signal can be blocked by the use of the proposed GECC. The measurement notch frequencies are 5.25 GHz, 4.95GHz, and 4.75 GHz when the length is chosen as 3.5 mm, 4.0 mm, and 4.5 mm, respectively. The longer

the length *a*, the lower the notch frequency is. This is obvious since a larger *a* corresponds to a longer slit and thus a longer inductive path. The increase of the GECC inductance reduces the resonant frequency of the parallel LC resonator and thus the notch frequency. Similar phenomenon can be observed when the choke width *b* is increased. Figure 4.3(b) shows the results for various choke width *b* (=2.0, 2.5, 3.0 mm), with choke lenth *a* and strip length *c* fixed at 3.5 mm and 3.9 mm, respectively. The resonant frequency reduces from 5.25 GHz to 4.375 GHz as *b* increased from 2 mm to 3 mm. A total frequency shift of 875 MHz is achieved for 1 mm increase of *b*, which is larger than that (500 MHz) for the increase of *a* in the same amount.

Figure 4.3(c) shows the frequency responses of the transmission coefficient for various strip length *c* (= 3.4, 3.9, 4.4 mm), with *a* = 3.5 mm and *b* = 2 mm. The resonant frequency varies from 5.7 GHz to 4.8 GHz with *c* increased from 3.4 mm to 4.4 mm. The strip length determines the overlapping area of the metal strip and the ground, and thus affects the value of the equivalent capacitance. With the same slit size, the longer strip can has lower resonant frequency because of larger capacitance. In practice, the capacitor of the proposed GECC can be implemented in an alternative way, i.e., by using a lumped capacitor instead of a printed one. The lumped capacitor has the advantage of larger capacitance in a small size, which can be considered when further miniaturization is required.

It is seen from the above tests that, the proposed GECC structure can effectively block the ground current flowing along the edge. Its behavior is just like that of an equivalent parallel LC circuit. Although not shown here, the effects of other structure parameters have also been checked. It is found that by tuning the parameters of the corrugated slit, the equivalent inductance can be varied. And by increasing the metal strip dimensions, the equivalent capacitance can be raised. The notch frequency of the GECC can thus be controlled and designed. Note that the proposed GECC is compact as compared to others in the open literature, and has a size as small as about 0.06 wavelength in free space.

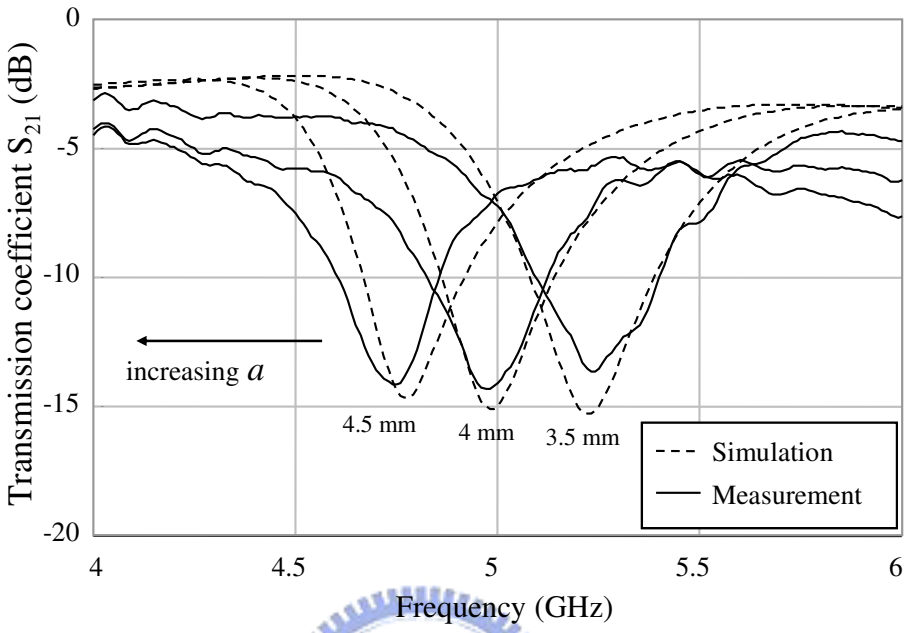
0
-5
-10
-15
-20
4
4.5
5
5.5
6
Transmission coefficient S_{21} (dB)
Frequency (GHz)
increasing a
4.5 mm
4 mm
3.5 mm
Simulation
Measurement

(a)

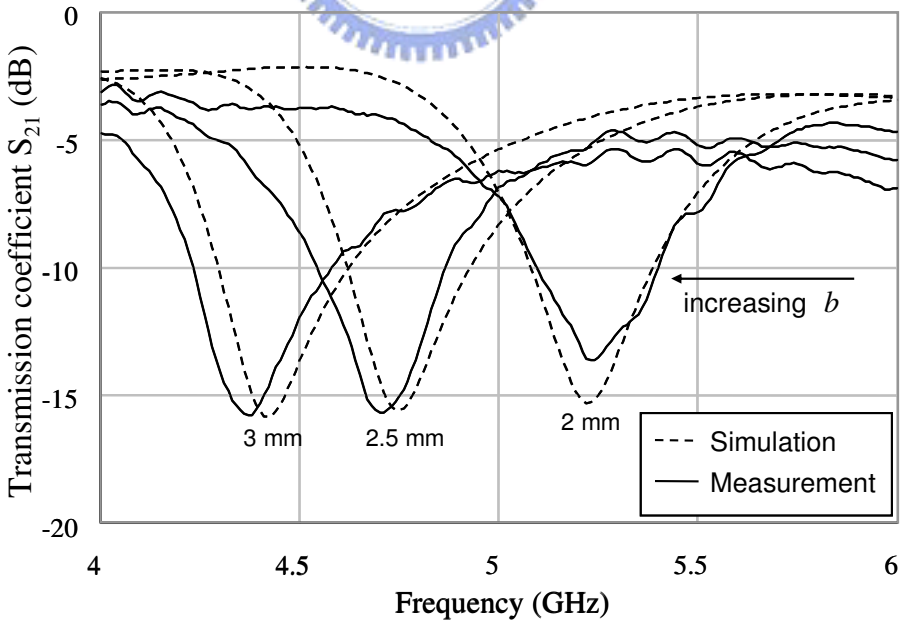
0
-5
-10
-15
-20
4
4.5
5
5.5
6
Transmission coefficient S_{21} (dB)
Frequency (GHz)
increasing b
3 mm
2.5 mm
2 mm
Simulation
Measurement

(b)

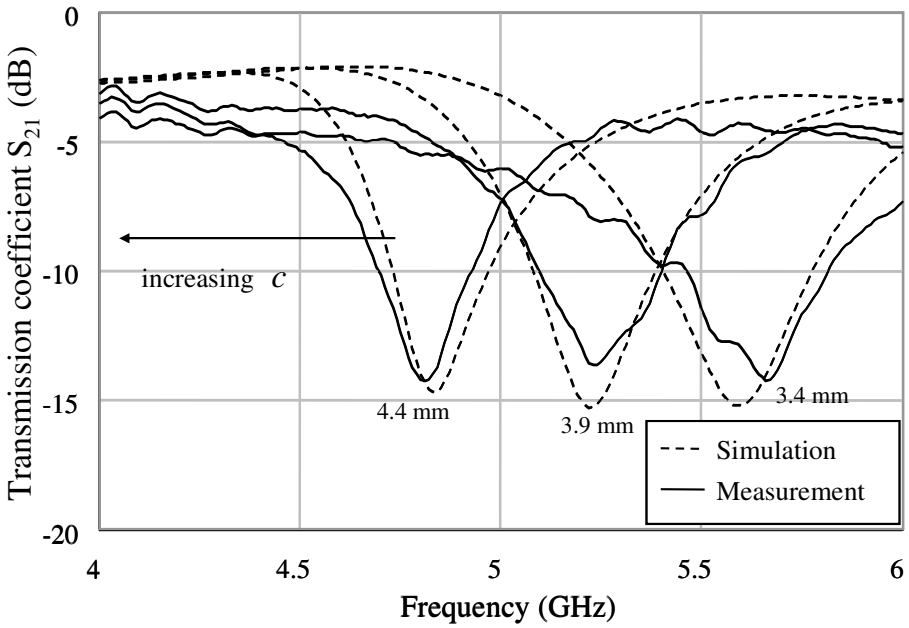

(c)

Figure 4.3 Simulated and measured transmission coefficients for the GECC of various sizes. (a)Frequency responses for the chokes of different length a with b = 2 mm and c = 3.9 mm. (b)Frequency responses for the chokes of different width b with a = 3.5 mm and c = 3.9 mm. (c)Frequency responses for the chokes of different strip length c with a = 3.5 mm and b = 2 mm. Other structure parameters are fixed as t = 1 mm, l = 0.5 mm, and s = 0.6 mm.

4.3 Decoupling Using GECC

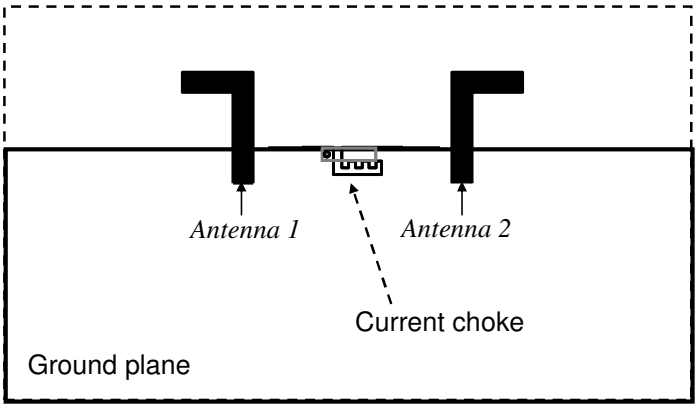

Figure 4.4 Structure of two nearby printed inverted-L antennas with a GECC in between.

In this section, another important application of the GECC is revealed, i.e., the decoupling of two nearby antennas. The antenna decoupling techniques have drawn a lot of attraction in recent years because of the growing demand of multiple-antennas system. The isolation between antennas affects the performance of the communication system. Many papers have discussed the methods of diminishing the coupling between antennas. For antennas with the common ground plane, blocking the coupling ground current between antennas is one of the decoupling approaches. As mentioned in Chapter I, the fish-bone like slot on the ground plane was proposed to prevent the coupling ground current [39]. Also, EBG structures are usually used to increase the isolation between patch antennas with common ground plane by blocking the surface wave.

To demonstrate the effectiveness of the proposed GECC on the enhancement of antenna isolation, let us consider two closely spaced printed inverted-L antennas operating at 5.25 GHz as shown in Figure 4.4. The antennas are designed on a 0.8 mm thick FR4 substrate with the same strip width as the previous antenna but a slightly larger length for better input impedance matching. The two antennas share the same ground plane with size of $L_2 \times W_2 = 40$ mm $\times$ 90 mm, and are separated with a distance l_g = 12.5 mm. Both antennas are fed by a small section of a 50 Ω microstrip line, which, in turn, is connected to a 50 Ω coaxial cable for measurement. To increase the isolation, a 5.25 GHz GECC as the previous example is placed in the middle of the two antennas on the ground edge.

Figure 4.5 and Figure 4.6 show the measured scattering parameters of the two antennas without and with, respectively, the insertion of the GECC. As seen from Figure 4.5, both the antennas are resonant at 5.25 GHz and well matched with return loss ($1/S_{11}$) better than 20 dB. However, the isolation ($1/S_{21}$) between antennas at the center frequency is only 8 dB, which is poor for many applications. Nevertheless, when the GECC is inserted, the isolation is greatly improved to 32 dB at 5.25 GHz as observed from Figure 4.6. The isolation is better than 20 dB over the bandwidth from 4.91 GHz to 5.37 GHz. The expense for the isolation improvement is the degradation of the return loss. Both the reflection coefficients of the antennas are raised in the considered frequency range, although they are still under -10 dB. (Note that the return-loss frequency responses of the two antennas are different due to the asymmetry of the GECC configuration.) If better return losses are required, the antennas need to be fine tuned or matching circuits can be used. Figure 4.7 shows the time-averaged current distribution on the antennas and ground plane from HFSS simulation, when antenna 1 is fed with antenna 2 terminated. Obviously, the GECC blocks the current from antenna 1 and keeps the ground near antenna 2 silent for good isolation. Both simulation and measurement results demonstrate the decoupling ability of the proposed GECC in multiple-antennas systems.

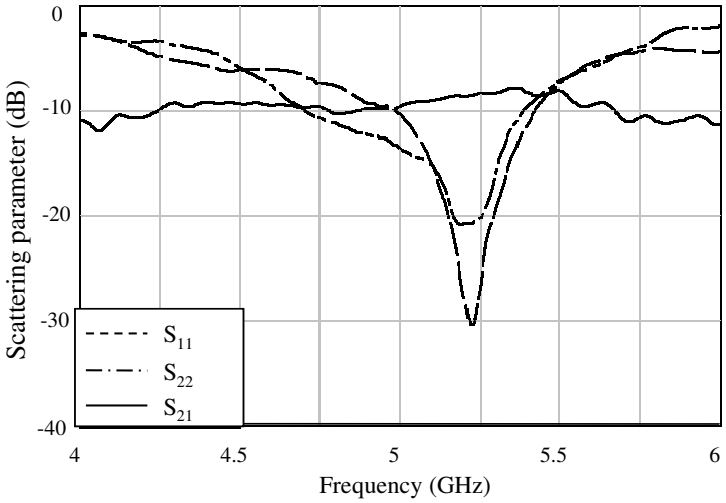

Figure 4.5 Measured scattering parameters for two printed inverted-L antennas without GECC in between.

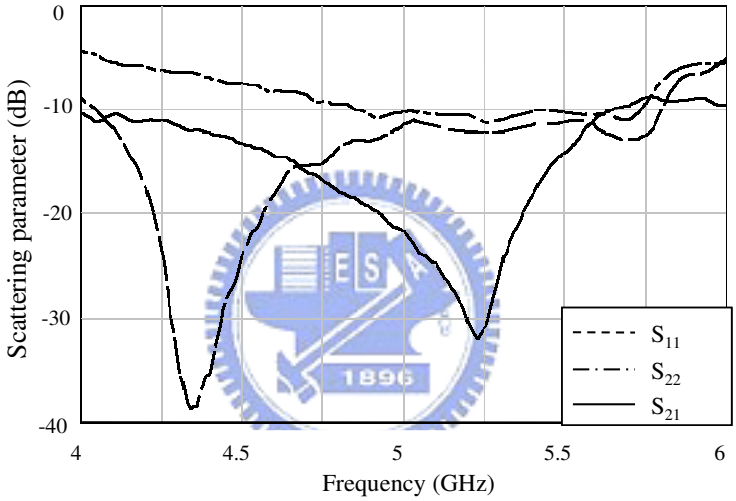

Figure 4.6 Measured scattering parameters for two printed inverted-L antennas with GECC in between.

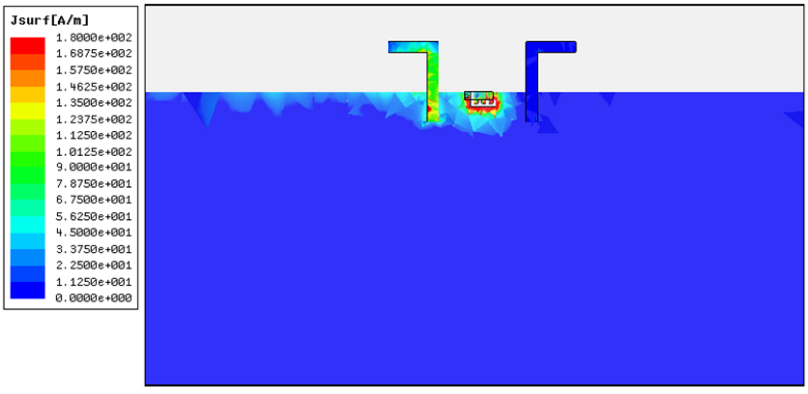

Figure 4.7 The time-averaged current distribution on the antennas and ground plane when antenna 1 is fed and antenna 2 is terminated.

4.4 Pattern Regulation Using GECC

There is another useful application, pattern regulation, can be implemented by using the same feature of blocking current. The printed monopole antenna is widely used for its simple configuration. Although many structure variations have been proposed, most of the designs adopted the quarter-wavelength resonance approach. In the microwave band, the quarter-wavelength monopole is small and can be easily fabricated on the same circuit board of the circuitry. For example, the monopole antenna length for the IEEE 802.11a WLAN system at 5 GHz band is only around 13 mm on an FR4 substrate. As compared to the size of the monopole radiator, the ground plane on the circuit board is usually much larger. For instance, the ground length (about 50 mm) of a small USB dongle is already near one wavelength of a 5 GHz signal. In this section, the radiation pattern of the monopole with long ground plane is to be considered with the application of the proposed GECC.

Consider a 5.25 GHz printed inverted-L monopole antenna fabricated on a 0.8 mm thick FR4 substrate, as shown in Figure 4.8(a). The length L_1 and width W_1 of the substrate ground plane are 50mm and 20mm, respectively. The monopole strip is with length of l_{m1} = 7 mm and l_{m2} = 6.8 mm and width of 1.5 mm. The antenna is fed by a small section of a 50 Ω microstrip line, which, in turn, is connected to a 50 Ω coaxial cable for measurement. Figure 4.8(b) shows the simulated and measured reflection coefficient (S_{11}) of the antenna. It is seen that the inverted-L monopole antenna is well matched around the center frequency. The resultant radiation patterns of co-polarization in the E plane (*y*-*z* plane) at 5.25 GHz are illustrated in Figure 4.9(a). Both the simulation and measurement are presented, showing agreement with each other. It is observed that, different from a typical radiation pattern (i.e., a digit "8" pattern in the E plane) of a monopole antenna, a tilted beam is formed in the present pattern. More power is radiated toward the -*y* direction, which is the direction of ground extension. In addition, there is a radiation null near the broadside direction. This weak broadside radiation and tilted beam pattern is not suitable for most mobile applications.

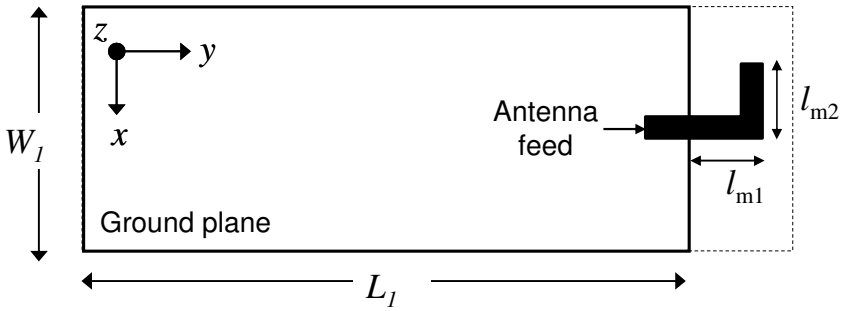

(a)

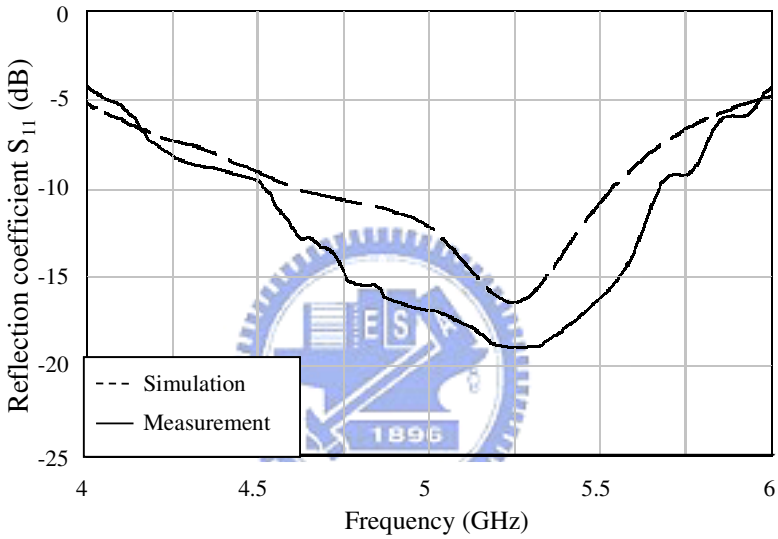

(b)

Figure 4.8 (a)Structure of the inverted-L monopole antenna with long ground plane. (b)Simulated and measured reflection coefficients of the inverted-L antenna.

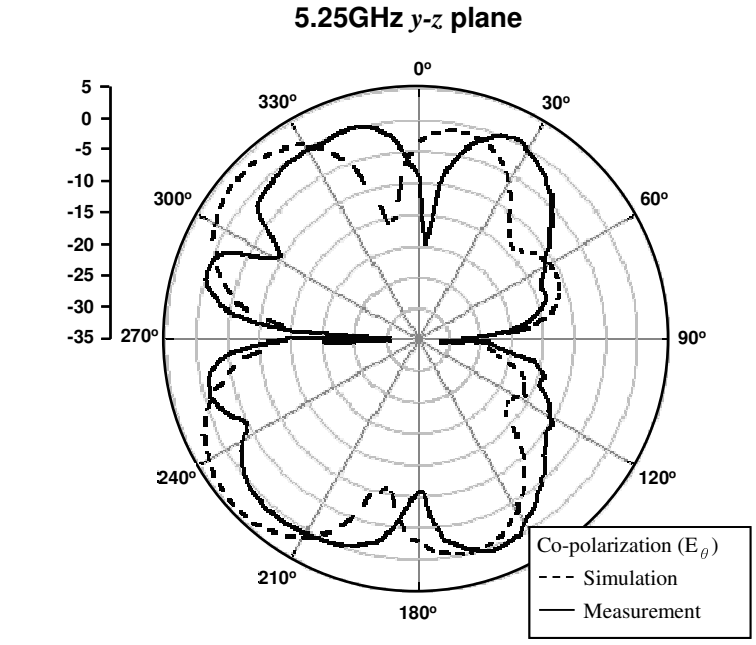

(a)

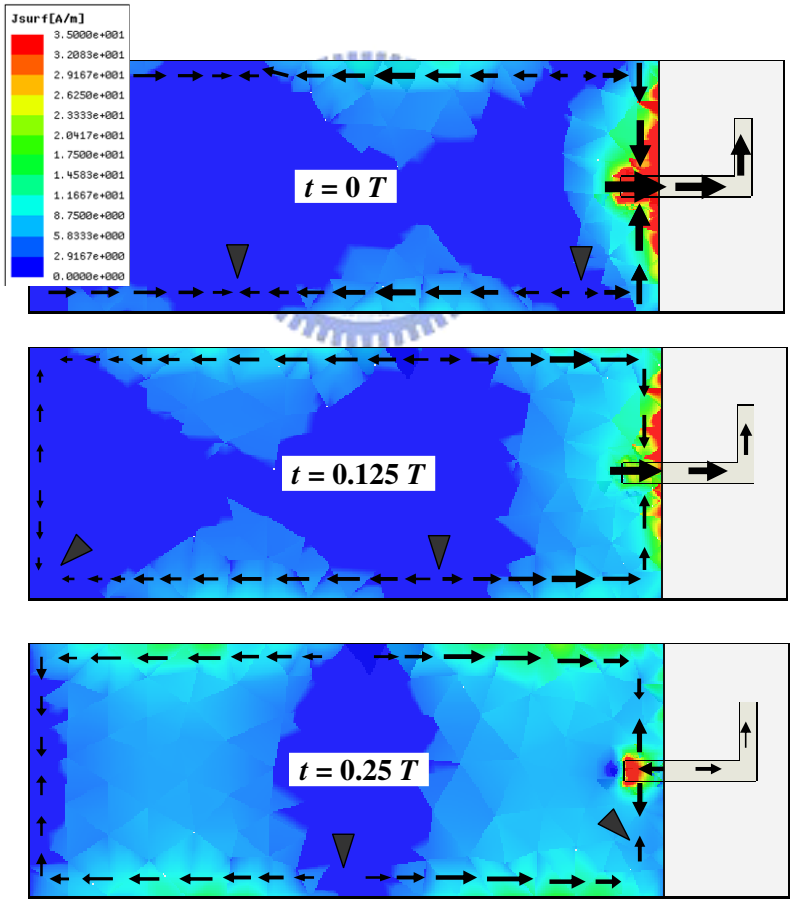

(b)

Figure 4.9 (a)Simulated and measured radiation patterns of the inverted-L antenna. (b)Current distributions in different time steps of the inverted-L antenna at 5.25 GHz. *T* is the time period of the signal at 5.25 GHz. The arrows indicate the current null positions.

To explain the deformation of the radiation pattern, the simulated current distribution on the ground plane in different time steps is plotted in Figure 4.9(b). It can be seen that the monopole radiator indeed behaves as a quarter-wavelength antenna. However, a close inspection on the ground plane current reveals that the ground current is a traveling-wave current, instead of a resonant one, propagating toward the -*y* direction. This can be observed from the moving of the current nulls with the advance of time. The long ground plane in this case acts like a traveling wave antenna, which contributes to a radiation field toward the (current) wave-propagating direction [60]. The combination of the fields from the inverted-L monopole and the ground plane leads to the radiation pattern shown in Figure 4.9(a).

To regulate the radiation pattern as a broadside radiation one, the traveling wave behavior of the ground plane current should be changed. For this purpose, the proposed GECC is designed to put at the two ground sides, as shown in Figure 4.10(a). As examined in the above section, the GECCs have the function of reflecting the incident current wave so that a standing-wave current distribution may be obtained along the ground edges. The required structure parameters of the GECC for a resonant frequency at 5.25 GHz are designed as a = 3.5 mm, b = 2 mm, c = 3.9 mm, t = 1 mm, l = 0.5 mm, and s = 0.6 mm. Also, the position of the GECCs is properly chosen at l_d = 15 mm, which is located near the current null at t = 0 in Figure 4.9(b). Figure 4.10(b) shows the simulated and measured reflection coefficients of the inverted-L monopole antenna with a GECC-embedded ground plane. The antenna is still well matched and has a return-loss frequency response similar to that without the GECCs. Figure 4.11(a) depicts the simulated and measured radiation patterns of co-polarization in the E plane at 5.25GHz for the GECC-embedded antenna. A significant difference is observed that the pattern becomes a digit “8” pattern that meets the expectation. The antenna pattern has changed from one with tilted beam to a broadside radiation one after the use of the GECCs. To confirm the current blocking effect of the GECCs, the time-averaged current distribution combined with instant maximum current vector distribution are examined and plotted in Figure 4.11(b). The scale of the current level is the same as that in Figure 4.9(b) for comparison. The current along the two sides of the ground plane has been blocked by the GECCs as expected. An effective open circuit caused by the GECC forces

the current turning to be a standing wave, instead of a traveling wave, thus adjusting the radiation pattern to a broadside one.

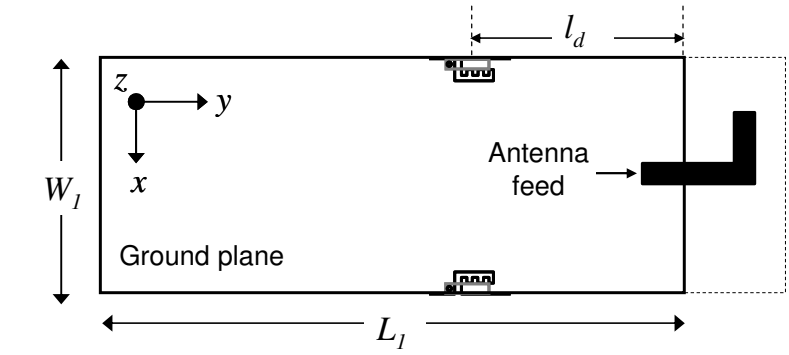

(a)

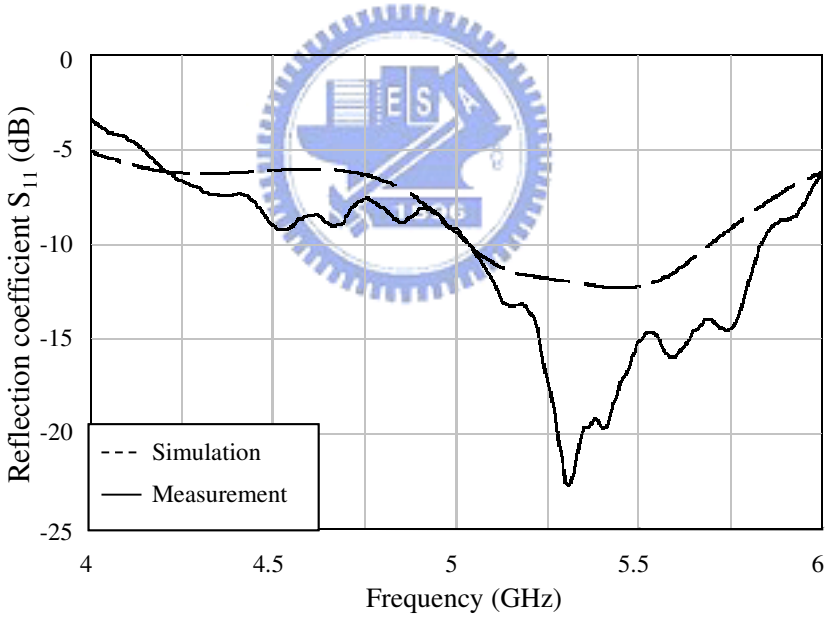

(b)

Figure 4.10 (a)Structure of the inverted-L monopole antenna with GECC. (b)Simulated and measured reflection coefficients of the inverted-L antenna with GECC.

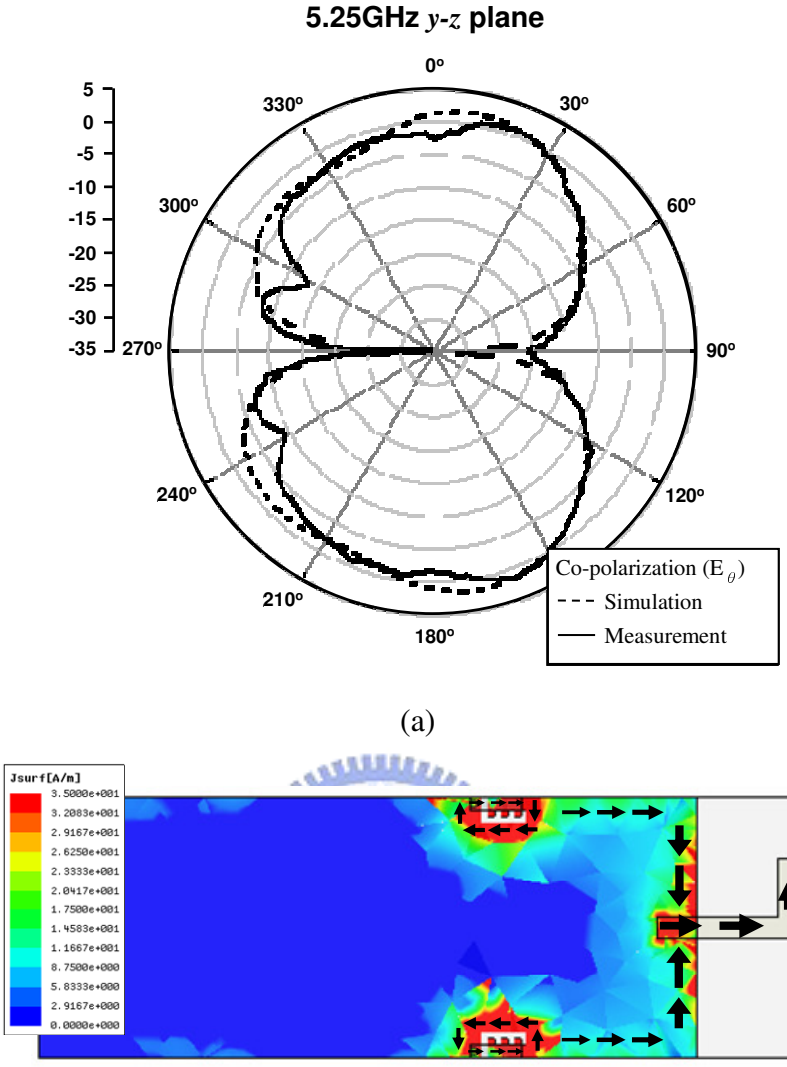

(a)

(b)

Figure 4.11 (a)Simulated and measured radiation patterns of the inverted-L antenna with GECC. (b)The time-averaged current distribution combined with an instant current vector distribution on the ground plane of the inverted-L antenna with GECC.

4.5 Summary

A miniaturized ground edge current choke (GECC) and its applications have been proposed. The GECC is a parallel combination of an open slit and an overlapping strip implemented on the edge of a ground plane. The slit behaves as an inductor and the strip a capacitor. By introducing the GECC on the ground edge, an effective electrical open circuit provided by the parallel LC circuit can be performed to block the current flowing along the ground plane edge. The design and the measurement of the choke have been presented. The resonant frequency of the choke can be easily determined by the sizes of the open slit and overlapping strip. The proposed evaluation approach for the GECC by using the transmission line method has been proved effective. Two applications of the proposed GECC have been examined. The first one by using the GECC to block the traveling-wave current induced along the ground edge of a small antenna demonstrated the feasibility of the proposed structure on regulating the antenna radiation pattern. And the second application showed the ability of the GECC to enhance the isolation between two nearby antennas. The experimental results agreed well with the simulation.

The proposed printed GECC has the advantages of compact size and ease of fabrication, which can be used in more applications. For a lower operation frequency, such as 900 MHz or 1800MHz, the required inductance and capacitance should be increased for resonance at the design frequency. With the same size, the printed capacitor can be replaced by SMD capacitor to gain larger value for lower operation frequency. However, if only the capacitance is increased but without increasing the inductance, the fractional bandwidth might be too narrow to be used. To increasing the inductance along the current path, a magnetic material, like ferrite, may be used so as to increasing the inductance and thus the bandwidth.

Chapter 5 Conclusions

For the requirement of compact antennas and decoupling techniques, a series of miniaturized antennas and decoupling methods has been developed. The operational principles and theories of these designs have been studied and demonstrated by using equivalent circuits. The equivalent circuit has also been proved of a useful method for compact antenna design.

In miniaturized antenna design, there are four kinds of antennas being proposed. To further understand the miniaturization methods, two different concepts were considered, the concept involved wavelengths for resonance and circuit approach instead of wavelengths for resonance. An important task of this dissertation is to prove that circuit approach method can bring compact and efficient antennas in an efficient way. About different concepts, both lead to successful designs.

The first proposed antenna by spiraling the conventional inverted-F antenna has 50%-size reduction and maintains the radiation efficiency. Also, the dual-band mechanism, which utilizes two resonant modes in one resonator, has been explained by using the equivalent circuit. This design successfully achieves the miniaturization and dual-band operation simultaneously. The antenna size of 9.5 mm by 6.5 mm for 2.4/5.2GHz band that is compact for most applications. The second proposed antenna by using dielectric load, with relative permittivity of 40, on QHA has great size reduction to 2.7% of air-loaded one. The related equivalent circuit has also explained impedance feature of self-phasing circular polarized QHA and the observed impedance curve can help to tune the circular polarization state. However, the small antenna size causes small radiation resistance that shrinks the impedance bandwidth. The matching structure was proposed for impedance matching. For narrow bandwidth operation of GPS, the proposed small QHA is sufficient.

The third proposed antenna adopts the circuit approach design. The resonance is achieved by circuit synthesis based on the concept of cascaded right/left handed transmission line with opposite phase delay. The antenna layout is formed by using printed elements corresponding to the equivalent lumped circuit of transmission line. In fact, this method can be considered as a sub-category of the general π and T models.

From experiments, it is proved that the resonant frequency can be synthesized by the circuit design without being affected by ground size. Also, the radiation mechanism was discussed. The most radiation from slot radiator has been confirmed. The circuit approach design has many design parameters thus flexible. The proposed type for 2.4GHz is finished inside 11.5 mm by 11.5 mm that is slightly larger than spiraled inverted-F antenna because of the size of printed capacitors. However, it proved the design concept of circuit approach and it can be further reduced by changing design parameters. Based on the short slot radiator that is proved of efficient radiation, the fourth antenna by using SMD elements on the slot has smaller size than using printed element for the entire layout. The design still starts with the equivalent circuit. The radiation resistor is considered in this design. The developed circuit structure of this antenna is simpler than the third antenna thus saving layout elements. The antenna for 2.4GHz band only with a short slot radiator (9 mm by 1.5 mm) and two SMD capacitors is more compact than previous designs. From the experiments, the equivalent circuit has shown its accuracy for antenna design. The impedance bandwidth is sufficient for IEEE802.11b/g. The radiation efficiency is fairly good according to the measured radiation patterns and gains. It is worth to notice that the frequency tunable type is developed from the same configuration. The lower frequency was achieved in this type using same slot radiator. Although the tuning range is determined on varactors, the realized antenna has measured tuning range from 1.7GHz to 2.8GHz. It means the proposed antenna configuration is very flexible and compact. All proposed miniaturized antennas have revealed their equivalent circuit model. Developing different kinds of miniaturization methods helps to understand the features of the miniaturized antenna more deeply.

The proposed miniaturized decoupling structures also follow the concept of circuit approach. Based on the LC parallel resonator, the ground edge current choke (GECC) has been developed using printed capacitor and inductor. Its function of blocking ground edge current is proved from the experiments of two presented applications. The decoupling function in 5GHz has been evaluated successfully. The simulated current distribution shows that it prevents the nearby antenna from the coupling current induced by the driven antenna. The GECC for 5GHz band is 3.5 mm by 2 mm that is compact to be inserted along the ground edge. For the further size

reduction and more flexible use, the decoupling circuit is developed. It can enhance the port isolation for any two nearby antennas that solves the efficiency problem due to the coupling. The circuit structure is compact that consists of two segments of transmission line and a lumped element. The formulas for circuit design have also been developed. In a series of experiments, the circuit structure has been proven that the decoupling function works and the formulas can design the circuit. The proposed two decoupling methods are compact. Their flexible design can be used in most applications.

References

[1] H. Morishita, "A study on compact antennas and antenna miniaturization for handsets," in *IWAT* 2008, 4-6 March, 2008, pp. 28-31.

[2] A. J. Paulraj, etc., "An overview of MIMO communications – A key to gigabit wireless," *Proc. of IEEE*, vol. 92, no. 2, pp. 198-218, Feb., 2004.

[3] T. Hult and A. Mohammed, "Compact MIMO antennas and HAP diversity for data rate communications," in *Vehicular Technology Conference*, Apr., 2007, pp. 1385-1389.

[4] Y. Chung, S. S. Jeon, D. Ahn, J. I. Choi, and T. Itoh, "High isolation dual-polarized patch antenna using integrated defected ground structure," *IEEE Microwave Wireless Comp. Lett.*, vol. 14, no. 1, pp. 4-6, Jan. 2004.

[5] R. Azadegan and K. Sarabandi, "A novel approach for miniaturization of slot antennas," *IEEE Trans. Antenna Propag.*. Vol. 51, No. 3, pp. 421-429, Mar. 2003.

[6] K. Van Caekenberghe, N. Behdad, K. M. Brakora, K. Sarabandi, "A 2.45-GHz Electrically Small Slot Antenna," *IEEE Antennas Wireless Propag. Lett.*, vol. 7, pp. 346-348, 2008

[7] R. Azadegan and K. Sarabandi, "Design of miniaturized slot antennas," in *IEEE AP-S Int. Symp.*, vol. 4, July 2001, pp. 565-568.

[8] E. J. Kim, H. H. Jung, Y. S. Lee, and Y. K. Cho, "Compact meander slot antenna with open-ends," in *Microwave Conference Korea-Japan*, Nov. 2007, pp. 69-72.

[9] S. K. Padhi, G. F. Swiegers, and M. E. Bialkowski, "A miniaturized slot ring antenna for RFID applications," in *Int. Conf. Microwaves, Radar and Wireless Communications*, vol. 1, May 2004, pp. 318-321.

[10] G.-Y. Lee, Y. Kim, J.-S. Lim, and S. Nam, "Size reduction of microstrip-fed slot antenna by inductive and capacitive loading," in *IEEE AP-S Int. Symp.*, Vol. 1, June 2003, pp. 312-315.

[11] M. C. Scardelletti, G. E. Ponchak, S. Merritt, J.S. Minor, and C. A. Zorman, "Electrically small folded slot antenna utilizing capacitive loaded slot lines," in *IEEE Radio Wireless Symp.,* Jan. 2008, pp. 731-734.

[12] T. L. Simpson, "The disc loaded monopole antenna," *IEEE Trans. Antenna Propag.* vol. 51, no. 2, pp. 542-550, Feb. 2004.

[13] Y. L. Kuo, Y. T. Cheng, and K. L. Wong, "Printed inverted-F antennas for applications in wireless communication," in *IEEE AP-S Int. Symp.*, vol. 3, June 2002, pp.454-457.

[14] S. H. Yeh and K. L. Wong, "Dual-band F-shaped monopole antenna for 2.4/5.2

GHz WLAN application," in *IEEE AP-S Int. Symp.* vol.4, June 2002, pp.72-75.

[15] J. Y. Jan, L. C. Tseng, W. S. Chen and Y. T. Cheng, "Printed monopole antennas stacked with a shorted parasitic wire for Bluetooth and WLAN applications," in *IEEE AP-S Int. Symp.* , vol.3, June 2004, pp. 2607-2610.

[16] E. S. Angelopoulos, A. I. Kostaridis, and D. I. Kaklamani, "A novel dual-band F-inverted antenna printed on a PCMCIA card," *Microwave and Optical Technology Lett.*, vol. 42, pp. 153-156, May 2004.

[17] C. M. Su, K. L. Wong, W. S. Chen, and Y. T. Cheng, "Microstrip-coupled printed inverted-F monopole antenna", *Microwave and Optical Technology Lett.*, vol. 43, pp. 470-472, Dec. 20, 2004.

[18] Y. D. Lin and P. L. Chi, "Tapered bent folded monopole for dual-band wireless local area network (WLAN) systems," *IEEE Antennas Wireless Propag. Lett.*, vol.4, pp. 355-357, 2005.

[19] W. C. Liu, "Broadband dual-frequency meandered CPW-fed monopole antenna," *Electronics Lett.*, vol.40, pp. 1319-1320, 14 Oct. 2004.

[20] H. M. Chen and Y. F. Lin, "Printed monopole antenna for 2.4/5.2 GHz dual-band operation," in *IEEE AP-S Int. Symp*, vol.3, June 2003, pp. 60-63.

[21] D. M. Pozar, *Microwave Engineering*, 3nd ed. New York: Wiley, 2005.

[22] K. Y. Hui and K. M. Luk, "A miniature dielectric resonator loaded patch antenna," *IEEE Trans. Antennas Propag.*, vol 53, no. 6. pp. 2118-2122, June 2005.

[23] Y.-F. Lin, C.-H. Lin, H.-M. Chen, and P. S. Hall, "A Miniature Dielectric Loaded Monopole Antenna for 2.4/5 GHz WLAN Applications," *IEEE Microwave Wireless Comp. Lett.*, vol. 16, no. 11, pp. 591-593, 2006.

[24] C. Caloz and T. Itoh, "Novel microwave devices and structures based on the transmission line approach of meta-materials," *IEEE MTT-S Int. Microwave Symp. Dig.*, Jun. 2003, pp. 195-198.

[25] A. Sanada, C. Caloz, and T. Itoh, "Novel zeroth-order resonance in composite right/left-handed transmission line resonators," in *Proc. Asia-Pacific Microwave Conf.*, Seoul, Korea, Nov. 2003, pp. 1588-1592.

[26] A. Sanada, M. Kimura, I. Awai, C. Caloz, and T. Itoh, "A Planar zeroth-order resonator antenna using a left-handed transmission line," in *European Microwave Conference*, Amsterdam, Netherlands, Oct. 2004, pp. 1341-1344.

[27] C.-J. Lee, K. M. K. H. Leong, and T. Itoh, "Design of resonant small antenna using composite right/left-handed transmission line," in *IEEE AP-S Int. Symp.*, Jul. 2005, vol. 2B, pp. 218-221.

[28] A. Lai, K. M. K. H. Leong, and T. Itoh, "Dual-mode compact microstrip antenna based on fundamental backward wave," in *Proc. Asia-Pacific Microwave Conf.*,

vol.4, Suzhou, China, Dec. 2005.

[29] G. J. Foschini and M. J. Gans, “On limits of wireless communications in a fading environment when using multiple antennas,” *Wirel. Pers. Commun.*, 1998, vol. 6, no. 3, pp. 331-335.

[30] F. Yang and Y. R. Samii, “Microstrip antennas integrated with electromagnetic band-gap EBG structures: a low mutual coupling design for array applications” *IEEE Trans. Antennas Propag*., vol. 51, no. 10, pp. 2936-2946, Oct. 2003.

[31] Z. Iluz, R. Shavit, and R. Bauer, “Microstrip antenna phased array with electromagnetic bandgap substrate,” *IEEE Trans. Antenna Propaga.*, vol. 52, no. 6, pp.1446-1453, June 2004.

[32] L. Yang, M. Fan, F. Chen, J. She, and Z. Feng, “A novel compact electromagnetic-bandgap (EBG) structre and its applications for microwave circuits,” *IEEE Tran. Microwave Theory Tech.*, vol. 53, no. 1, pp.183-190, Jan. 2005.

[33] A. Diallo, C. Luxey, P. L. Thuc, R. Staraj, and G. Kossiavas, “Study and reduction of the mutual coupling between two mobile phone PIFAs operating in the DCS1800and UMTS bands,” *IEEE Trans. Antennas Propag.*, vol. 54, no. 11, pp. 3063-3073, Nov. 2006.

[34] A. Diallo, C. Luxey, P. L. Thuc, R. Staraj, G. Kossiavas , M. Franzen, and P.-S. Kildal, “MIMO performance of enhanced UMTS four-antenna structures for mobile phones in the presence of the user’s head,” in *Proc. IEEE AP-S Int. Symp*., Jun. 2007, pp. 2853-2856.

[35] A. Diallo and C. Luxey, "Estimation of the diversity performance of several two-antenna systems in different propagation environments," in *IEEE AP-S Int. Symp.*, Jun. 2007, pp. 2642-2645.

[36] A. Diallo, C. Luxey, P. L. Thuc, R. Staraj, and G. Kossiavas, “Enhanced two-antenna structures for universal mobile telecommunications system diversity terminals, *IET Microwaves, Antennas and Propagation*, Vol. 2, no. 1, pp. 93-101, Feb. 2008.

[37] S. Ranvier, C. Luxey, P. Suvikunnas, R. Staraj, and P. Vainikainen, “Capacity enhancement by increasing both mutual coupling and efficiency: a novel approach,” in *IEEE AP-Symp*., Honolulu, Hawaii, June 2007.

[38] J. Andersen and H. Rasmussen, “Decoupling and descattering networks for antennas,” *IEEE Trans. Antennas Propag.*, vol. 24, pp. 841-846, Nov. 1976.

[39] C. Y. Chiu, C. H. Cheng, R. D. Murch, and C. R. Rowell, “Reduction of mutual coupling between closely-packed antenna element,” *IEEE Tran. Antenna Propag.*, vol. 55, no. 6, pp.1732-1738, June 2007.

[40] M. Yamamoto and K. Itoh, “Behaviour of the parallel plate mode in a stripline

slot-coupled patch antenna," *IEE Proc. Microw. Antennas Propag.* Vol. 147, No. 5, pp. 385-389, Oct. 2000. (phy 1 pat)

[41] G. Tzeremes, Tsai S. Liao, Paul K. L. Yu, and C. G.. Christodoulou, "Computation of equivalent circuit models of optically driven CPW-fed slot antennas for wireless communications," *IEEE Antennas Wireless Propag. Lett*., Vol. 2, 2003, pp. 140-142. (phy 2 mm)

[42] K. Ram babu, M. Ramesh and A.T. Kalghatgi, "Broadband equivalent circuit of a dipole antenna," *IEE Proc. Microw. Antennas Propag.* Vol. 146, No. 6, pp. 391-393, Oct. 2000. (phy 3 fff)

[43] A. A. Kishk, X. Zhang, A. W. Glisson, and D. Kajfez, "Numerical analysis of stacked dielectric resonator antennas excited by a coaxial probe for wideband applications," *IEEE Tran. Antenna Propag.*, vol. 51, no. 8, pp.1996-2006, Aug. 2003. (phy 5)

[44] S. B. T. Wang, A. M. Niknejad, and R. W. Brodersen, "Circuit modeling methodology for UWB omnidirectional small antennas," *IEEE J. Sel. Areas Commun*, Vol. 24, No. 4, pp. 871-877, Apr. 2006. (time 1)

[45] J. Bernardes, F. Peterkin, B. Hankla, and J. Latess, "Antenna circuit model for time-domain transient analysis," *IEEE Digest. Pulsed Power Conference,* Vol. 1, 27-30 June 1999 pp. 260-263.

[46] C. Wu, "Printed antenna structure for wireless data communications," U.S. Patent 6 008 774, Dec. 28, 1999.

[47] C. Soras, M. Karaboikis, G. Tsachtsiris, and V. Makios, "Analysis and design of an inverted-F antenna printed on a PCMCIA card for the 2.4 GHz ISM band," *IEEE Antennas Propag. Mag.*, vol. 44, pp. 37-44, Feb. 2002.

[48] V. Stoiljkovic and G. Wilson, "A small planar inverted-F antenna with parasitic element for WLAN applications," *10th International Conference on Antennas and Propagation*, vol.1, pp. 82-85, April 1997.

[49] T. Tiehong and Z. Zheng, "Applications of planar inverted-F antenna for Bluetooth," in *Proc. 2003 International Conference on Communication Technology*, April 2003, vol.2, pp. 1230-1233.

[50] IE3D, Zeland Software Inc, CA, USA.

[51] R. Bricker and H. Rickert, "An S-band resonant quadrifilar antenna for satellite communication," in *Proc. IEEE AP-S Int. Symp*., vol. 12, pp. 78-82, June 1974.

[52] C. Kilgus, "Resonant quadrafilar helix," *IEEE Trans. Antennas Propag.*, vol. 17, no. 3, pp. 349-351, May 1969.

[53] G. Nicolaidis, O. Leisten, and Y. Vardaxoglou, "Measurement of Dielectrically Loaded Antennas for Mobile Phone Handsets," in *ARMMS*, 23-24 Nov. 1998, Worcester, UK.

[54] G. Nicolaidis, O. Leisten, and J. C. Vardaxoglou, “TLM investigation of dielectric loaded bifilar personal telephone antennas,” *Proc. Nat. Conf. Antennas Propag*., Vol. 461, pp. 16-18, April 1999.

[55] Murata Manufacturing Co., ltd. (http://www.murata.com)

[56] H. X. Xue, P. B. Kenington and M. A. Beach, “A high performance ultra-broadband RF choke for microwave application,” *IEE Colloquium on Evolving Tech. for Small Earth Station Hardware*, pp. 1-4, 1995.

[57] Y.-C. Jeong, S.-G. Jeong, J.-S. Lim, and S. Nam, “A new method to suppress harmonics using $\lambda/4$ bias line combined by defected ground structure in power amplifiers,” *IEEE Microwave Wireless Comp. Lett.*, vol. 13, no. 4, pp. 538-540, Dec. 2003.

[58] Y. Chung, S.-S. Jeon, D. Ahn, J.-I. Choi, and T. Itoh, “High isolation dual-polarized patch antenna using integrated defected ground structure,” *IEEE Microwave Wireless Comp. Lett.*, vol 14, no. 1, pp. 4-6, Jan, 2004.

[59] Choi, V. Govind and M. Swaminathan, "A novel electromagnetic bandgap (EBG) structure for mixed-signal system applications," in *IEEE radio and wireless conference*, 19-22 Sept. 2004, pp. 243-246.

[60] W. L. Stutzman and G. A. Thiele, *Antenna Theory and Design*. New York: Wiley, 1998.

[61] A. A. Kishk, L. Shafai, and A. Ittipiboon, “Improvement in radiation characteristic of coaxial feds using a quater-wavelength choke,” *Electronics Lett*., vol. 20, no. 12, pp. 522-523, 1984.

[62] K. Miyata and M. Suzuki, “Effects of choked-load position on radiation properties in double-choked small horn antennas,” *Electronics Lett*., vol. 19, no. 9, pp. 329-330, 1983.

[63] S.Noghanian and L.Shafai, “Gain enhancement of annular slot antennas,” *IEE Proc. Microw Antennas Propag*., vol. 148, no. 2, pp. 109-114, Apr. 2001.

[64] L. I. Basilio, J. T. Williams, D. R. Jackson, and M. A. Khayat, “A comparative study of a new GPS reduced-surface-wave antenna,” *IEEE Antennas Wireless Propag. Lett*., vol. 4, pp.233-236, 2005.

[65] C. C. Tchapwou and T. Bertuch, “Investigation of EBG surface performance for high-precision GPS applications,” *Electronics Lett*. vol. 43, no. 24, pp. Nov. 2007.

[66] K. T. Chen, Y. S. Wang, and S.-J. Chung, “A new printed dual-band monopole antenna with a short stub,” in *Int. Conf. on Antennas, Radar, and Wave Propagation*, Banff, Canada, July 19-21, 2005.

[67] P. Lindberg and E. Ojefors, “A bandwidth enhancement technique for mobile handset antennas using wavetraps,” *IEEE Tran. Antenna Propag*., vol. 54, no. 8, pp.2226-2233, Aug. 2006.

Appendix A Decoupling Circuit Network

In this section, a miniaturized structure to achieve high port isolation between two antennas is proposed. The decoupling structure is accomplished on the circuit board. Formulas for decoupling circuit construction are developed. The required parameters of the structure are derived based on the measured or simulated coupling coefficient between antennas. The circuit-approach decoupling can achieve good isolation between two antenna input ports. However, the driving antenna can still induce the current on the other antenna although the power will not deliver to its port terminal. The driven current on antenna has also be studied in this section.

A1. Operational Principle

It is usually easy to design the input impedances but hard to reduce the coupling between two closely spaced antennas. In this study, a dual antenna system (Ant.1 and Ant. 2 in Figure A.1) with good input impedance matching but poor port isolation is first assumed. For simplicity, the antennas are symmetrical to each other and have input impedance of Z_0 (= 50Ω). A four-port decoupling network is proposed, with two output ports connected to the antennas, for reducing the coupling between the two resultant new input ports. Each input port is in turn connected to a matching network for improving the input impedance. Figure A.1 shows the function blocks of the decoupling structure.

The decoupling network consists of two transmission lines with characteristic impedance Z_0 and electrical length θ and a shunt reactive component with admittance jB. Let the scattering matrix of the coupled antennas be denoted as $[S^A]$ at the reference plane t_1. After connecting the transmission lines, the new scattering matrix at the reference plane t_2 is expressed as $[S^{A'}]$. $[S^B]$ is the scattering matrix at the reference plane t_3 after the addition of the shunt lumped element. Finally, the total scattering matrix at the reference plane t_4, including the antennas, the decoupling network, and the matching networks, is indicated as [S].

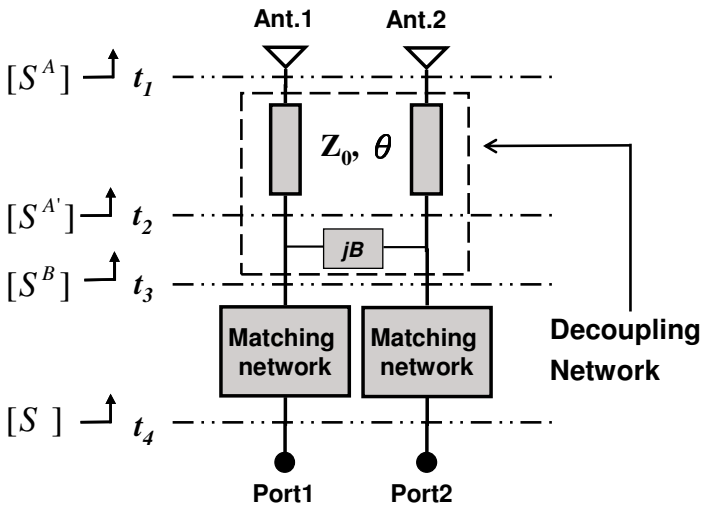

Figure A.1 The function blocks of the proposed decoupling structure, including two transmission lines, a shunt reactive component, and two impedance matching networks.

Since the coupled antennas are assumed with good input matching, the diagonal terms of $[S^A]$ approximately vanish, and the scattering matrix at t_1 can thus be expressed as

$$[S^A] = \begin{bmatrix} 0 & \alpha e^{j\phi} \\ \alpha e^{j\phi} & 0 \end{bmatrix} \tag{A-1}$$

where α and ϕ are the magnitude and phase of the coupling coefficient between antennas. After adding a transmission line of the same impedance Z_0 to each antenna port, the return loss remains infinite (or, $S_{11} = 0$), while the coupling coefficient experiences an extra phase delay of 2θ. Thus, the scattering matrix at t_2 can be described as

$$[S^{A'}] = \begin{bmatrix} 0 & \alpha e^{-j(2\theta-\phi)} \\ \alpha e^{-j(2\theta-\phi)} & 0 \end{bmatrix} \tag{A-2}$$

Once this scattering matrix is known, the corresponding admittance matrix $[Y^{A'}]$ can be easily derived [21].

As shown in Figure A.1, the two-port network seen at t_2 is in shunt with a reactive element of susceptance B, and thus the resultant new two-port network, i.e., that with ports at t_3, should have an admittance matrix $[Y^B]$ equal to

$$[Y^B] = [Y^{A'}] + [Y^b] \tag{A-3}$$

where $[Y^b]$ is the admittance matrix of the two-port network composed of the shunt

component,

$$[Y^b]=\begin{bmatrix} jB & -jB \\ -jB & jB \end{bmatrix} . \tag{A-4}$$

Therefore, the components of $[Y^B]$ can be derived as

$$Y_{21}^B = Y_{12}^B = Y_0\left(\frac{-2\alpha e^{-j(2\theta-\phi)}}{1-\alpha^2 e^{-j2(2\theta-\phi)}}\right) - jB \tag{A-5}$$

and

$$Y_{11}^B = Y_{22}^B = Y_0\left(\frac{1+\alpha^2 e^{-j2(2\theta-\phi)}}{1-\alpha^2 e^{-j2(2\theta-\phi)}}\right) + jB \quad . \tag{A-6}$$

The components of the scattering matrix $[S^B]$ at t_3 are related to these components through the following formulas:

$$S_{21}^B = \frac{-2Y_{21}^B Y_0}{Y_0^2 + 2Y_{11}^B Y_0 + (Y_{11}^B)^2 - (Y_{21}^B)^2} \tag{A-7}$$

$$S_{11}^B = \frac{Y_0^2 - (Y_{11}^B)^2 + (Y_{12}^B)^2}{Y_0^2 + 2Y_{11}^B Y_0 + (Y_{11}^B)^2 - (Y_{21}^B)^2} \tag{A-8}$$

where Y_0 represents the characteristic admittance of the input ports, $Y_0 = 1/Z_0$.

Since our purpose is to eliminate the coupling of the two ports, the coupling coefficient $S_{21}{}^B$ at t_3 should be zero, which means that, from (A-7), the trans-admittance Y_{21}^B should vanish. Then, from (A-5), the required electrical length θ and the susceptance B can be solved:

$$\theta = \frac{1}{2}\left(\phi \pm \frac{\pi}{2}\right) \tag{A-9}$$

and

$$B = \pm\frac{2\alpha}{1+\alpha^2} Y_0 \quad . \tag{A-10}$$

Both of these values are physically realizable, since both positive and negative values of B are possible (positive B implies a capacitor and negative implies an inductor). However, a shunt capacitor is preferred, since a negative B corresponds to a negative θ (ϕ is negative due to close spacing between antennas), which means longer transmission lines (longer than half wavelength) are required.

The solution of (A-9) is quite obvious, which shows that the coupling coefficient

after the introduction of the transmission lines should possess a phase $(-2\theta+\phi)$ equal to $\mp 90^{o}$. As revealed in (5), when this condition holds, the trans-admittance $Y_{21}^{A'}$ at t_2 would be pure imaginary, and can thus be cancelled by the reactive component jB. The transmission lines have the functions of not only delay lines of connecting the antenna input ports to the decoupling network, but also transferring the complex trans-admittance at the coupled antennas to a pure imaginary one. The solutions of (A-9) and (A-10) can be cast into (A-6) to get the input admittances Y_{11}^{B} and Y_{22}^{B} at t_3. Further impedance matching network is required to transfer these input admittances to the system admittance Y_0. A simple L-section matching network, which uses a series and a shunt reactive element, can usually accomplish the requirement.

A2. Derivation of Antenna Driving Currents

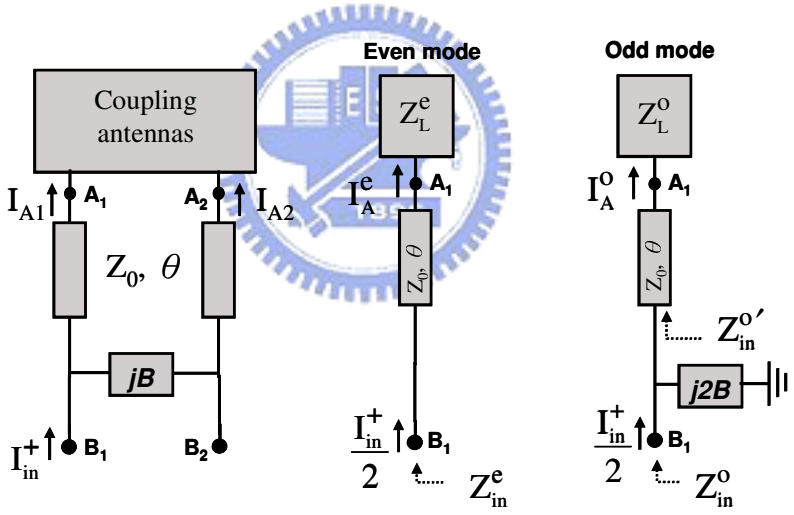

(a) (b) (c)

Figure A.2 (a)The coupled antennas in connection with the decoupling network. (b)The corresponding even-mode circuit, and (c) the odd-mode circuit.

Due to the close coupling between the two antennas and the introduction of the decoupling network, both the antennas will be excited even if the input power is only fed to one port. The antennas form a two-element array, with the radiation pattern determined by the excited currents on the antennas. Consider now that port 1 is fed by a current source and port 2 is terminated by Z_0. Let the input current, after passing the impedance matching network, at the reference plane t_3 (or point B_1 of

Figure A.2(a)) be denoted as I_{in}^{+}. Note that since at point B_1 the impedance is not matched, this input current would cause a returning current propagating back to the impedance matching network. In order to estimate the radiation pattern, the resultant driving currents I_{A1} and I_{A2} at the input points (points A_1 and A_2) of the two coupled antennas are to be derived through the even and odd modes analysis. To this end, the two-port coupled antennas are first modeled by a T network. Then, by setting the connecting points at the symmetric plane as open-circuits for the even mode and short-circuits for the odd mode, the even-mode and odd-mode circuit schematics can be obtained as shown in Figure A.2(b) and (c), respectively. The even-mode (Z_L^e) and odd-mode (Z_L^o) antenna load impedances at point A_1 are derived as

$$Z_L^e = Z_{11}^A + Z_{12}^A = Z_0 \frac{1+\alpha e^{j\phi}}{1-\alpha e^{j\phi}} \tag{A-11}$$

$$Z_L^o = Z_{11}^A - Z_{12}^A = Z_0 \frac{1-\alpha e^{j\phi}}{1+\alpha e^{j\phi}} = \frac{Z_0^2}{Z_L^e} \tag{A-12}$$

with Z_{ij}^A, i, j = 1, 2, being the components of the impedance matrix $[Z^A]$ of the coupled antennas, which can be obtained from the scattering matrix $[S^A]$. And the corresponding reflection coefficients at the antenna input points are

$$\Gamma_L^e = \frac{Z_L^e - Z_0}{Z_L^e + Z_0} = \alpha e^{j\phi} \tag{A-13}$$

$$\Gamma_L^o = \frac{Z_L^o - Z_0}{Z_L^o + Z_0} = -\Gamma_L^e = -\alpha e^{j\phi} \quad . \tag{A-14}$$

After a simple derivation, the even-mode driving current I_A^e at point A_1 can be expressed as

$$I_A^e = \frac{I_{in}^{+}}{2} \cdot (1-\Gamma_{in}^e) \cdot \frac{1-\Gamma_L^e}{e^{j\theta} - \Gamma_L^e e^{-j\theta}} \, . \tag{A-15}$$

Similarly, the odd-mode driving current I_A^o is expressed as

$$I_A^o = \frac{I_{in}^{+}}{2} (1-\Gamma_{in}^o) \cdot \left(\frac{\frac{1}{j2B}}{Z_{in}^{o\prime} + \frac{1}{j2B}}\right) \cdot \left(\frac{1-\Gamma_L^o}{e^{j\theta} - \Gamma_L^o e^{-j\theta}}\right) \tag{A-16}$$

where

$$Z_{in}^{o\prime} = Z_0 \frac{e^{j\theta} + \Gamma_L^o e^{-j\theta}}{e^{j\theta} - \Gamma_L^o e^{-j\theta}} \tag{A-17}$$

and Γ_{in}^e and Γ_{in}^o are the reflection coefficients at point B_1 for the even mode and odd mode, respectively. When the two system ports are perfectly isolated, the input impedances at point B_1 of the even mode (Z_{in}^e) and odd mode (Z_{in}^o) should be the same, which can be easily derived by modeling the two-port network shown in Figure A.2(a) as a π network, and

$$\begin{aligned} Z_{in}^e &= Z_0 \frac{e^{j\theta} + \Gamma_L^e e^{-j\theta}}{e^{j\theta} - \Gamma_L^e e^{-j\theta}} \\ &= Z_{in}^o = Z_{in}^{o'} // (1/\, j2B) \end{aligned} \tag{A-18}$$

The corresponding reflection coefficients Γ_{in}^e and Γ_{in}^o in (A-15) and (A-16) are thus equal to each other. Finally, by casting (A-13) and (A-14) into (A-15) and (A-16), and using the relationships of (A-9), (A-10), and (A-18), the ratio of driving currents at the antenna input points can be derived as a function of the coupling coefficient:

$$\frac{I_{A1}}{I_{A2}} = \frac{I_A^e + I_A^o}{I_A^e - I_A^o} = \frac{1 + \dfrac{1 - j\alpha}{1 + j\alpha} \cdot \dfrac{1 + \alpha e^{j\phi}}{1 - \alpha e^{j\phi}}}{1 - \dfrac{1 - j\alpha}{1 + j\alpha} \cdot \dfrac{1 + \alpha e^{j\phi}}{1 - \alpha e^{j\phi}}} . \tag{A-19}$$

A3. Experimental Results of Single-band Solution

Two examples are tackled in this study. One is a dual-antenna system with two closely spaced parallel printed monopole antennas, and the other is with two miniaturized printed antennas. The antennas, operating at the frequency of 2.45 GHz, were all implemented on the FR4 substrates with the dielectric constant of 4.5, the loss tangent of 0.02, and the thickness of 0.8 mm. Both the EM simulator HFSS and the circuit simulator AWR Microwave Office were used for the simulation. The former handles the full-wave simulation for the antenna structure, with the results cast to the latter, if needed, for the following lumped-element related simulation.

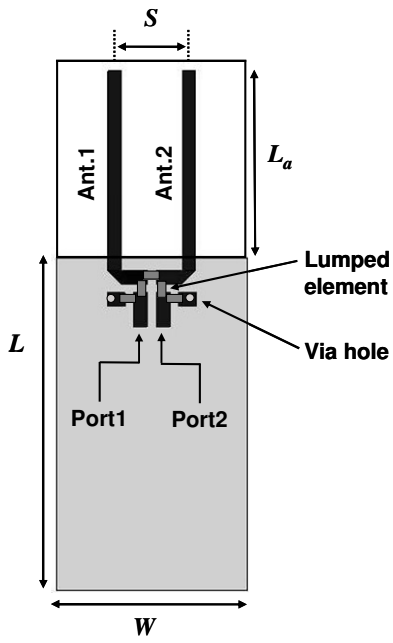

Figure A.3 The configuration of the two closely spaced printed monopole antennas.

The first example is two parallel printed monopole antennas with length L_a and spacing S = 8.5 mm (0.069λ_0 at 2.45GHz), as shown in Figure A.3. The antennas are fed by two 50Ω microstrip lines of width 1.5 mm on a substrate with ground size of $L \times W$ = 45 mm × 22 mm, which is suitable for a general USB dongle. By using the full-wave simulator HFSS, the antenna dimensions are first designed to be with length L_a = 22.5 mm and metal strip width of 1.5 mm for good input impedance matching. Figure A.4(a) plots the results of simulated S-parameters from 2 GHz to 3 GHz for the two coupled antennas in the complex plane. It is seen that at this stage, the reflection coefficient S_{11} (and S_{22}) is close to the origin of the coordinate around the center frequency, but the coupling coefficient S_{21} is not. This means that the two antennas exhibit input impedances close to 50Ω while have poor isolation between them. The coupling coefficient S_{21} at 2.45GHz is with an amplitude α = 0.77 and a phase ϕ = -25°. Figure A.4(b) and (c) depict, respectively, the return loss ($1/S_{11}$) and the isolation ($1/S_{21}$) as functions of the frequency. Both the simulation and measurement results are shown, which show good agreement with each other. The measured 10-dB return-loss bandwidth is 15.1% from 2.27 GHz to 2.64 GHz and the worst isolation in the in-band (from 2.4 GHz to about 2.5 GHz) is only 3 dB.

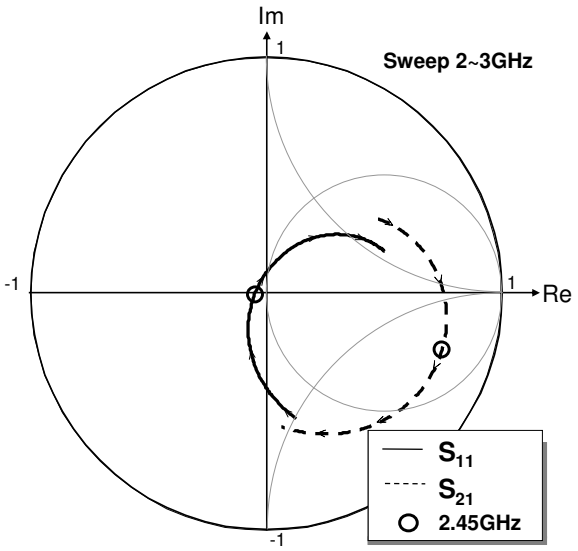

(a)

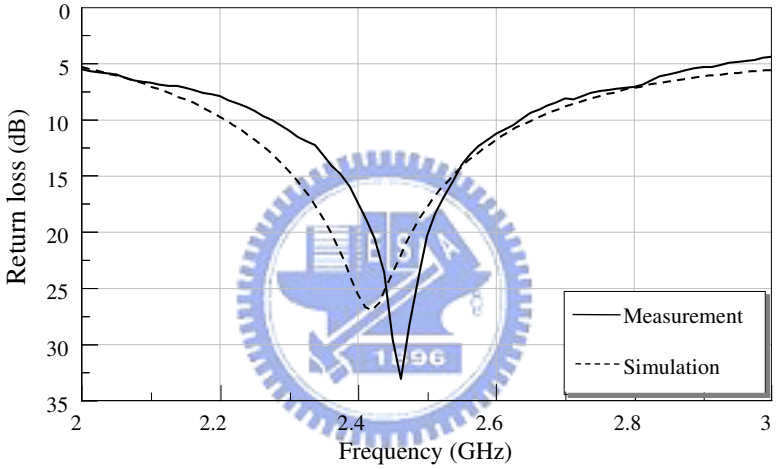

(b)

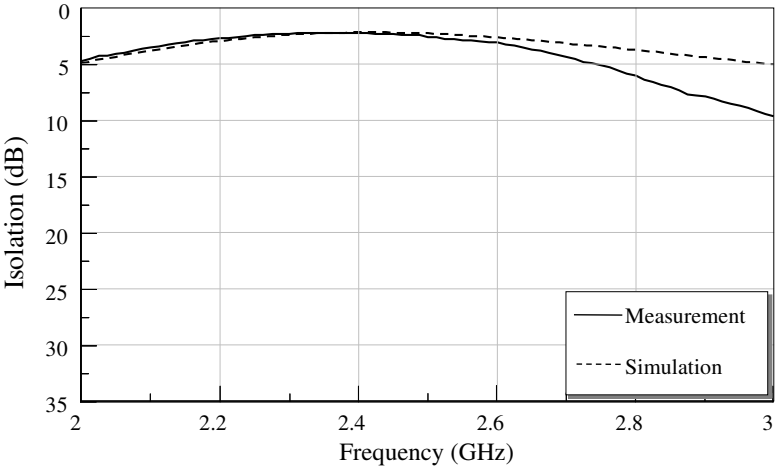

(c)

Figure A.4 (a)The simulated reflection coefficient S_{11} and coupling coefficient S_{21}, in the complex plane, of the strongly coupled monopole antennas. (b)Measured and simulated return losses. (c)Measured and simulated isolations.

According to the proposed structure in Figure A.1, the decoupling network was added after the two coupled antennas to increase the isolation between input ports. The required transmission-line length θ and the shunt susceptance B can be obtained by setting $\alpha = 0.77$ and $\phi = -25^{o}$ into (A-9) and (A-10), leading to $\theta = 32.5^{o}$ and $B = 0.97Y_0$ (or a capacitance of 1.26 pF). In practice, a 1pF Murata SMD capacitor with number of GRM1555C1H1R0CZ0 [55] was used. The high-frequency parasitics of the capacitor and the solders make the susceptance of this capacitor meet the requirement. The resultant S-parameters, return loss, and isolation are illustrated in Figure A.5. It is seen that the curve of the coupling coefficient (S_{21}) shown in Figure A.4(a) goes very close to the coordinate origin near the center frequency. The port isolation at 2.45GHz becomes 35 dB as shown in Figure A.4(c). There is at least 30dB improvement of isolation after the decoupling network is employed. However, this improvement of the isolation is obtained at the expense of deteriorating the input matching. As can be observed from Figure A.5(a) and (b), the impedance matched frequency shifts from 2.45 GHz to a lower one (2.36 GHz). The measured return loss at 2.45GHz is only 3dB. Further matching network is thus necessary in this situation. Since the isolation is very high (S_{21} almost zero), the additional impedance matching network will not change the isolation and the individual return loss, at least near the center frequency. A simple L-section matching network, with a series inductor (4.7/5.1 nH, Murata LQG15HN4N7S02/ LQG15HN5N1S02) and a shunt capacitor (1 pF, Murata GRM1555C1H1R0CZ0), is adopted at each input port to pull back the matched frequency to 2.45 GHz. Due to the experiment tolerance, the inductors used in the two ports are little different after fine tuning.

The final results for the antennas with the decoupling network and the matching network are depicted in Figure A.6. Both the curves for the reflection coefficient (S_{11}) and the coupling coefficient (S_{21}) shown in Figure A.6(a) go near the origin at the center frequency. The measured 10-dB return-loss bandwidth covers at least from 2 GHz up to 2.51 GHz, with a maximum return loss of 28 dB at 2.45 GHz. The best measurement isolation happens at 2.44 GHz and reaches a level of 30 dB. From 2.4 GHz to 2.5 GHz, the isolation has been improved to be better than 10 dB. It is seen that the matching network ameliorates the return loss while remains the high isolation. The measurement results match quite well with the simulation ones.

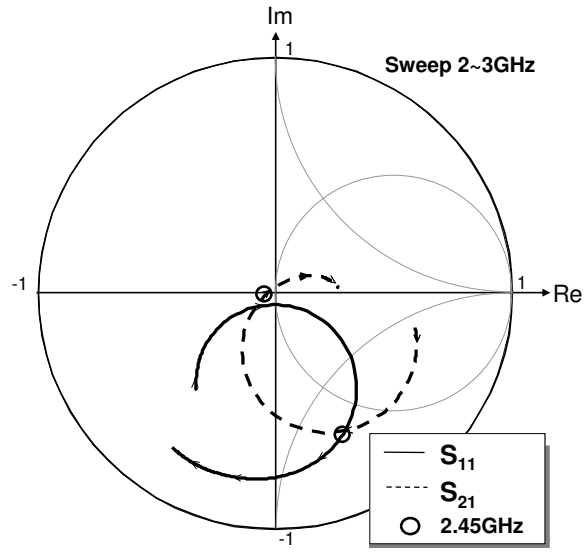

(a)

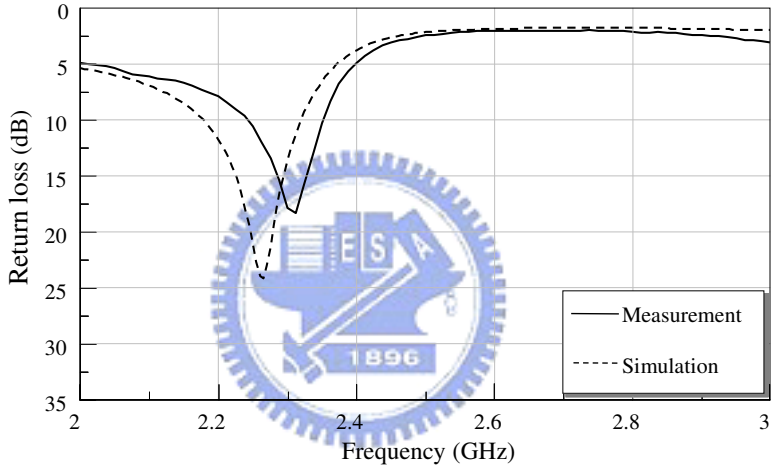

(b)

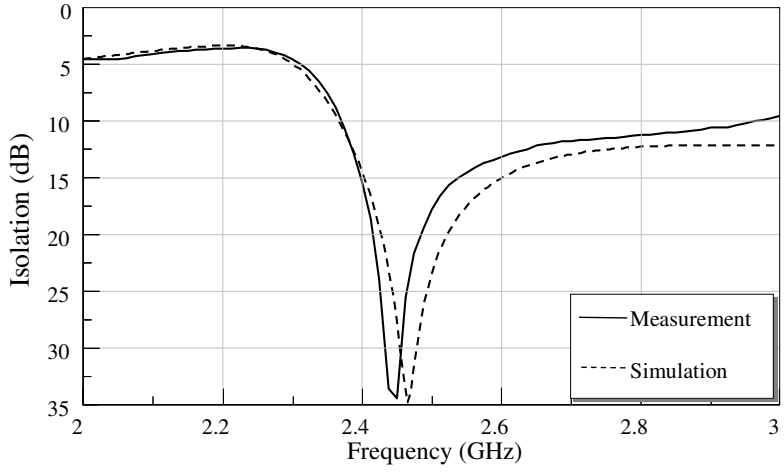

(c)

Figure A.5 (a)The simulated reflection coefficient S_{11} and coupling coefficient S_{21}, in the complex plane, of the coupling monopole antennas with decoupling network. (b)Measured and simulated return losses. (c)Measured and simulated isolations.

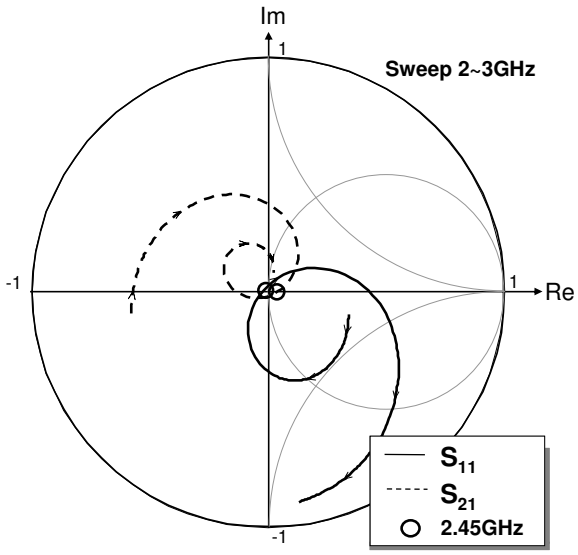

(a)

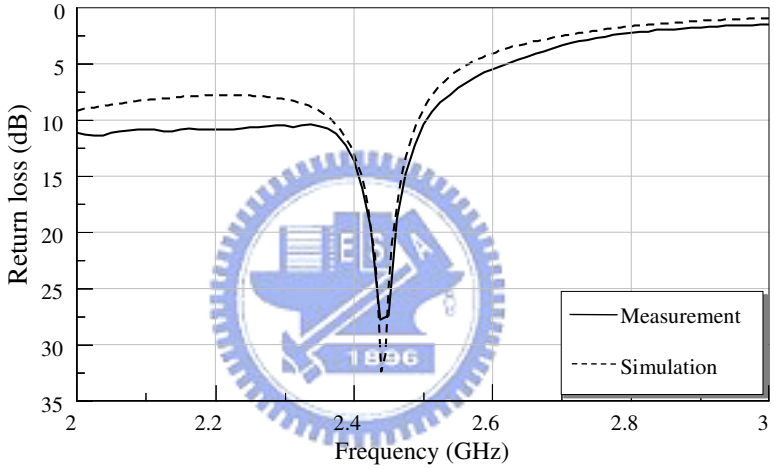

(b)

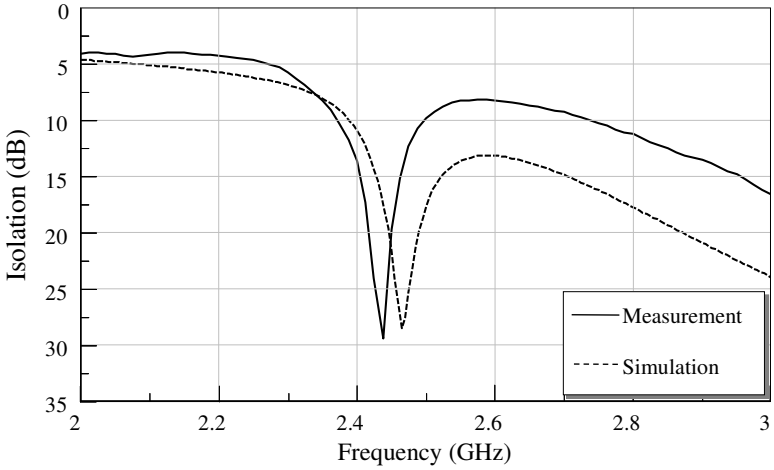

(c)

Figure A.6 (a)The simulated reflection coefficient S_{11} and coupling coefficient S_{21}, in the complex plane, of the coupling monopole antennas with decoupling network and impedance matching networks. (b)Measured and simulated return losses. (c)Measured and simulated isolations.

Figure A.7 shows the measured radiation patterns in the three principal planes of the finished high-isolation antennas, with port 1 excited and port 2 terminated to a 50-Ω load. Although only port 1 is driven, both antennas are distributed with currents due to the presence of the decoupling network and the strong near-field coupling between antennas. The ratio of currents induced on the two monopoles can be estimated through the result derived in the previous section. By inserting α = 0.77 and ϕ = -25° into (A-19), one obtains $I_{A1}/I_{A2} = 0.71\angle$-158°. The distance between the two antennas is 8.5 mm, which corresponds to a wave propagation delay of about 25° at 2.45GHz. Thus, the phase difference (-158°) of the excited antenna currents would cause an out-of-phase (-158° – 25° =-183°) far-field cancellation in the $+x$ direction, resulting in a radiation pattern directed toward the negative x direction as shown in Figure A.7. The measured peak gains are respectively 1.8 dBi in the x-y plane, -0.05 dBi in the x-z plane, and -3.9 dBi in the y-z plane. Although not shown here, the measured radiation patterns when fed from port 2 are similar to those in Figure A.7, but with the beam directed to the opposite direction (i.e., positive x direction). It should be mentioned that due to the induction of the ground plane current, the radiation patterns shown in the figure are different from those calculated using the two-element array theory. However, the measured pattern diversity effect does coincide with the theoretical prediction. The proposed antenna decoupling structure provides two complementary diversity patterns when the two antenna ports are fed separately, which is thus quite suitable for the application in a MIMO system with prosperous multiple signal paths.

It is interesting to evaluate the efficiency of the whole antenna system after the use of the decoupling network. To this end, the radiation patterns of two extra antennas are measured and compared to the present example. The first is a single printed monopole antenna and the second is two closely spaced printed monopole antennas without decoupling. Both the antennas have the same ground size and monopole strip size as the present example. Figure A.8 shows the measured radiation patterns in the x-y plane for the two antennas. In the measurement, the single monopole antenna is first matched by a series inductor (2.2 nH) for good return loss at the center frequency. And the coupled antennas without decoupling, whose return loss and isolation are shown in Figure A.4, is fed from port 1 with port 2

terminated. It is seen that the single printed antenna has a typical donut-like pattern with peak gain of -0.3 dBi. The strongly coupled antennas without decoupling also exhibit a near donut-like pattern but tilted due to the presence of the terminated monopole. Since half of the input power is absorbed in port 2, the radiation peak gain is only -3.23 dBi as shown in Figure A.8(b), about 3 dB lower than that of the single antenna. It is evident that the decoupled antennas in this example with measured peak gain of 1.8 dBi (Figure A.7(a)) possess an antenna gain 2.1dB higher than the single monopole antenna. Therefore, the array efficiency is approximately 80% based on the maximum array gain of 3dB for two-element array. Notably, this efficiency includes that of the matching circuit. According to the Murata's library, the matching efficiency is 93% when using L-type matching with a series 4.7 nH inductor and a shunt 1 pF capacitor.

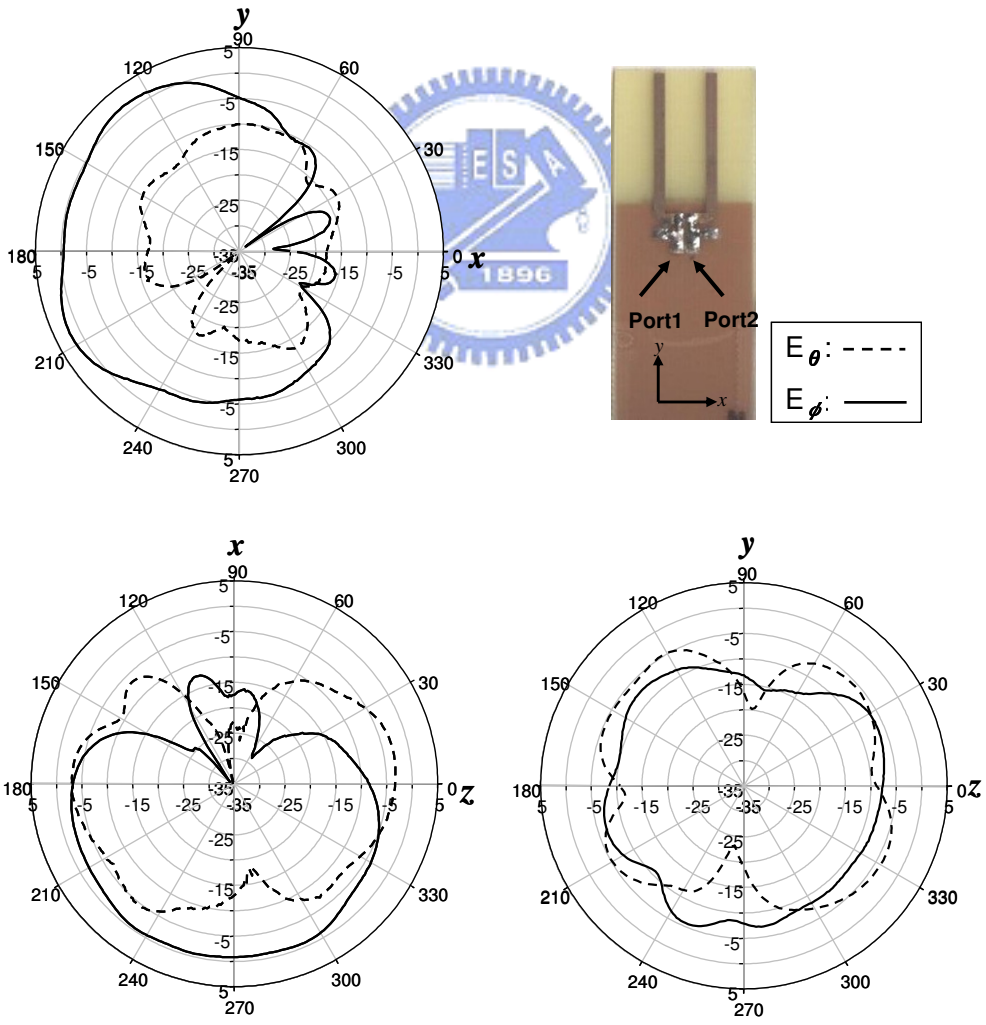

Figure A.7 Measured radiation patterns of the two closely spaced printed monopole antennas at 2.45GHz when fed from port 1: (a)*x*-*y* plane, (b)*x*-*z* plane, and (c)*y*-*z* plane.

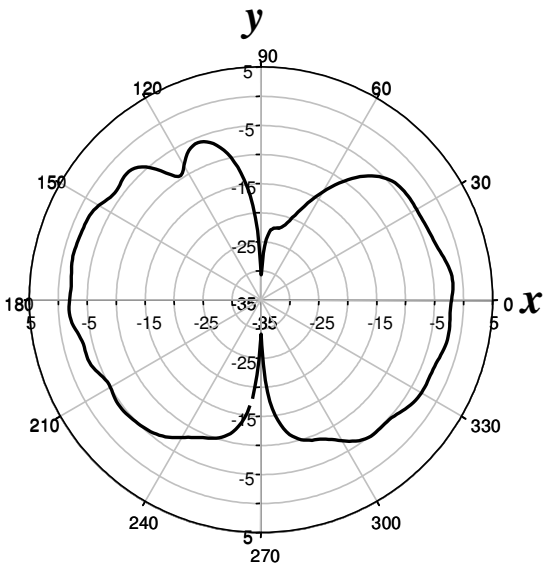

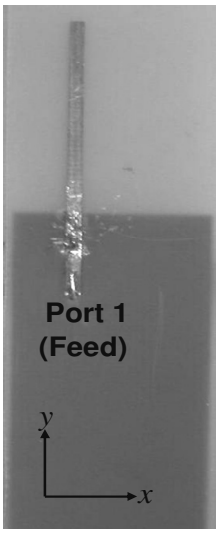

(a)

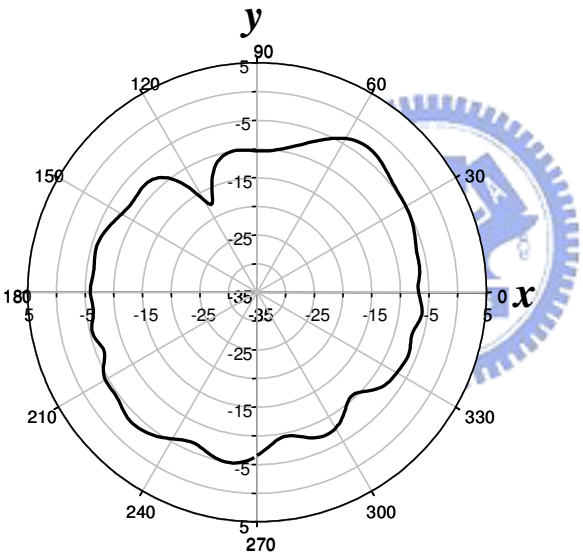

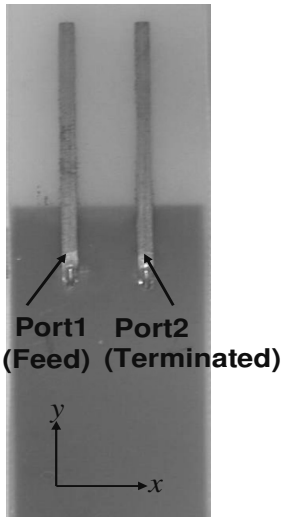

(b)

Figure A.8 Measured radiation patterns (E_φ) in the x-y plane of (a)the single printed monopole antenna and (b)the two closely spaced printed monopole antennas without decoupling. f = 2.45 GHz.

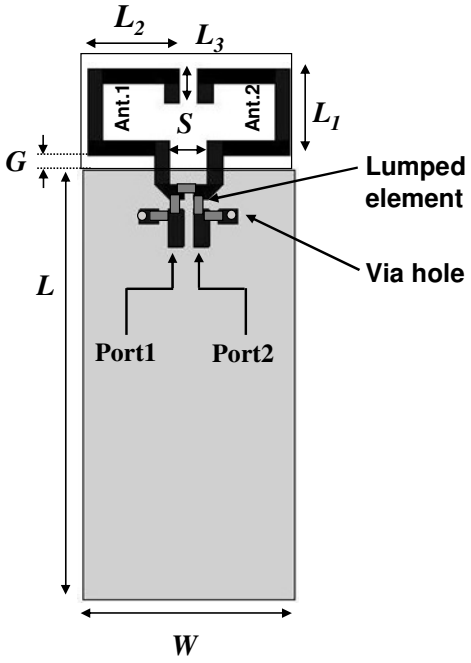

Figure A.9 The configuration of the two closely spaced miniaturized monopole antennas.

For practical application, the antennas in the previous example occupy too much antenna area and need to be miniaturized. Figure A.9 illustrates the miniaturized version of the printed monopole antennas, which are fabricated on the same FR4 substrate with the same ground size ($L \times W$ = 45 mm × 22 mm). The antenna dimensions are designed as L_1 = 7.5 mm, L_2 = 9.5 mm, L_3 = 3.5mm, S = 5 mm ($0.040\lambda_0$ at 2.45GHz), and G = 1.5 mm to have good input matching. The simulated coupling coefficient at the center frequency is with an amplitude of α=0.71 and phase of ϕ=-40°. Strong coupling still appears between these two miniaturized antennas. According to the decoupling solutions in (A-9) and (A-10), the required transmission line length of θ= 25° and shunt susceptance of B = $0.944Y_0$ (or a capacitance of 1 pF) were obtained. A shorter length of transmission lines and smaller capacitance are needed than those in the previous examples. For the impedance matching network, only a series inductor (4.3 nH) was adopted in each port. No shunt component was used in the practical implementation due to the lack of available capacitors with very small capacitances.

The resultant return losses and isolations are shown in Figure A.10(a) and (b), respectively. It is seen that the simulation return loss and isolation are better than 10 dB in the in-band with deeps at the design center frequency (2.45 GHz). And the

measurement results follow the simulation ones quite well. The deep of the measured return loss happens at a lower frequency (2.42 GHz) as shown in Figure A.10(a), owing to the omitting of the small shunt capacitance in the impedance matching network. However, the return loss still keeps higher than 10 dB in the frequency range from 2.4 GHz to 2.5 GHz, with a maximum value of 27 dB at 2.42 GHz. On the other hand, the measured isolation curve shifts a little bit toward the higher frequency as depicted in Figure A.10(b). The isolation is larger than 10 dB for frequencies higher than 2.4 GHz. A maximum isolation value of 20 dB was measured at the frequency of 2.46 GHz.

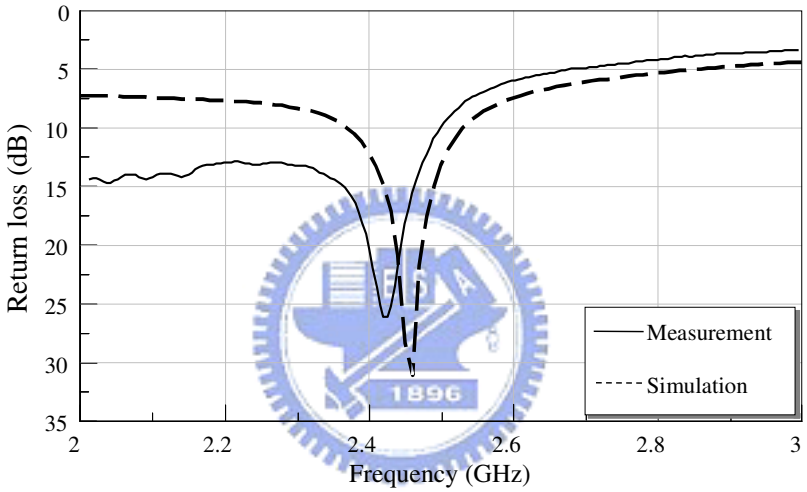

(a)

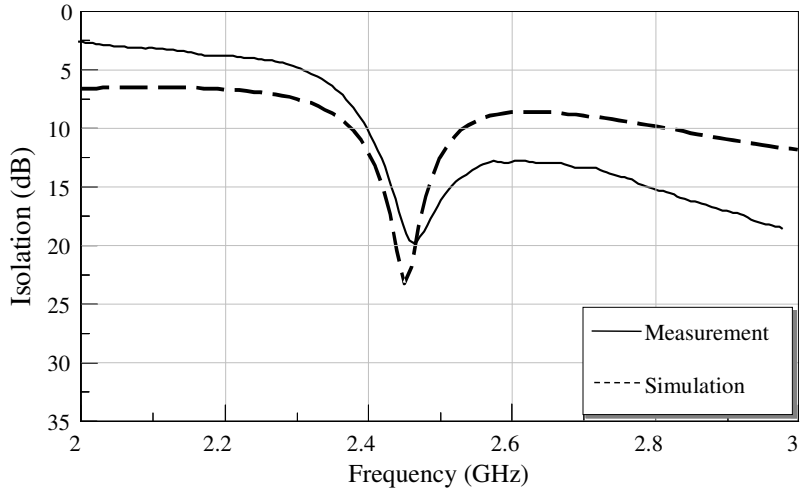

(b)

Figure A.10 (a)The return loss and (b)the isolation of the miniaturized monopole antennas with decoupling network and impedance matching networks.

Figure A.11 illustrates the measured radiation patterns with port 1 excited and port 2 terminated to a 50-Ω load. Like those of the parallel straight monopole antennas, the radiation pattern of the miniaturized antennas directed toward the negative *x* direction with measured peak gains of 1.57 dBi in the *x*-*y* plane, -2.3 dBi in the *x*-*z* plane, and -1 dBi in the *y*-*z* plane. The pattern changes to the positive *x* direction when the input power is fed from port 2. Following the discussion in the previous example, the array efficiency, as compared to a straight monopole antenna, is about 75%.

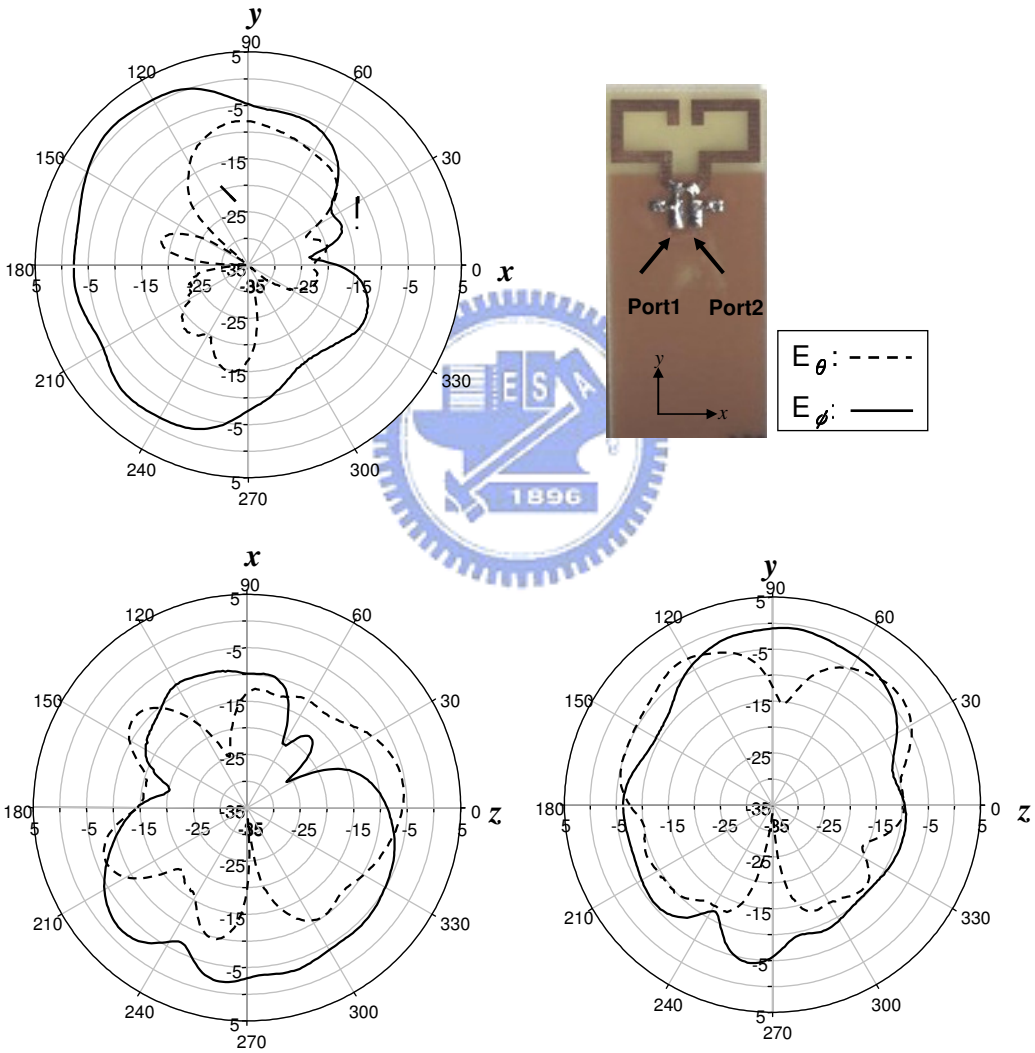

Figure A.11 Measured radiation patterns of the two closely spaced miniaturized monopole antennas at 2.45GHz when fed from port 1: (a) *x*-*y* plane, (b) *x*-*z* plane, and (c) *y*-*z* plane.

A4. Extended Design and Experimental Results of Dual-band Solution

The antennas were designed on an FR4 substrate with thickness of 0.8mm and the dielectric constant of 4.4, as shown in Figure A.12. The total dimensions of the substrate are L= 70mm and W=30mm with ground plane size of $W \times L_g$ = 30mm × 40mm. Each antenna was constructed by using the fork shape metal strips with the longer strip for low band operation and the shorter for high band. The strip width W_m = 1.56mm and strip lengths L_1 = 22mm, L_2 = 4mm, and L_3= 9 mm. The distance D between two antennas equals 10mm.

The simulated scattering parameters of the antennas are shown in Figure A.13. It is seen that, although the antennas possess good return losses in the two operating bands and high isolation in the 5 GHz band, there is strong coupling between antennas in the 2.4GHz band. Thus a decoupling network is designed to improve the isolation in the low band while without much degradation of the high isolation in the high band. Figure A.14 shows the schematic of the modified decoupling network which consists of a section of 50-Ω transmission line and a parallel lumped LC resonator. The resonator presents inductance in low band for decoupling and open circuit in high band. The layout of the proposed decoupling and matching circuit is illustrated in Figure A.12. The lengths of the 50-Ω microstrip lines are D_1=16.56 mm and D_2=4.75 mm, and the capacitor and inductor used are 0.5 pF and 1.5 nH, respectively. Since the property of lumped elements in high frequency is not ideal, the complete models provided by the manufacturer of these components should be used in the circuit simulation. The decoupling network would greatly reduce the antennas' coupling in the two frequency bands while changing the input impedances. Thus, two high-impedance microstrip stubs were connected at the input ports for impedance matching. The designed results of the stubs' length and width are L_{m1}=12.5mm, L_{m2}=6.5mm, and W_d=0.5mm, respectively. An additional capacitor parallel to the LC resonator was also used to improve the high-band impedance matching.

As shown in Figure A.13, the minimum isolation is about 4 dB at 2.4GHz band and the isolation is better than 20dB at 5GHz band. The input impedance matching is good in these bands. After employing the decoupling network and matching network, the measured S-parameter of the proposed antenna is shown in Figure A.15. It can be observed that the maximum isolation is near 20dB at 2.4GHz band but the isolation in 5GHz band has a little degradation. However, the isolation in high band is still kept above 15dB and the input return losses in both bands are better than 10dB. The decoupling and matching network improve the isolation in low band with a little degradation of high band.

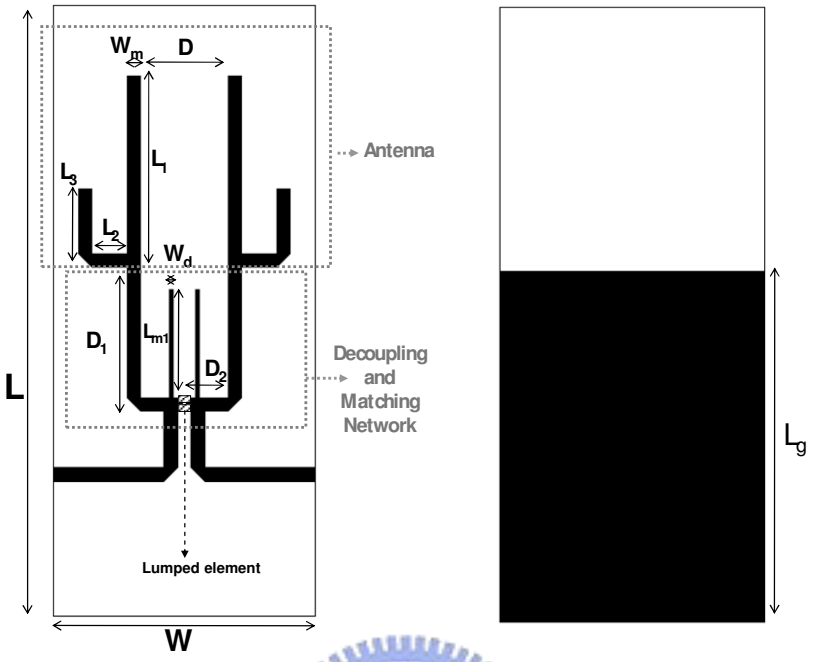

(a) (b)

Figure A.12 Antenna layout. (a)Top view (b)Bottom view.

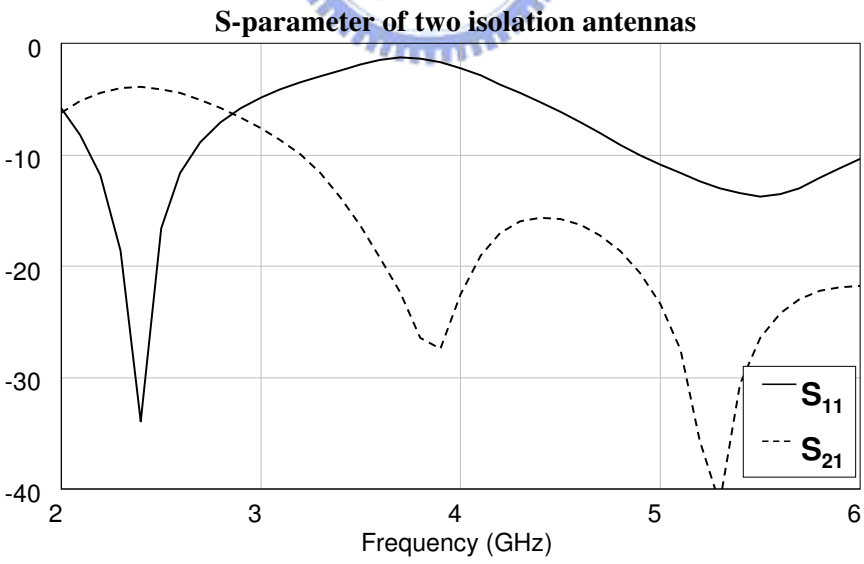

Figure A.13 Simulated S-parameters of the two closely spaced antennas.

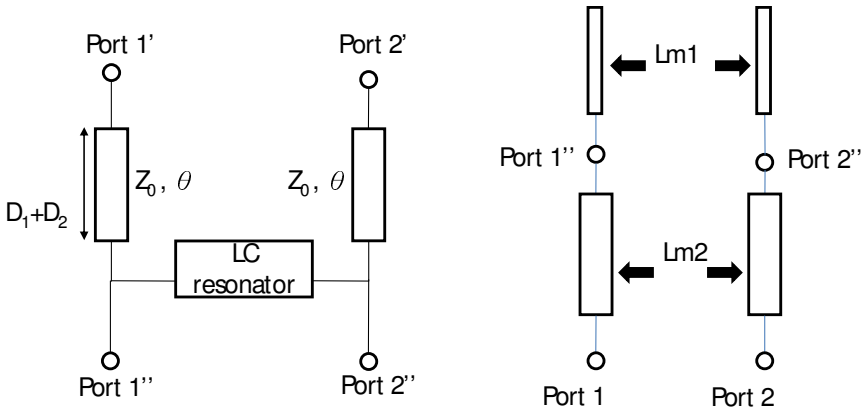

Figure A.14 (a)The decouple network and (b)the matching network.

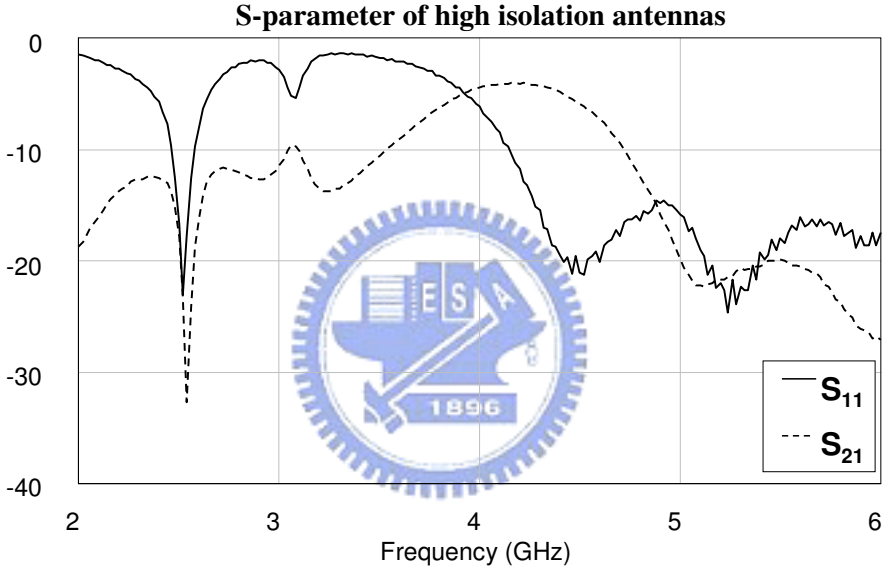

Figure A.15 Measured return loss and isolation of the finished antennas

Vita

Yu-Shin Wang was born in May 1981 in Taiwan, R.O.C. He received the B.S. degree in communication engineering from the National Chiao Tung University, Hsinchu, Taiwan, R.O.C., in 2003, where he is currently working toward the Ph.D. degree in communication engineering. He is currently involved with research on microwave circuits, antennas and antenna arrays.

Publication list

Journal papers

1. **Y.-S. Wang,** M.-F. Hsu, and S.-J. Chung, "A compact slot antenna utilizing a right/left-handed transmission line feed," *IEEE Trans. Antennas Propaga*., vol. 56, no. 3, pp. 675 – 683, Mar. 2008.
2. **Y.-S. Wang**, M.-C. Lee, S.-J. Chung, **"**Two PIFA-Related Miniaturized Dual-Band Antennas**,**" *IEEE Trans. Antennas Propaga.*, Vol. 55, Issue 3, Part 2, pp. 805 – 811, Mar. 2007.
3. S.-C. Chen, **Y.-S. Wang**, and S.-J. Chung, "A Decoupling Technique for Increasing the Port Isolation between Two Strongly Coupled Antennas," *IEEE Trans. Antennas Propaga.*, Dec. 2008.
4. I-Y. Tarn, **Y.-S. Wang**, and S.-J. Chung, "A Dual-Mode Millimeter-Wave Folded Microstrip ReflectArray Antenna," *IEEE Trans. Antennas Propaga*., Vol. 56, Issue 6, pp. 1510-1517, June 2008.
5. **Y.-S. Wang** and S.-J. Chung, "A Miniature Quadrifilar Helix Antenna for Global Position System Application," *IEEE Trans. Antennas Propaga.,* in revision.
6. **Y.-S. Wang**, J.-C. Lu, and S.-J. Chung, "A Miniaturized Ground Edge Current Choke –Design, Measurement, and Applications," *IEEE Trans. Antennas Propaga.,* accepted.
7. **Y.-S. Wang** and S.-J. Chung, "A Shorter Than One-Eighth Wavelength Open-End Slot Antenna with Equivalent Circuit Analysis," *IEEE Trans. Antennas Propaga.,* submitted

Conference papers

1. **Y.-S. Wang**, Y.-Y. Tsai, and S.-J. Chung, "A Crossed-Slot Coupled Patch Antenna Array with Wedge Design for DBS Reception," in *2008 IEEE AP-S*, San Diego, July 5-12, 2008.
2. C.-Y. Lui, **Y.-S. Wang**, and S.-J. Chung, "Two Nearby Dual-Band Antennas with High Port Isolation," in *2008 IEEE AP-S*, San Diego, July 5-12, 2008.
3. C.-H. Wu, M.-F. Hsu, **Y.-S. Wang**, S.-J, Chung, "A Novel Small Planar Antenna Utilizing Cascaded Right/Left-Handed Transmission Lines," in *2007 IEEE AP-S*, Hawaii, June 10-15, 2007.
4. S.-C. Chen, **Y.-S. Wang**, S.-J. Chung, "A New High Isolation Dual-Antennas with Miniature Decoupling Network Design," in *2007 IEEE AP-S*, Hawaii, June 10-15, 2007.
5. M.-L. Lee, **Y.-S. Wang**, and S.-J. Chung, "A Pattern Reconfigurable Strip Monopole with Eight Switched Printed Parasitic Elements," in *2007 IEEE AP-S*, Hawaii, pp. 3177-3180, June 10-15, 2007.
6. Y.-C. Shen, **Y.-S. Wang**, and S.-J. Chung, "A Printed Triple-Band Antenna for WiFi and WiMAX Applications," in *APMC*, Japan, Dec 2006.
7. **Y.-S. Wang** and S.-J. Chung, "Design of A Dielectric-loaded Quadrifilar Helix Antenna ," in *2006 IEEE International Workshop on Antenna Technology Small Antennas and Nove Metamaterials,* Mar 6-8, 2006.